CONNECTING ENTANGLEMENT ENTROPY GROWTH AND LOCAL INTEGRALS OF MOTION IN THE DISORDERED FERMI-HUBBARD MODEL

A Thesis Submitted to the Committee on Graduate Studies
in Partial Fulfillment of the Requirements for the Degree of Master of Science
in the Faculty of Arts and Science

TRENT UNIVERSITY
Peterborough, Ontario, Canada

Materials Science M.Sc. Graduate Program
May 2025

ABSTRACT

Connecting Entanglement Entropy Growth and Local Integrals of Motion in the Disordered Fermi-Hubbard Model

Ahad Nokhostin Helm

We study a one-dimensional Fermi-Hubbard model with disorder in charge and spin degrees of freedom. We calculate the time dependence of the entanglement entropy. While previous research on disordered interacting systems has typically focused on systems with either charge or spin, our model enables us to explore the interplay between charge and spin in shaping the behavior of entanglement. We use a method that identifies optimally local charge- and spin-specific integrals of motion. We ask how the locality level of these integrals of motion influences the capacity of low-order terms in the l-bit Hamiltonian to capture the entanglement entropy. Our results show that increasing the locality level improves the accuracy of low-order terms in capturing entanglement entropy dynamics. With equally strong charge and spin disorder, the behavior of the entanglement entropy closely resembles that observed in single-degree-of-freedom systems, and the l-bit Hamiltonian truncated at second order accurately captures this behavior.

Keywords: Many-Body Localization, Local Integrals of Motion, l-bit Hamiltonian, Entanglement Entropy, Fermi-Hubbard Model, Charge Disorder, Spin Disorder, Hungarian Algorithm

Acknowledgments

I am deeply grateful to my supervisor, Professor Rachel Wortis, for her invaluable guidance, support, and encouragement throughout my research. I also thank my wife, Shohreh, for her unwavering support and patience throughout this journey.

I acknowledge SHARCNET for providing the computational resources essential for this work. I am also grateful to Trent University for awarding me the International Graduate Student Scholarship and to the Slavin family for their generous support through the Slavin Bursary.

Contents

Abstract ii

Acknowledgments iii

List of Figures vi

List of Tables viii

List of Abbreviations ix

Chapter 1: Introduction 1
Many-body localization . . . 1
Equilibrium . . . 1
Failure to equilibriate . . . 3
Entanglement . . . 7
Definition of entanglement . . . 7
Time evolution of entanglement . . . 8
Why is entanglement useful? . . . 9
Local integrals of motion . . . 10
What are local integrals of motion? . . . 10
Why are LIOMs useful? . . . 11
How are LIOMs constructed? . . . 12
Research question . . . 15
Overview . . . 16

Chapter 2: Method 17
Hamiltonian . . . 17
Fock basis . . . 18
Energy basis . . . 19
Unitary transformations between bases . . . 20
Matrix representation . . . 20
Local integrals of motion and writing the Hamiltonian in terms of them 24
Creating integrals of motion . . . 24
Local integrals of motion . . . 26
Charge and spin . . . 28
Complete set of operators . . . 28
The Hamiltonian expressed in terms of LIOMs and their products 36
Quantifying entanglement as a function of time . . . 37
The definition of entanglement entropy . . . 37
Time dependence . . . 39

Chapter 3: Coding and Test Runs **43**
Eigenstates and time evolution . . . 44
Hamiltonian . . . 44
Eigenvalues and eigenstates . . . 53
Time evolution and density matrix . . . 54
Test runs for eigenstates and density matrix . . . 54
Entanglement Entropy . . . 56
Method . . . 56
Test runs for Entanglement entropy . . . 57
The Hungarian Algorithm . . . 58
The assignment problem . . . 59
Overview of the Hungarian algorithm . . . 59
Our implementation . . . 60
The primary question of our thesis . . . 63
Test of our implementation of the Hungarian Algorithm . . . 64
Integrals of motion and l-bit Hamiltonian . . . 64
Local integrals of motion . . . 65
Complete set of operators . . . 67
L-bit Hamiltonian . . . 70
Test runs . . . 73
Averaging . . . 74
Statistical measures . . . 74
Quantities being averaged over . . . 76
Coefficients in l-bit Hamiltonian . . . 77
Timescales . . . 80
Entanglement entropy . . . 80

Chapter 4: Results **82**
Assessing impact of Hungarian algorithm implementation . . . 82
Tests on random matrices . . . 83
Tests on entanglement entropy . . . 86
Contribution of the charge and spin local integrals of motion in the time dependence of entanglement entropy . . . 92
Exact Hamiltonian . . . 93
First-order truncated Hamiltonian . . . 95
Second-order truncated Hamiltonian . . . 98

Chapter 5: Conclusion **102**

Bibliography **107**

Appendix A: Hungarian algorithm, details **113**

Appendix B: Partial trace, details **119**

List of Figures

1.1 Probability distribution across sites in a clean and disordered one-dimensional lattice 4

3.1 Schematic representation of a 4-site-system state encoded as a byte 47
3.2 Schematic of first-nearest-neighbor hopping in a 4-site system . . 47
3.3 Masks used for calculating the hopping terms 49
3.4 Masks used for calculating the Hubbard term 51

4.1 The assignment deviation and runtime versus the Hungarian algorithm's accuracy level 84
4.2 The average and standard deviation of entanglement entropy for different numbers of disorder configurations 87
4.3 The standard error of the mean for the average entanglement entropy 88
4.4 The entanglement entropy from H_{liom1} with $U = 0$ and different accuracy levels of the Hungarian algorithm 90
4.5 The entanglement entropy from H_{liom1} with $U = 1$ and different accuracy levels of the Hungarian algorithm 90
4.6 The entanglement entropy from H_{liom2} with $U = 1$ and different accuracy levels of the Hungarian algorithm 91
4.7 The time-dependent behavior of the entanglement entropy from H_{exact} with $U = 0$ and $U = 1$ 93
4.8 The time-dependent behavior of the entanglement entropy from H_{liom1} with $U = 0$ and H_{exact} with $U = 0$ 95

4.9 The time-dependent behavior of the entanglement entropy from H_{liom1}, H_{liom1c} and H_{liom1s} with $U = 1$ 96
4.10 The timescales associated with the first and second-order terms in the l-bit Hamiltonian 98
4.11 The time-dependent behavior of the entanglement entropy from H_{liom2}, H_{liom2o}, $H_{liom2cc}$, $H_{liom2cs}$, and $H_{liom2ss}$ with $U = 1$ 99
4.12 The timescales associated with terms of all orders in the l-bit Hamiltonian 101

List of Tables

2.1 Energy basis to Fock basis transformation of an operator 26

3.1 Representations of states in a single-site system 45
3.2 Representations of states in a two-site system 46
3.3 Average coefficients in the l-bit Hamiltonian 79

4.1 The converging value of the Hungarian algorithm's accuracy level and the corresponding runtimes 85

A.1 Coefficient in the total Fock basis with single and double subscripts 122

List of Abbreviations

Acronym	**Definition**
EE	Entanglement Entropy
LIOM	Local Integral of Motion
MBL	Many-Body Localization
FIPR	Fock Inverse Participation Ratio

Introduction

In this chapter, we introduce three concepts essential for articulating the research question of this thesis. Specifically, we cover many-body localization (MBL), entanglement, and local integrals of motion (LIOMs), followed by the formulation of the research question. Finally, we provide an overview of the remaining chapters.

Many-body localization

MBL is an interesting phenomenon that arises in closed many-body quantum systems with disorder. This section introduces the concept of MBL, starting with the definition of equilibrium and then discussing the mechanisms through which equilibration can be prevented.

Equilibrium

Equilibrium in a physical system is a state in which the system's macroscopic properties, such as temperature, remain constant over time and uniform throughout the system. These stable macroscopic properties arise from the behavior of the system's microscopic components, or microstates.

Microstates refer to the specific detailed configurations of all the particles in the system. At equilibrium, the probabilities of the system being in each microstate

do not change over time. We can take the average of an observable over appropriately weighted microstates of an ensemble, or we can take the average of an observable over time. In equilibrium, these ensemble and time averages are the same. If the system starts far from equilibrium, it can evolve toward equilibrium. Below, we describe how classical and quantum closed systems reach equilibrium.

Closed classical system: Thermal equilibrium in a closed classical system arises from the chaotic nature of the dynamics governing the system. In chaotic dynamics, as the system explores its microstates, it eventually comes arbitrarily close to any possible microstate given sufficient time. Chaotic dynamics can only arise in systems described by differential equations second-order in time or higher.

For example, consider a dilute gas in a box. If a small amount of gas is injected into one corner of an initially empty box, the gas molecules will quickly spread out. Soon, it will be impossible to identify the initial injection point. The gas will eventually reach a state where its temperature and density are uniform throughout the container, signifying thermal equilibrium.

Closed quantum system: Quantum systems are governed by the Schrödinger equation, a differential equation that is first-order in time, and hence does not exhibit chaotic behavior. Understanding how quantum systems reach equilibrium remains an active area of research. Current understanding suggests that by examining the properties of subsystems we can infer whether the entire system has reached equilibrium.

For example, consider a one-dimensional chain of lattice sites, where particles can move between sites. We focus on a single site as a subsystem, using the occupation number at this site as the observable of interest. In equilibrium, the

expectation value of the occupation number at this site is consistent with its ensemble average, which is calculated using the Boltzmann distribution. The rest of the system acts as a thermal bath, with its temperature determined by the energy of the full system.

When the system is initially in an energy eigenstate, it remains static, showing no time dependence. However, when the system starts in a superposition of energy eigenstates, there will be time dependence. In this case, if the system begins out of equilibrium, it can evolve toward equilibrium.

Failure to equilibriate

There are various mechanisms through which a quantum system can fail to equilibrate. Here, we focus on how this can occur due to disorder. We'll begin by examining non-interacting particles moving on a lattice and then explore the interacting case, leading to a definition of MBL.

Non-interacting particles: Anderson localization

Disorder in non-interacting systems changes the dynamics of particles, leading to Anderson localization, a phenomenon that was originally demonstrated by Anderson.[1]

Consider the example of a one-dimensional lattice with an initial state where a single particle is inserted at the central site. Initially, the wavefunction is a delta function and can be represented as a weighted sum of energy eigenstates. As time passes, the probability amplitude of finding the particle at a given site shifts from being solely at the central site and spreads out into surrounding sites. However, this spreading is limited to the spatial extent of the eigenstates included in the weighted sum of the initial delta function. The system is in equilibrium if

each site has an occupation number consistent with the ensemble average, which means uniform occupation across all sites.

Consider two systems: one clean and one disordered. In the clean system, all lattice sites have equal potential. The energy eigenstates are Bloch states that extend uniformly over the entire lattice. The probability amplitude of finding the particle spreads to the whole lattice. Figure 1.1 (a,b,c) shows the time evolution of the occupation number at each site in the clean system. At long times, as shown in Figure 1.1(c), the occupancy of each site becomes steady and uniform. In this uniform distribution, the occupation number at each site converges to $1/L$, consistent with the ensemble average.

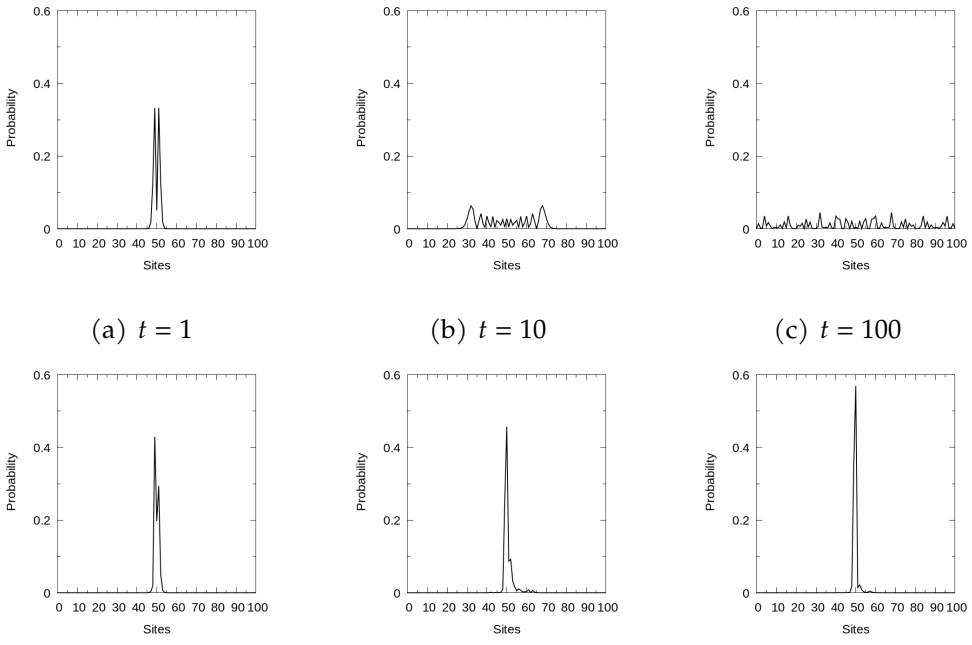

(a) $t = 1$ (b) $t = 10$ (c) $t = 100$

(d) $t = 1$ (e) $t = 10$ (f) $t = 100$

Figure 1.1: The probability distribution $|\psi(t)|^2$ as a function of position for a chain of 100 sites, with the initial state being a single particle located at the center of the chain, the clean system (a,b,c) and with site disorder (uniform distribution of width 4.0) (d,e,f).

In the disordered case, each site has a different potential. This alters the nature of the eigenstates; instead of Bloch states, the eigenstates become Anderson localized. These eigenstates are localized in specific regions of space and decay

exponentially away from those regions. Localized eigenstates with similar energies are spatially separated.[2] Since the initial delta function is a weighted sum of a few localized eigenstates, the probability amplitude does not spread across the whole lattice. Figure 1.1 (d,e,f) shows the time evolution of the occupation number at each site in the disordered system. Even at long times, a site far from where the particle was inserted shows no probability of occupation. The occupation number at this site is thus zero, in contrast to the ensemble average.

In general, a non-interacting system may have multiple particles. The many-body wavefunction is a product of single-particle states. Each single-particle wavefunction evolves independently and is governed by the system's energy eigenstates. In a disordered non-interacting system, this evolution fails to equilibrate due to the localized nature of the energy eigenstates.

Interacting particles: MBL

In the presence of interactions, the system's state can no longer be described simply by the occupancy of a set of single-particle states; instead, the state of all particles must be described together. Consequently, the Hilbert space expands significantly. MBL is a phenomenon occurring in interacting disordered quantum systems, where disorder prevents the system from thermalizing and reaching equilibrium. Similar to Anderson localization, MBL systems retain a memory of the initial state and exhibit a form of spatial localization, which will be discussed in detail later in this chapter.

MBL key developements

The interplay between interaction and Anderson localization was first addressed by Fleishman and Anderson.[3] Using perturbation theory, they suggested that localization can persist despite interaction. Following their work, numerous

studies were conducted on this topic. However, significant advancements were made by Gornyi et al.[4] and Basko et al.[5], who investigated the dynamical properties of interacting electrons in low-dimensional disordered systems at low temperatures. They found that below a critical temperature, the electron transport is suppressed due to localization. These studies suggest that localization persists even in interacting systems, setting the stage for the investigation of MBL.

Subsequent research has expanded our understanding of MBL, focusing on various aspects such as its persistence in the thermodynamic limit, the nature of the transition from an ergodic system to an MBL system, what exactly is local within the MBL system, the dynamics of information and entanglement propagation, and the suppression of particle and energy transport in MBL systems. [6], [7], and [8] are some major reviews on the topic.

MBL in experiment

Various experiments have found evidence of MBL. An example is an experiment by Schreiber et al. [9] They studied an isolated system of interacting ultracold atoms confined in a one-dimensional optical lattice. They prepared the system in an initial state, in which site occupancies alternate between two particles and empty. The sites with two particles were labeled as even sites, while the empty sites were labeled as odd sites. They then applied a quasi-periodic potential, created by superimposing two incommensurate periodic potentials. For the small size of the system, this quasi-periodic potential acted similarly to random disorder. They measured the imbalance between the particle density in even and odd sites over time. In cases where the disorder potential was weak, they noted a rapid reduction of this imbalance towards zero, indicating the system reached thermal equilibrium. Conversely, with a strong disorder potential, the imbalance initially declined but then reached a non-zero saturation value. The system

did not thermalize and localization persisted even in the presence of interactions, providing experimental support for MBL.

In the following sections, we will discuss two specific quantities used to characterize MBL systems: entanglement and LIOMs. This will be followed by presenting the main question of our research.

Entanglement

Entanglement is a fundamental concept in quantum mechanics that has no classical equivalent. In this section, we will define entanglement, explain how it evolves in many-body systems, and discuss its importance, especially in MBL systems.

Definition of entanglement

A composite system is a system composed of two or more subsystems. Entanglement is a quantum phenomenon where the global state of a composite system cannot be expressed as a product of the states of individual subsystems. As an example, consider a bipartite system of two sites between which spin-1/2 particles can move. Below, an example of a non-entangled state and an entangled state in this system are described.

A non-entangled state or product state is a state that can be expressed as the product of the states of individual subsystems. For example, one spin-up fermion on the left site and one spin-down fermion on the right site, denoted as $|\uparrow\rangle_{\text{Left}} \otimes |\downarrow\rangle_{\text{Right}}$. A product state has zero entanglement.

An entangled state is a state in which the state of one subsystem cannot be determined without considering the state of the other. For example, $\frac{1}{\sqrt{2}}(|\downarrow\rangle_{\text{Left}} \otimes$

$|\uparrow\rangle_{\text{Right}} + |\uparrow\rangle_{\text{Left}} \otimes |\downarrow\rangle_{\text{Right}})$.

A system that starts in a product state may evolve in time to an entangled state.

Having established the foundational understanding of entanglement, let's now turn our attention to its dynamic behavior over time.

Time evolution of entanglement

Entanglement can be quantified in various ways. The specific measure we use will be defined in the next chapter. Here, we describe qualitatively the evolution of the entanglement starting from a product state. In a generic system, in the absence of disorder, entanglement grows linearly in time, bounded solely by system size.[10, 11, 12] In an Anderson localized system, entanglement grows rapidly for a short period and then saturates to a constant value which is independent of the system size.[13, 14] In an interacting disordered system, entanglement has the same initial rapid growth, but, instead of going flat, continues to increase logarithmically in time and is ultimately limited by the system size. [10, 15, 16, 17, 18]

Entanglement growth in experiment

Understanding entanglement in MBL systems poses significant experimental challenges. Measuring entanglement is difficult because it is a property of the wavefunction, and wavefunctions of many-body systems are incredibly hard to measure. To fully characterize a wavefunction, one needs to measure the probability density everywhere, multiple times, and even then, the phase information remains elusive.

The entanglement observed in a closed quantum system arises from two sources. The motion of particles across the boundary between two subsystems produces

entanglement known as number entanglement. In addition, the correlations between particle configurations in the two subsystems can contribute to entanglement. This form of entanglement, which arises independently of particle transport between the subsystems, is called configuration entanglement.

A pioneering experiment by Lukin et al. [19] investigated an isolated 1D system of ultra-cold bosonic atoms confined in an optical lattice. They quantified number entanglement by raising the barrier between lattice sites to project the wavefunction onto each site and then measured the number of particles on each site. They also estimated configuration entanglement by measuring density-density correlations. This experiment marked the first time researchers successfully identified and characterized the logarithmic growth of entanglement in the MBL state in a closed quantum system, aligning with theoretical models.

Why is entanglement useful?

Understanding the evolution of entanglement in quantum systems is interesting for several reasons.

Firstly, entanglement is a key resource in quantum computing. Classical computers store information in bits, physical systems that are in either a 0 or a 1 state. Quantum computers store information in qubits, which are described by a wavefunction. For quantum computers to perform computations beyond classical capabilities, these qubits must be entangled. The unique properties of entangled qubits enable quantum algorithms to solve certain problems much more efficiently than classical algorithms.[20]

Secondly, entanglement can be used to characterize different phases of matter. For example, previously, we saw that entanglement growth is different in non-disordered, Anderson localized, and MBL systems. Additionally, entanglement has been used to study topological phases, which are challenging to characterize

using traditional local order parameters. [21]

Thirdly, entanglement characterizes information transport in quantum systems. Consider two parties, Alice and Bob, controlling different parts of a 1D system. Alice can encode a message by creating a perturbation on her part of the chain, while Bob measures some local operator on his part. Over time, Bob can receive the encoded message sent by Alice. [22] There is a theoretic limit on the speed of information propagation called the Lieb-Robinson bound.[23] Recent studies have shown a close relationship between the propagation of information and the growth of entanglement.[24, 25]

In summary, entanglement is a powerful tool for understanding quantum systems. It plays an important role in quantum computing, characterizes different phases of matter, and provides insights into information transport.

Local integrals of motion

This section starts by explaining what LIOMs are and why they are useful. Then, we look at how they can be constructed, discussing the challenges involved and the different methods used.

What are local integrals of motion?

Before getting to the definition of LIOMs, let's first explore what being conserved and local mean.

Conserved quantities

A conserved quantity is an observable that remains constant over time, implying that its corresponding operator commutes with the Hamiltonian. Systems can

possess multiple conserved quantities. A combination of two or more conserved quantities, either sum or product, is also a conserved quantity. Two conserved quantities are called independent if their corresponding operators are orthogonal: one cannot be expressed in terms of the other. An example of a conserved quantity is a projector operator onto one eigenstate of the Hamiltonian.

Locality

A strictly local operator only affects the state of one site while leaving all other sites unchanged. The concept of locality can be extended to include quasi-local operators, which can influence a finite region of neighboring sites, but with diminishing influence as we move away from the central site. This thesis will use the term local operator to mean either a strictly local or a quasi-local operator.

Definition of LIOMs

LIOMs are conserved quantities that are also local. The LIOMs of a system are not unique due to the possible combinations.[18] If two LIOMs in the same region are combined, the combination remains a local operator as well. In practice, researchers use the term LIOM with slightly varying meanings. Some methods for constructing LIOMs yield only approximately conserved local quantities, as discussed in Section 1.

Why are LIOMs useful?

LIOMs do not exist in all systems; their existence is characteristic of MBL systems. For the purpose of this thesis, LIOMs are valuable for two main reasons. Firstly, LIOMs and their products can be used to construct a complete set of operators in an MBL system. The LIOM operators and their products can chosen to

be independent (orthogonal). Consequently, any observable of interest, including the Hamiltonian, can be expressed as a linear combination of the operators in this set [26, 18], and this set provides a powerful framework for analyzing and understanding the properties of MBL systems. We will specify precisely how we construct the complete set in Chapter 2. Secondly, the existence of LIOMs in a system helps explain the unique time dependence of entanglement in MBL systems. A system that has one or multiple LIOMs is inhibited from exploring all possible microstates. As a result, different remote parts of the system become entangled more slowly compared to a system without any LIOMs. This restriction on entanglement growth due to LIOMs is a key feature that distinguishes MBL systems from generic systems, where entanglement grows linearly.[10, 11, 12]

How are LIOMs constructed?

LIOMs can be constructed exactly from the eigenstates of an interacting Hamiltonian. However, in many-body systems, the Hilbert space grows exponentially with system size, making it impractical to find the exact eigenstates for large systems. Another challenge is the non-uniqueness of LIOMs, as multiple operators can act as conserved quantities while exhibiting varying degrees of locality. As a result, it is essential to establish a mechanism for defining and optimizing the locality of these quantities in each construction approach.

Overview of methods for construction of LIOMs

There are various methods to define and construct LIOMs, each differing in how they balance conservation and locality. Below, we survey a selection of approximate methods and describe how the LIOMs constructed using these approaches achieve conservation and locality. Next, we review a few of the exact methods and, finally, introduce the method used in this thesis.

One of the first approaches taken is a perturbative approach, which starts with the exact eigenstates of the non-interacting Hamiltonian and treats the interaction as a perturbation. Researchers use perturbation theory to modify a strictly local, non-conserved operator into an approximately conserved and quasilocal one. This method has been effective in constructing approximately conserved operators for large systems.[27, 28, 29] However, it is limited by its reliance on weak interactions and is not accurate for strongly interacting systems.

Another method involves combining local operators in real space with adjustable coefficients to construct conserved operators within a specific region. By employing a minimization algorithm, researchers adjust these parameters to find a conserved operator. This approach, which does not require weak interactions, has been used to create approximately conserved operators that act within a specific region.[30] The conservation and locality achieved are approximate and depend on the effectiveness of the minimization algorithm.

A different strategy uses a unitary transformation operator called a displacement operator to shift the operators in phase space. Starting with strictly local operators, a series of displacement operators is applied to make a combination of them conserved. These transformations retain the quasi-local character of the operators. This method has successfully constructed approximately conserved LIOMs for systems up to 30 sites [31], though it is computationally intensive for larger systems.

To improve computational efficiency, a continuous version of displacement operators, known as the tensor flow equation, has been developed. This method offers higher efficiency and lower computational costs compared to using consecutive discrete displacement operators and has been applied to systems up to 36 sites.[32] Despite its scalability, it is still limited by system size.

Another innovative method involves long-time averaging of local operators. Over

time, local operators become nonlocal, but long-time averaging turns them into local operators as the nonlocal terms average out. This approach has shown that as the averaging period increases, the resulting LIOMs become more localized. Researchers have found exactly conserved and local LIOMs for systems up to 16 sites using this method.[33, 34] However, it is computationally intensive for long times and larger systems, and it is not clear that they are optimally local.

In another approximate approach, He et al. [35] started from the eigenstates of the non-interacting case and used a combinatorial optimization algorithm to identify maximally local LIOMs. This method was designed for weakly interacting systems, and while it achieved high locality, the LIOMs it produced were only approximately conserved.

While approximate methods provide valuable insights into the existence of LIOMs and characterize MBL in different systems, exact approaches aim to construct LIOMs that are maximally local and exactly conserved. These approaches use the energy eigenstates of the interacting Hamiltonian and various mechanisms to optimize locality. For example, Peng et al. [36], Adami et al. [37], and Gholami et al. [38] used the eigenstates of interacting Hamiltonian and mapping techniques to find exactly conserved LIOMs. However, these approaches did not incorporate a specific method to ensure the LIOMs achieved maximal locality.

We use an exact method with a mechanism to make the conserved quantities maximally local. In Chapter 2, we will describe this exact method and the mechanism in detail.

Research question

The list of methods provided above has been applied to systems with a single degree of freedom per site — either spin or charge. In contrast, we focus on a system that incorporates both spin and charge degrees of freedom at each site, as seen in experimentally realized MBL systems like cold atomic gases.

To model such a system, we study a one-dimensional lattice known as a Hubbard chain, in which spin-1/2 particles move freely between neighboring sites and interact only when occupying the same site. Broadly, this thesis addresses the question: Starting from a non-entangled state, how do the charge and spin degrees of freedom contribute to the growth of entanglement?

There has been previous research on MBL in the Hubbard chain. For instance, studies on a Hubbard chain suggest that disorder in the charge channel alone, without disorder in the spin channel, is insufficient to localize both charge and spin degrees of freedom.[39, 40, 41] Additionally, the introduction of both charge and spin-dependent disorder leads to the localization of both charge and spin degrees of freedom [39], and preliminary investigations into entanglement suggest a logarithmic growth within the limited timescale studied. [39, 42]

Early work on identifying LIOMs in the Hubbard chain by Wortis and Kennet [43] optimized the locality of LIOMs in a two-site Hubbard model with disorder only in the charge degree of freedom. Later, Leipner-Jones and Wortis [44] found maximally local and exactly conserved LIOMs in a larger Hubbard chain with disorder in both charge and spin degrees of freedom. Their identified LIOMs were specific to either charge or spin degrees of freedom, showing how localization in one degree of freedom relates to disorder in the other.

We will use the method of [44] to construct maximally local and exactly conserved LIOMs. By focusing on how these LIOMs and their products contribute

to the spreading of entanglement throughout the Hubbard chain, this thesis aims to explicitly connect entanglement growth with the LIOMs. Exploring the relationship between LIOMs and entanglement growth is also practically relevant to experimentally realized systems, such as cold atomic gases. Understanding this connection could offer valuable insights for developing strategies to control entanglement in these systems, a key component of quantum information processing.

Overview

The rest of the thesis is organized as follows. Chapter 2 introduces the Hamiltonian of the system and describes how operators and states are represented in different bases. It also details the method used to construct exactly conserved and maximally localized LIOMs for both charge and spin degrees of freedom. Furthermore, this chapter describes the measure used to quantify entanglement.

Chapter 3 focuses on the computational framework. It describes how the matrix representation of the Hamiltonian and LIOMs is constructed, explains the calculation of entanglement entropy, and outlines the averaging procedures. Notably, it provides a detailed description of the combinatorial optimization algorithm, which is used to make the LIOMs maximally local, and elaborates on the research question.

Chapter 4 presents our results. Lastly, Chapter 5 summarizes the findings and discusses potential directions for future research.

Method

This chapter describes the methods used to construct LIOMs and quantify entanglement. We begin by detailing the Hamiltonian and representations of our system in various bases. Next, we outline the process for identifying IOMs and a mechanism to make the IOMs maximally local. Next, we give the LIOMs charge and spin character. We then proceed to develop a complete set of operators, composed of these charge- and spin-specific LIOMs and their products, and express the Hamiltonian in terms of this operator set. Finally, we explain how to calculate EE, a measure of entanglement.

Hamiltonian

This section details the Hamiltonian of our system and defines the Fock basis and the energy basis. We also describe the concept of unitary transformations and how they generate a change of basis, in which the operators are represented.

Our system of interest consists of spin-1/2 fermions, which obey the Pauli exclusion principle. These fermions move within a one-dimensional lattice, where they can hop between neighboring sites. The fermions interact with each other through an on-site Coulomb repulsion when they occupy the same site. The disorder is introduced as random potentials and magnetic fields on each site. The Hamiltonian for this system is:

$$\hat{H} = -t_h \sum_{\sigma=\uparrow,\downarrow} \sum_{<i,j>} (\hat{c}^\dagger_{j\sigma}\hat{c}_{i\sigma} + \hat{c}^\dagger_{i\sigma}\hat{c}_{j\sigma}) + U \sum_i \hat{n}_{i\uparrow}\hat{n}_{i\downarrow} + \sum_i \epsilon_i(\hat{n}_{i\uparrow} + \hat{n}_{i\downarrow}) + \sum_i h_i(\hat{n}_{i\uparrow} - \hat{n}_{i\downarrow}) \quad (2.1)$$

In Eq.(2.1), the first term is the hopping term where t_h is the hopping amplitude, $\hat{c}^{(\dagger)}_{i\sigma}$ is fermion annihilation (creation) operator that removes (creates) a fermion with spin $\sigma = \pm 1/2$ on site i, and $< i, j >$ indicates that the summation runs over only nearest neighbor sites. The second term is the Hubbard interaction term in which U is a positive real number and $\hat{n}_{i\sigma} = \hat{c}^\dagger_{i\sigma}\hat{c}_{i\sigma}$ is called the number operator for spin σ on the i-th site. The third and fourth terms are disorder in charge and spin, respectively, in which ϵ_i and h_i are random variables drawn from uniform distributions over the intervals $[-W_{ch}, W_{ch}]$ and $[-W_{sp}, W_{sp}]$.

The Hamiltonian in Eq.(2.1) conserves total particle number and net spin in the z direction. These are globally conserved quantities, in contrast to LIOMs which are locally conserved quantities. The Hamiltonian operator itself is independent of any basis. For a given Hilbert space, one can choose a set of states that spans the space, known as a basis, express states (wavefunctions), and operators in this basis. Below, we describe two such bases: the Fock basis and the energy basis.

Fock basis

In the Fermi-Hubbard chain, particles in each site can be in one of four different states: $|0\rangle$ (empty), $|\uparrow\rangle$ (spin-up fermion), $|\downarrow\rangle$ (spin-down fermion) or $|2\rangle$ (doubly-occupied).

For a chain with L sites, a Fock state $|n\rangle$ is a product of the states of each site within the chain:

$$|n\rangle = |l\rangle_L \otimes |l\rangle_{L-1} \otimes \cdots \otimes |l\rangle_2 \otimes |l\rangle_1 , \tag{2.2}$$

where $|l\rangle_i$ is the state of site i .

The set of Fock states forms a complete and orthonormal basis that spans the Hilbert space. We represent the Fock basis as $\{|1\rangle , |2\rangle , ... , |N\rangle\}$ where $N = 4^L$.

A state $|\psi\rangle$, a many-body wavefunction of the particles in the Fermi-Hubbard chain, is expressed in the Fock basis as:

$$|\psi\rangle = \sum_n |n\rangle \langle n|\psi\rangle \tag{2.3}$$

An operator, such as Hamiltonian $\hat{H}$, can be expressed in Fock basis as:

$$\hat{H} = \sum_{nm} |n\rangle \langle n| \hat{H} |m\rangle \langle m| = \sum_{nm} \langle n| \hat{H} |m\rangle |n\rangle \langle m| \tag{2.4}$$

Energy basis

The eigenstates of the Hamiltonian $\{|E_n\rangle\}$, defined by $\hat{H} |E_n\rangle = E_n |E_n\rangle$, form another complete set of states that spans the Hilbert space, called the energy basis.

A state $|\psi\rangle$ is expressed in the enegy basis as:

$$|\psi\rangle = \sum_n |E_n\rangle \langle E_n|\psi\rangle \tag{2.5}$$

An operator, such as the Hamiltonian, can be expressed in the energy basis as:

$$\hat{H} = \sum_{nm} |E_n\rangle \langle E_n| \hat{H} |E_m\rangle \langle E_m| = \sum_n E_n |E_n\rangle \langle E_n| . \tag{2.6}$$

Eq.(2.6) makes transparent that Hamiltonian is diagonal in energy basis.

Unitary transformations between bases

A unitary transformation is a map between two inner product spaces that preserves the inner product. When the map is from a space back onto itself, it is called a unitary operator [45]. A unitary operator satisfies $\hat{U}\hat{U}^\dagger = \hat{U}^\dagger\hat{U} = \hat{I}$.

In quantum mechanics, a unitary transformation generated by the unitary operator $\hat{U}$ transforms all states as $\hat{U}\left|\psi\right\rangle = \left|\psi'\right\rangle$ and all operators as $\hat{U}\hat{A}\hat{U}^\dagger = \hat{A}'$. This unitary transformation preserves the Hermiticity of operators, operator equations, eigenvalues of operators, and matrix elements $\langle\xi|\,\hat{A}\left|\psi\right\rangle$.

In this thesis, we use a unitary operator of the following form to generate the transformation from the Fock basis to the energy basis:

$$\hat{U} = \sum_n |n\rangle\langle E_n| \tag{2.7}$$

We use a particular matching of the Fock states to the energy eigenstates, as discussed below in Section 2.

Matrix representation

From 2.2 to 2.7, all equations are in the Dirac notation, in which the states $\{|n\rangle\}$ and $\{|E_n\rangle\}$ can be represented in any chosen basis.

For computational purposes, these symbolic expressions of states and operators need to be converted into vectors and matrices, as computers operate with numbers rather than symbols.

To distinguish between an operator (or state) and its matrix (or vector) representation, we use the following notation:

- Representations in the Fock basis are denoted with the subscript F, while those in the energy basis use the subscript E.
- The vector representation of a state is denoted by a vector symbol.
- The matrix representation of an operator is denoted by double underlines.

Vector representation of a state in the Fock basis is

$$(\vec{\psi}_F)_i = \sum_n \langle n|\psi\rangle \langle i|n\rangle = \sum_n \langle n|\psi\rangle \delta_{i\,n} = \langle i|\psi\rangle$$

$$\vec{\psi}_F = \begin{pmatrix} \langle 1|\psi\rangle \\ \langle 2|\psi\rangle \\ \vdots \\ \langle N|\psi\rangle \end{pmatrix} \tag{2.8}$$

Similarly, the vector representation of a state in the energy basis is:

$$\vec{\psi}_E = \begin{pmatrix} \langle E_1|\psi\rangle \\ \langle E_2|\psi\rangle \\ \vdots \\ \langle E_N|\psi\rangle \end{pmatrix} \tag{2.9}$$

Matrix representation of the Hamiltonian in the Fock basis is

$$(\underline{\underline{H}}_F)_{ij} = \langle i|\hat{H}|j\rangle$$

$$\underline{\underline{H}}_F = \begin{bmatrix} \langle 1|\hat{H}|1\rangle & \langle 1|\hat{H}|2\rangle & \dots & \langle 1|\hat{H}|N\rangle \\ \langle 2|\hat{H}|1\rangle & \langle 2|\hat{H}|2\rangle & \dots & \langle 2|\hat{H}|N\rangle \\ \vdots & \ddots & \ddots & \vdots \\ \langle N|\hat{H}|1\rangle & \langle N|\hat{H}|2\rangle & \dots & \langle N|\hat{H}|N\rangle \end{bmatrix} \tag{2.10}$$

Matrix representation of the Hamiltonian in energy basis is:

$$(\underline{\underline{H}}_E)_{ij} = \langle E_i|\hat{H}|E_j\rangle$$

$$\underline{\underline{H}}_E = \begin{bmatrix} \langle E_1|\hat{H}|E_1\rangle & \langle E_1|\hat{H}|E_2\rangle & \dots & \langle E_1|\hat{H}|E_N\rangle \\ \langle E_2|\hat{H}|E_1\rangle & \langle E_2|\hat{H}|E_2\rangle & \dots & \langle E_2|\hat{H}|E_N\rangle \\ \vdots & \ddots & \ddots & \vdots \\ \langle E_N|\hat{H}|E_1\rangle & \langle E_N|\hat{H}|E_2\rangle & \dots & \langle E_N|\hat{H}|E_N\rangle \end{bmatrix} = \begin{bmatrix} E_1 & 0 & \dots & 0 \\ 0 & E_2 & \dots & 0 \\ \vdots & \ddots & \ddots & \vdots \\ 0 & 0 & \dots & E_N \end{bmatrix} \tag{2.11}$$

The elements of the operator $\hat{U}$ are the same whether it is expressed in the Fock basis or the energy basis.

$$(\underline{\underline{U}}_F)_{ij} = \sum_n \langle i|n\rangle \langle E_n|j\rangle = \sum_n \delta_{i\,n} = \langle E_i|j\rangle$$
$$(\underline{\underline{U}}_E)_{ij} = \sum_n \langle E_i|n\rangle \left\langle E_n|E_j\right\rangle = \sum_n \delta_{j\,n} = \langle E_i|j\rangle \tag{2.12}$$

Note that the rows of the matrix representation of the unitary operator $\underline{\underline{U}}$ are the transpose of the vector representation of the energy eigenstates in the Fock basis.

Using the matrix $\underline{\underline{U}}$, a state is transformed from the Fock basis to the energy basis as:

$$
\begin{aligned}
(\underline{\underline{U}}\vec{\psi}_F)_n &= \sum_m (\underline{\underline{U}})_{nm}(\vec{\psi}_F)_m \\
&= \sum_m \langle E_n|m\rangle \langle m|\psi\rangle \\
&= \langle E_n| (\sum_m |m\rangle \langle m|) |\psi\rangle = \langle E_n| \hat{I} |\psi\rangle \\
&= (\vec{\psi}_E)_n \\
\Rightarrow \underline{\underline{U}}\vec{\psi}_F &= \vec{\psi}_E
\end{aligned} \tag{2.13}
$$

The $\vec{\psi}_F$ and $\vec{\psi}_E$ are the vector representations of the same state in the Fock and energy bases, respectively.

The Hamiltonian is transformed from the Fock basis to the energy basis as:

$$
\begin{aligned}
(\underline{\underline{U}}\,\underline{\underline{H}}_F\,\underline{\underline{U}}^\dagger)_{nm} &= \sum_{pq} (\underline{\underline{U}})_{np}(\underline{\underline{H}}_F)_{pq}(\underline{\underline{U}}^\dagger)_{qm} \\
&= \sum_{pq} \langle E_n|p\rangle \langle p| \hat{H} |q\rangle \langle q|E_m\rangle \\
&= \langle E_n| (\sum_p |p\rangle \langle p|) \hat{H} (\sum_q |q\rangle \langle q|) |E_m\rangle \\
&= \langle E_n| \hat{I}\hat{H}\hat{I} |E_m\rangle \\
&= \langle E_n| \hat{H} |E_m\rangle = (\underline{\underline{H}}_E)_{nm} \\
\Rightarrow \underline{\underline{U}}\,\underline{\underline{H}}_F\,\underline{\underline{U}}^\dagger &= \underline{\underline{H}}_E
\end{aligned} \tag{2.14}
$$

$\underline{\underline{H}}_F$ and $\underline{\underline{H}}_E$ are matrix representations of the same operator $\hat{H}$ in the Fock and energy bases, respectively.

Local integrals of motion and writing the Hamiltonian in terms of them

In this section, we outline our method for generating IOMs and describe an optimization technique to make them as localized as possible. Using this approach, we make LIOMs specifically with charge or spin character. We then use these LIOMs to construct a complete set of operators, which allows us to fully expand the Hamiltonian in terms of this set.

Creating integrals of motion

An integral of motion (IOM) is an operator representing a conserved quantity, which consequently commutes with the Hamiltonian, as discussed in Section 1. Below, we outline our method for identifying these integrals of motion within our model.

The transformation from the energy basis to the Fock basis is generated by the unitary operator $\hat{Q} = \hat{U}^{\dagger}$, where:

$$\hat{Q} = \sum_{p} \left|E_p\right\rangle \langle p| \tag{2.15}$$

The matrix elements of the operator $\hat{Q}$ are the same in both the energy and Fock bases:

$$(\underset{\underset{E}{=}}{Q})_{ij} = \sum_{p} \langle E_i|E_p\rangle\langle p|E_j\rangle = \sum_{p} \delta_{i\,p}\langle p|E_j\rangle = \langle i|E_j\rangle. \tag{2.16}$$

The columns of $\underset{=}{Q}$ are the energy eigenvectors expressed in the Fock basis.

Here, we will show that applying $\hat{Q}$ to an operator that is diagonal in the Fock

space, generates a new operator which is diagonal in the energy basis and hence is an integral of motion.

Consider an operator $\hat{A}$ that is diagonal in the Fock basis:

$$\begin{aligned}
\hat{A} =&(\sum_n |n\rangle \langle n|)\hat{A}(\sum_m |m\rangle \langle m|) \\
=& \sum_{nm} |n\rangle (\langle n| \hat{A} |m\rangle) \langle m| \\
=& \sum_{nm} |n\rangle (A_m \langle n|m\rangle) \langle m| \\
=& \sum_{nm} A_m \delta_{nm} |n\rangle \langle m| \\
=& \sum_n A_n |n\rangle \langle n|
\end{aligned} \tag{2.17}$$

Applying the unitary transformation $\hat{Q}$ to $\hat{A}$ produces a new operator $\hat{A}'$:

$$\begin{aligned}
\hat{A}' =&\hat{Q}\hat{A}\hat{Q}^\dagger \\
=&(\sum_n |E_n\rangle \langle n|)\hat{A}(\sum_m |m\rangle \langle E_m|) \\
=& \sum_{nm} |E_n\rangle \langle n| \hat{A} |m\rangle \langle E_m| \\
=& \sum_{nm} |E_n\rangle A_m \langle n|m\rangle \langle E_m| \\
=& \sum_{nm} |E_n\rangle A_m \delta_{nm} \langle E_m| \\
=& \sum_n A_n |E_n\rangle \langle E_n|
\end{aligned} \tag{2.18}$$

Table 2.1 summarizes the effect of the unitary transformation on an operator $\hat{A}$.

Since the operator $\hat{A}'$ is diagonal in the energy basis, it commutes with the Hamiltonian $\hat{H}$, making it an integral of motion.

	$\hat{A}$	$\hat{A}'$
Energy basis	$\underline{\underline{A}}_E$ where $(\underline{\underline{A}}_E)_{ij} = \langle E_i \vert \hat{A} \vert E_j \rangle$	$\underline{\underline{A'}}_E$ where $(\underline{\underline{A'}}_E)_{ij} = A'_j \delta_{ij}$
Fock basis	$\underline{\underline{A}}_F$ where $(\underline{\underline{A}}_F)_{ij} = \langle i \vert \hat{A} \vert j \rangle = A_j \delta_{ij}$	

Table 2.1: Most commonly, a unitary transformation is carried out in matrix representation and is used to take an operator $\hat{A}$ expressed in the energy basis and re-express it in the Fock basis (moving vertically in the table). However, as shown in Eq.(2.18), the unitary transformation executed in Dirac notation can be seen as creating a new operator $\hat{A}'$ which has the same elements in the energy basis as the operator $\hat{A}$ has in the Fock basis (moving horizontally in the table).

Thus, the unitary transformation generated by $\hat{Q}$ on an operator that is diagonal in the Fock basis produces a new operator that is an integral of motion.

Local integrals of motion

In Section 2, we described how we construct integrals of motion by the unitary transformation of an operator that is diagonal in the Fock basis. Our objective is to generate local integrals of motion. To achieve this, we start with a local operator and then change the operator as little as possible with the unitary transformation.

We begin with an operator, $\hat{A}$, that is both local and diagonal in the Fock basis. A unitary transformation, $\hat{Q}$, is then applied to $\hat{A}$ to generate an integral of motion,$\hat{A}'$. If $\hat{Q}$ were the identity operator, the resulting integral of motion would remain local. Therefore, $\hat{Q}$ is constructed to be as close as possible to the identity operator. This ensures that the resulting integral of motion, $\hat{A}'$, is being changed as little as possible compared to the original operator, $\hat{A}$, and maximally preserves the locality of $\hat{A}$.

We denote such an optimized unitary operator as $\hat{Q}_{opt}$. The transformation of operator $\hat{A}$ generated by $\hat{Q}_{opt}$, results in a local integral of motion: $\hat{A}' = \hat{Q}_{opt} \hat{A} \hat{Q}^{\dagger}_{opt}$. In the following, we describe how we find $\hat{Q}_{opt}$.

A unitary operator $\hat{Q}$ maps the energy eigenstates $|E_n\rangle$ to the Fock states $|n\rangle$, as defined in Eq.(2.15). In the matrix representation, the columns of $\underline{\underline{Q}}$ are the energy eigenvectors in the Fock representation. The order of the columns in $\underline{\underline{Q}}$ determines the correspondence between the energy eigenstates and the Fock states. The numerical approach that we are using produces $\underline{\underline{Q}}$ such that the order of columns is in increasing energy eigenvalues, $\{\vec{E}_0, \vec{E}_1, \dots, \vec{E}_{N-1}\}$. Therefore initially, the ground state $\left|E_0\right\rangle$ is mapped to $|0\rangle$, the first excited state $|E_1\rangle$ to $|1\rangle$, and so on.

However, a $\underline{\underline{Q}}$ with a different order of columns assigns energy eigenstates to the Fock states differently.

$$\hat{Q}\,|n\rangle = \sum_p \langle E_{a(p)}|p\rangle\,\langle n| = \sum_p \langle E_{a(p)}|\delta_{pn} = |E_{a(n)}\rangle \tag{2.19}$$

In Eq.(2.19), $a(n)$ is an integer from 0 to $N-1$ and specifies the energy eigenstate $\left|E_{a(n)}\right\rangle$ that is assigned to the Fock state $|n\rangle$.

The combination of all $a(n)$s forms the assignment array $\{a(n) : n = 0, \dots, N-1\}$ that is equivalent to a specific order of the energy eigenvectors $\{\vec{E}_{a(0)}, \vec{E}_{a(1)}, \dots, \vec{E}_{a(N-1)}\}$ in $\underline{\underline{Q}}$.

The assignment array $\{a(n)\}$ can be any permutation of the integers from 0 to $N-1$. There are $N!$ possible assignment arrays, each representing a different correspondence between the energy eigenstates and the Fock states.

Our approach is to find a specific order of columns in the matrix representation of the unitary operator $\hat{Q}$, such that the sum of the magnitudes of the diagonal elements is maximum. Such an order of columns determines the matrix representation of the operator $\hat{Q}_{opt}$ which is as close as possible to the identity operator.

In Section 3, we describe the combinatorial optimization method used to find the permutation of integers in the assignment array $\{a_n\}$ that maximizes the sum of the diagonal elements' magnitudes in the matrix representation of $\hat{Q}$.

Charge and spin

We are interested in distinguishing the influence of charge and spin. Therefore, we now focus on local operators in the Fock basis that are specific to the charge and spin degrees of freedom for each site.

The on-site charge density, $\hat{d}_i$, and magnetization, $\hat{m}_i$, are local operators that are diagonal in the Fock basis.

$$\begin{aligned} \hat{d}_i &= \hat{c}^\dagger_{i\uparrow}\hat{c}_{i\uparrow} + \hat{c}^\dagger_{i\downarrow}\hat{c}_{i\downarrow} = \sum_n d_{i,n} \left|n\right\rangle \left\langle n\right| \\ \hat{m}_i &= \hat{c}^\dagger_{i\uparrow}\hat{c}_{i\uparrow} - \hat{c}^\dagger_{i\downarrow}\hat{c}_{i\downarrow} = \sum_n m_{i,n} \left|n\right\rangle \left\langle n\right| . \end{aligned} \tag{2.20}$$

The unitary transformation generated by $\hat{Q}_{opt}$ yields LIOMs that are specific to the system's charge $\hat{Q}_{opt}\hat{d}_i\hat{Q}^\dagger_{opt}$ and spin $\hat{Q}_{opt}\hat{m}_i\hat{Q}^\dagger_{opt}$ degree of freedom.

However, these are not quite the LIOMs that we will use. In the next section, we will describe the slight modifications we will make to better suit our objectives.

Complete set of operators

We want to express the Hamiltonian in terms of LIOMs and their products. Below, we describe how we construct a complete and orthonormal set of operators, based on the charge and spin LIOMs. This set spans those operators within the

Hilbert space that are diagonal in the energy basis, such as the Hamiltonian itself. By fully expanding the Hamiltonian in terms of these operators, we gain a structured approach to analyzing how charge and spin LIOMs contribute to the system's dynamics.

We begin by defining a special type of inner product called the Frobenius inner product. We then build a complete and orthogonal set of operators for a single site and extend this construction to L sites. Finally, we express the Hamiltonian using this complete set and discuss how we can isolate the contribution of individual IOMs to the system's dynamics.

The Frobenius inner product

The Frobenius inner product between two operators $\hat{A}$ and $\hat{B}$ is defined as:

$$(\hat{A}, \hat{B}) = \frac{1}{N} Tr(\underline{\underline{A}}^{\dagger} \underline{\underline{B}}) \tag{2.21}$$

This inner product provides the mathematical foundation for constructing our complete set of operators.

Note that the Frobenius inner product is invariant under any unitary transformation:

$$(\hat{U}\hat{A}\hat{U}^{\dagger}, \hat{U}\hat{B}\hat{U}^{\dagger}) = (\hat{A}, \hat{B}) \tag{2.22}$$

In Section 3, we will use the invariance of the Frobenius inner product to construct a complete set of operators diagonal in the Fock basis.

An operator $\hat{A}$ is normalized if $(\hat{A}, \hat{A}) = 1$, and two operators $\hat{A}_1$ and $\hat{A}_2$ are orthogonal if $(\hat{A}_1, \hat{A}_2) = 0$.

Complete set of operators for one site

Here, we describe how we construct a complete set of operators for a one-site system, therefore, the operators are going to have a superscript (1). We start with the charge density $\hat{d}_i^{(1)}$, the magnetization $\hat{m}_i^{(1)}$ and the identity $\hat{I}_i^{(1)}$ operators.

$$\hat{d}_i^{(1)} = |\uparrow\rangle\langle\uparrow| + |\downarrow\rangle\langle\downarrow| + 2\,|2\rangle\langle 2| \tag{2.23}$$

$$\hat{m}_i^{(1)} = |\uparrow\rangle\langle\uparrow| - |\downarrow\rangle\langle\downarrow| \tag{2.24}$$

$$\hat{I}_i^{(1)} = |0\rangle\langle 0| + |\uparrow\rangle\langle\uparrow| + |\downarrow\rangle\langle\downarrow| + |2\rangle\langle 2| \tag{2.25}$$

As discussed in the previous section, the unitary operator $\hat{Q}_{opt}$ transforms the Fock state $|n\rangle$ to the energy eigenstate $|E_{a(n)}\rangle$:

$$\hat{Q}_{opt}\,|n\rangle = |E_{a(n)}\rangle \tag{2.26}$$

Hereafter, we will denote the optimized unitary operator as $\hat{Q}$ for simplicity. Applying this transformation to the charge density and magnetization operators gives us the initial version of LIOMs:

$$\begin{aligned}\hat{Q}\hat{d}_i^{(1)}\hat{Q}^\dagger &= |E_{a(\uparrow)}\rangle\langle E_{a(\uparrow)}| + |E_{a(\downarrow)}\rangle\langle E_{a(\downarrow)}| + 2|E_{a(2)}\rangle\langle E_{a(2)}| \\ \hat{Q}\hat{m}_i^{(1)}\hat{Q}^\dagger &= |E_{a(\uparrow)}\rangle\langle E_{a(\uparrow)}| - |E_{a(\downarrow)}\rangle\langle E_{a(\downarrow)}|\end{aligned} \tag{2.27}$$

The identity operator retains the same form across all bases:

$$\hat{I}_i^{(1)} = |E_{a(0)}\rangle\langle E_{a(0)}| + |E_{a(\uparrow)}\rangle\langle E_{a(\uparrow)}| + |E_{a(\downarrow)}\rangle\langle E_{a(\downarrow)}| + |E_{a(2)}\rangle\langle E_{a(2)}| \tag{2.28}$$

This initial version of this set of operators is not orthogonal, not normalized, and not complete.

Orthogonality

The initial version of the spin LIOM, $\hat{Q}\hat{m_i^{(1)}}\hat{Q}^\dagger$, is orthogonal to the identity $\hat{I}$ and initial version of the charge LIOM $\hat{Q}\hat{d_i^{(1)}}\hat{Q}^\dagger$. However, the initial version of the charge LIOM $\hat{Q}\hat{d_i^{(1)}}\hat{Q}^\dagger$ is not orthogonal to the identity $\hat{I}$.

$$\begin{aligned}(\hat{Q}\hat{d}_i^{(1)}\hat{Q}^\dagger, \hat{Q}\hat{m}_i^{(1)}\hat{Q}^\dagger) &= 0 \\ (\hat{Q}\hat{m}_i^{(1)}\hat{Q}^\dagger, I) &= 0 \\ (\hat{Q}\hat{d}_i^{(1)}\hat{Q}^\dagger, I) &\neq 0\end{aligned} \tag{2.29}$$

To address this we construct a version of the charge density operator, that is orthogonal to the identity operator:

$$\tilde{d}_i^{(1)} = (\hat{n}_{i\uparrow} + \hat{n}_{i\uparrow} - \hat{I}_i) = -|0\rangle\langle 0| + |2\rangle\langle 2| \tag{2.30}$$

By applying the unitary transformation $\hat{Q}$ to this modified charge density operator, we obtain a new version of charge LIOM that is orthogonal to the identity operator:

$$\hat{Q}\tilde{d}_i^{(1)}\hat{Q}^\dagger = -|E_{a(0)}\rangle\langle E_{a(0)}| + |E_{a(2)}\rangle\langle E_{a(2)}| \tag{2.31}$$

Now, the three operators of $I_i^{(1)}$, $\hat{Q}\tilde{d}_i^{(1)}\hat{Q}^\dagger$, $\hat{Q}\hat{m}_i^{(1)}\hat{Q}^\dagger$ are mutually orthogonal:

$$\begin{aligned}(\hat{Q}\tilde{d}_i^{(1)}\hat{Q}^\dagger, \hat{Q}\tilde{m}_i^{(1)}\hat{Q}^\dagger) &= 0 \\ (I_i, \hat{Q}\tilde{d}_i^{(1)}\hat{Q}^\dagger) &= 0 \\ (I_i, \hat{Q}\tilde{d}_i^{(1)}\hat{Q}^\dagger) &= 0\end{aligned} \tag{2.32}$$

Normalization

The current version of charge $\hat{Q}\tilde{d}_i^{(1)}\hat{Q}^\dagger$ and spin $\hat{Q}\hat{m}_i^{(1)}\hat{Q}^\dagger$ LIOMs are not yet normalized.

$$\begin{aligned}(\hat{Q}\tilde{d}_i^{(1)}\hat{Q}^\dagger, \hat{Q}\tilde{d}_i^{(1)}\hat{Q}^\dagger) &= \frac{1}{2} \neq 1 \\ (\hat{Q}\hat{m}_i^{(1)}\hat{Q}^\dagger, \hat{Q}\hat{m}_i^{(1)}\hat{Q}^\dagger) &= \frac{1}{2} \neq 1\end{aligned}$$

To normalize these operators, we multiply the operators $\hat{Q}\tilde{d}_i^{(1)}\hat{Q}^\dagger$ and $\hat{Q}\hat{m}_i^{(1)}\hat{Q}^\dagger$ by $\sqrt{2}$. We denote these normalized operators by:

$$\begin{aligned}\mathbb{d}_i^{(1)} &= \sqrt{2}\hat{Q}\tilde{d}_i^{(1)}\hat{Q}^\dagger \\ \mathbb{m}_i^{(1)} &= \sqrt{2}\hat{Q}\hat{m}_i^{(1)}\hat{Q}^\dagger\end{aligned} \tag{2.33}$$

Now, the three operators $\hat{I}_i^{(1)}$, $\mathbb{d}_i^{(1)}$ and $\mathbb{m}_i^{(1)}$ are normalized:

$$(I_i^{(1)}, I_i^{(1)}) = (\mathbb{d}_i^{(1)}, \mathbb{d}_i^{(1)}) = (\mathbb{m}_i^{(1)}, \mathbb{m}_i^{(1)}) = 1. \tag{2.34}$$

Completeness

The number of degrees of freedom of the Hamiltonian is equal to the dimension of the Hilbert space since the Hamiltonian is diagonal in the energy basis. For a single site, the Hilbert space dimension is 4, meaning one requires four operators to fully expand the Hamiltonian. So far, we have identified three operators: $\hat{I}_i^{(1)}$, $\mathfrak{d}_i^{(1)}$ and $\mathfrak{m}_i^{(1)}$. To complete the set, we need a fourth operator that is mutually orthogonal to these three. This fourth operator is derived from the following operator:

$$\begin{aligned}\tilde{o}_i^{(1)} =&(\tilde{d}_i^{(1)})^2 - (\tilde{m}_i^{(1)})^2 \\ =&\hat{I}_i^{(1)} - 2\hat{n}_{i\uparrow} - 2\hat{n}_{i\downarrow} + 4\hat{n}_{i\uparrow}\hat{n}_{i\downarrow} \\ =&|0\rangle\langle 0| - |\uparrow\rangle\langle\uparrow| - |\downarrow\rangle\langle\downarrow| + |2\rangle\langle 2|\end{aligned} \tag{2.35}$$

The operator $\tilde{o}_i$ determines the type of site i: +1 for charge-type sites and −1 for spin-type sites.

The fourth and final operator in the complete set for a single site is denoted as $\mathfrak{o}_i^{(1)} = \hat{Q}\tilde{o}_i^{(1)}\hat{Q}^\dagger$. As shown in Eq.(2.35), this operator is of second order in the LIOMs and we will therefore refer to it as the second-order on-site operator.

The operator $\mathfrak{o}_i^{(1)}$ is normalized, $(\mathfrak{o}_i^{(1)}, \mathfrak{o}_i^{(1)}) = 1$, and it is orthogonal to the other three operators: $(\mathfrak{o}_i^{(1)}, \mathfrak{d}_i^{(1)}) = (\mathfrak{o}_i^{(1)}, \mathfrak{m}_i^{(1)}) = (\mathfrak{o}_i^{(1)}, I_i^{(1)}) = 0$.

Thus, the complete and orthonormal set of operators for a single site consists of:

1. The identity operator

$$\hat{I}_i^{(1)}$$

2. the charge LIOM

$$\mathbb{d}_i^{(1)} = \hat{Q}\tilde{d}_i^{(1)}\hat{Q}^\dagger \tag{2.36}$$

3. the spin LIOM

$$\mathbb{m}_i^{(1)} = \hat{Q}\tilde{m}_i^{(1)}\hat{Q}^\dagger \tag{2.37}$$

4. the on-site 2nd-order operator

$$\mathbb{o}_i^{(1)} = \hat{Q}\tilde{o}_i^{(1)}\hat{Q}^\dagger \tag{2.38}$$

For clarity, we emphasize (i) that Eq.(2.27) through Eq.(2.38) refer to a system consisting of a single site and (ii) that the same unitary operator $\hat{Q}$ is applied in all cases.

Complete set of operators for L sites To construct the complete set of operators for L sites, we take the outer product of L operators, one for each site, chosen from the set of four single-site operators listed above. This creates a complete set of operators for L sites.

The complete set contains $N = 4^L$ operators, corresponding to the dimension of the Hilbert space. While it might initially seem that a complete set would require the square of the Hilbert space dimension, this is not the case here, as we are only expanding operators that are diagonal in the energy basis. These operators are categorized by the number of distinct LIOMs they contain, which determines their order.

For example, let's consider the complete set of operators for $L = 2$:

- Zeroth-order

$$\hat{I}^{(2)} = I_1^{(1)} \otimes I_2^{(1)}$$

- First-order

$$\mathbb{d}_1^{(2)} = \mathbb{d}_1^{(1)} \otimes I_2^{(1)}$$

$$\mathbb{d}_2^{(2)} = I_1^{(1)} \otimes \mathbb{d}_2^{(1)}$$

$$\mathbb{m}_1^{(2)} = \mathbb{m}_1^{(1)} \otimes I_2^{(1)}$$

$$\mathbb{m}_2^{(2)} = I_1^{(1)} \otimes \mathbb{m}_2^{(1)}$$

- Second-order

$$\mathbb{o}_1^{(2)} = \mathbb{o}_1^{(1)} \otimes I_2^{(1)}$$

$$\mathbb{o}_2^{(2)} = I_1^{(1)} \otimes \mathbb{o}_2^{(1)}$$

$$(\mathbb{d}_1\mathbb{d}_2)^{(2)} = \mathbb{d}_1^{(1)} \otimes \mathbb{d}_2^{(1)}$$

$$(\mathbb{m}_1\mathbb{d}_2)^{(2)} = \mathbb{m}_1^{(1)} \otimes \mathbb{d}_2^{(1)}$$

$$(\mathbb{d}_1\mathbb{m}_2)^{(2)} = \mathbb{o}_1^{(1)} \otimes \mathbb{m}_2^{(1)}$$

$$(\mathbb{m}_1\mathbb{m}_2)^{(2)} = \mathbb{m}_1^{(1)} \otimes \mathbb{m}_2^{(1)}$$

- Third-order

$$(\mathbb{d}_1\mathbb{o}_2)^{(2)} = \mathbb{d}_1^{(1)} \otimes \mathbb{o}_2^{(1)}$$

$$(\mathbb{o}_1\mathbb{d}_2)^{(2)} = \mathbb{o}_1^{(1)} \otimes \mathbb{d}_2^{(1)}$$

$$(\mathbb{m}_1\mathbb{o}_2)^{(2)} = \mathbb{m}_1^{(1)} \otimes \tilde{o}_2^{(1)}$$

$$(\mathbb{o}_1\mathbb{m}_2)^{(2)} = \mathbb{o}_1^{(1)} \otimes \tilde{m}_2^{(1)}$$

- Fourth-order

$$(\mathbb{o}_1\mathbb{o}_2)^{(2)} = \mathbb{o}_1^{(1)} \otimes \mathbb{o}_2^{(1)}$$

Among these operators, the first-order operators correspond to the charge and spin LIOMs. Higher-order operators, although representing conserved quantities, are not LIOMs. They describe couplings between charge and spin LIOMs.

Going forward, we will omit the superscript (L) since our focus is on systems with L sites.

The Hamiltonian expressed in terms of LIOMs and their products

We are using the complete set of operators we have established for L sites, we can now expand the Hamiltonian $\hat{H}$, resulting in what is known as the l-bit Hamiltonian:

$$\begin{aligned}\hat{H} =& J_0\hat{I} + \sum_i J_i^c \mathbb{d}_i + \sum_i J_i^s \mathbb{m}_i + \sum_i J_{ii}^o \mathbb{o}_i + \sum_{i,j(i>j)} J_{ij}^{cc} \mathbb{d}_i \mathbb{d}_j + \sum_{i,j(i>j)} J_{ij}^{ss} \mathbb{m}_i \mathbb{m}_j + \sum_{i,j(i\neq j)} J_{ij}^{cs} \mathbb{d}_i \mathbb{m}_j \\ &+ \sum_{i,j,k(i>j>k)} J_{ijk}^{ccc} \mathbb{d}_i \mathbb{d}_j \mathbb{d}_k + \sum_{i,j,k(i>j,k\neq i,k\neq j)} J_{ijk}^{ccs} \mathbb{d}_i \mathbb{d}_j \mathbb{m}_k + \sum_{i,j,k(i>j\neq i,k\neq i,j>k)} J_{ijk}^{css} \mathbb{d}_i \mathbb{m}_j \mathbb{m}_k \\ &+ \sum_{i,j,k(i>j>k)} J_{ijk}^{sss} \mathbb{m}_i \mathbb{m}_j \mathbb{m}_k + \sum_{ij,(i\neq j)} J_{iij}^{oc} \mathbb{o}_i \mathbb{d}_j + \sum_{ij,(i\neq j)} J_{iij}^{os} \mathbb{o}_i \mathbb{m}_j + ... \end{aligned} \tag{2.39}$$

In Eq.(2.39), the coefficients of the expansion are denoted by J_i^c, J_i^s, J_i^o, J_{ij}^{cc}, and so on. The superscripts indicate the type of the terms in the expansion, while the subscripts represent the specific sites involved. These coefficients can be determined by projecting the Hamiltonian onto each operator in the complete set; for example, $J_{ij}^{cc} = (\hat{H}, \hat{\mathbb{d}}_i \hat{\mathbb{d}}_j)$.

The first term is the zeroth-order term which consists of the identity operator. The second term is the first-order charge term which consists of the charge LIOMs, $\mathbb{d}_i$. The third term is the first-order spin term which consists of the spin LIOMs, $\mathbb{m}_i$. Additionally, the second-order terms include:

- The second-order on-site term: The fourth term in the expansion, consists of the on-site 2nd-order operators, $\mathbb{o}_i$.
- The second-order charge-charge term: The fifth term consists of pairwise

couplings of charge LIOMs, $\mathbb{d}_i\mathbb{d}_j$.

- The second-order spin-spin term: The sixth term which consists of the pairwise couplings of spin LIOMs, $\mathbb{m}_i\mathbb{m}_j$.
- The second-order charge-spin term: The seventh term consists of the pairwise couplings between charge and spin LIOMs, $\mathbb{d}_i\mathbb{m}_j$,

To determine how these LIOMs and their pairwise couplings influence the evolution of the many-body wavefunction, we truncate the l-bit Hamiltonian, retaining only specific terms.

Each truncated version of the Hamiltonian shares the same eigenstates as the full Hamiltonian, although the eigenvalues differ. In Section 3, we will describe how we determine the set of energy eigenvalues for each truncation of the l-bit Hamiltonian.

Quantifying entanglement as a function of time

To quantify the entanglement, we divide our system into two halves – the left and right subsystems – and use the bipartite von Neumann entanglement entropy (EE) as the measure.

In this section, we first define EE, then we describe how we calculate the EE in our system as a function of time, and finally, we describe the EE time-dependent behavior seen in disordered one-dimensional systems with one degree of freedom per site.

The definition of entanglement entropy

We consider the case where the full system is prepared in a pure state, represented by a single wavefunction $|\psi\rangle$. To quantify the entanglement of the right

half with the rest of the system, we analyze how much information is contained within the right subsystem. While the full system is in a pure state, the states accessible to the right subsystem are occupied with certain probabilities, indicating a level of uncertainty. EE measures this uncertainty in the state of the subsystem.

To find the possibilities that the available states to the right subsystem are occupied, we start with the density operator of the full system $\hat{\rho}_{LR}$:

$$\hat{\rho}_{LR} = |\psi\rangle\langle\psi| \tag{2.40}$$

Our numerical approach allows us to calculate the matrix representation of $\hat{\rho}_{LR}$ in the Fock basis, which is an $N \times N$ matrix.

The state of the right subsystem, which may be mixed due to entanglement, is described by a reduced density operator, $\hat{\rho}_L$:

$$\hat{\rho}_R = Tr_L[\rho_{LR}] = \sum_n (\langle\alpha|_L \otimes I_R)\rho_{LR}(|\alpha\rangle_L \otimes I_R) \tag{2.41}$$

where $\{|j\rangle_L\}$ is any basis that spans the Hilbert space of the left subsystem, H_L (e.g. the Fock basis) that has M dimension, and $\hat{I}_R$ is the identity operator for the right subsystem. Using Eq.(2.41) and the Fock representation of the ρ_{LR}, we can find the matrix representation of $\hat{\rho}_R$, which is an $M \times M$ matrix.

We find the eigenvalues p_i and eigenstates $|\phi\rangle_i$ of ρ_R.

Our knowledge about the right subsystem is described by the ensemble $\{p_i, |\phi_i\rangle | i = 1, ...M\}$, where $\{|\phi_i\rangle\}$ is an orthonormal basis that spans the right subsystem's Hilbert space. The eigenvalues $\{p_i\}$ are the probabilities of the states $\{|\phi_i\rangle\}$ are being occupied, which sum to one ($\sum_{i=1}^{M} p_i = 1$).

The EE, which quantifies the uncertainty about the state of the right subsystem given the full system's state, is defined as [18]:

$$S = -\sum_i p_i \log_2 p_i \tag{2.42}$$

Time dependence

Here, we analyze how EE evolves over time, starting from a product state. A product state implies that there is no initial entanglement between subsystems. In this case, the full system state $|\psi\rangle$ can be expressed as :

$$|\psi\rangle = |\phi\rangle_L |\phi\rangle_R \tag{2.43}$$

Initially, only one non-zero probability $p_i = 1$ exists in the ensemble of the right subsystem, resulting in zero EE, $S(0) = 0$, which reflects complete knowledge of the subsystem's state.

At time t, the wavefunction evolves to $|\psi(t)\rangle$ under the Hamiltonian while remaining a pure state. For a Hamiltonian with eigenvalues $\{E_n\}$ and eigenstates $\{|E_n\rangle\}$, the time evolution is given by:

$$\begin{aligned}
|\psi(t)\rangle &= e^{-i\hat{H}t} |\psi(0)\rangle \\
&= e^{-i\hat{H}t} (\sum_n |E_n\rangle \langle E_n|) |\psi(0)\rangle \\
&= \sum_n e^{-i\hat{H}t} |E_n\rangle \langle E_n|\psi(0)\rangle \\
&= \sum_n e^{-iE_n t} \langle E_n|\psi(0)\rangle |E_n\rangle
\end{aligned}$$

We determine the EE at a specific time t using $|\psi(t)\rangle$ and following the steps outlined in Section 2.

The maximum value of EE, $S_{max} = log_2(M)$, occurs when the subsystem is maximally mixed, meaning the probabilities $\{p_i\}$ are equally distributed among all possible states of the subsystem. This state represents minimal knowledge about the subsystem.

Time dependent behavior of entanglement entropy in a disordered system

Below, we describe what is already known about the time-dependent behavior of EE in a disordered one-dimensional lattice with a single degree of freedom.

Non-interacting system:

In a non-interacting system, the many-body state is determined by the occupations of single-particle eigenstates. These eigenstates are spatially localized due to disorder, with their amplitudes decaying exponentially with distance as $e^{\frac{-|i-j|}{\xi}}$, where i and j are lattice sites and ξ is the localization length.

To illustrate, consider a particle initially located on a single site in the right subsystem. Its wavefunction, represented as a delta function in real space, corresponds to a weighted sum of Anderson localized eigenstates, with the weights determined by the eigenstates' amplitudes at the initial site. The squared magnitude of each coefficient in the sum represents the occupation probability of the corresponding eigenstate.

As the wavefunction evolves, it spreads over a distance determined by the localization length, ξ. If this extends across the boundary between left and right subsystems, then this spreading increases the uncertainty in the state of the right subsystem, and the off-diagonal terms of the reduced density matrix ρ_L decrease, leading to a rapid rise in EE.

When the wavefunction fully spreads, the magnitude of the off-diagonal terms in the reduced density matrix stabilizes and the EE saturates. The saturation value is independent of system size and is determined by the characteristic localization length, ξ.

Interacting system:

Here, we consider weak interactions, allowing the many-body state to be still approximated as particles occupying Anderson localized single-particle states. These interactions modify the dynamics by introducing small differences in the energy eigenvalues and creating couplings between localized eigenstates.[17]

To illustrate, consider two particles in different Anderson-localized single-particle eigenstates on opposite sides of the subsystem boundary, separated by a distance x. Interactions introduce couplings between these two states. The overlap of the two wavefunctions decays exponentially with distance, and the interaction energy is proportional to this overlap, $V \propto e^{-x/\xi}$. The timescales associated with these couplings, which scale as $\hbar/V$, increase exponentially with distance, $t \propto e^{x/\xi}$. At early times, interactions primarily affect particles near the subsystem boundary on opposite sides. Over longer times, particles farther from the boundary are influenced by the interactions, with the distance scaling as $x \propto \ln(t)$. As the interactions couple particles farther away, the off-diagonal terms of the reduced density matrix ρ_L corresponding to each pair of single-particle states, decay with time, leaving only the corresponding diagonal terms, which represent the occupation probabilities of the Anderson-localized single-particle states. Consequently, the entanglement entropy grows logarithmically with time in MBL systems with a single degree of freedom per site, as mentioned in Section 1.

In larger systems, more pairs of particles at increasingly large separations contribute to the growth of EE. However, the growth is ultimately bounded by the

finite size of the system, as entanglement cannot spread beyond its spatial extent.

Coding and Test Runs

In this chapter, we describe the conventions used to develop our code and present the results of the test runs to check the validity of our calculations. The chapter contains five sections:

- Eigenstates and time evolution

  We represent the process of building the Hamiltonian and then diagonalizing it to find the energy eigenstates that, in turn, are used to find the system's state at any time.

- Entanglement entropy

  We explain the process of building the density matrix and partial tracing to find the reduced density matrix for the right half of the system that gives us the entropy of entanglement between the right and the left halves.

- Hungarian Algorithm

  We describe the Hungarian algorithm to find the unitary transformation matrix that makes the integrals of motion as local as possible. We also present the primary question of our thesis.

- Local integrals of motion and l-bit Hamiltonian

  We describe how we can construct the LIOMs using the optimized unitary transformation matrix. We also describe how we calculate the coefficients in the l-bit Hamiltonian.

- Averaging

We describe the averaging procedure for the observables and specify the quantities over which we are averaging.

Eigenstates and time evolution

In this section, we describe how we construct the Hamiltonian in the Fock basis, obtain the eigenvalues and eigenstates, find the time-dependent wave-function and density matrix, and the tests we have run to check these aspects of the code.

Hamiltonian

In this part, we discuss the construction and storage of the Hamiltonian matrix in the Fock representation. First, we allocate the required memory for an $N \times N$ Hamiltonian matrix, called *ham1*, for a system with the Hilbert space of dimension N. We initialize all the elements of *ham1* as zeros. This approach arranges the elements of *ham1* in contiguous units of memory and, in turn, optimizes access to them during the diagonalization process.

We developed an object in C++, called *ham-obj*, and use it to access three built-in functions – *hopping*, *hubbard*, and *disorder* – which update the non-zero elements of the matrix stored in *ham1*. The code destroys the created object of *ham-obj* after constructing the Hamiltonian, leaving only the updated *ham1* in memory.

In the following, we first describe the representation of the Fock basis set in our program. Then, we describe how the three functions of the *ham-obj* update the corresponding non-zero elements of the *ham1*.

Fock basis

Before we start describing the three built-in functions of *ham-obj*, we explain the preparation of the Fock basis set. We assign an unsigned integer to each basis state, where the binary representation of the integer encodes the occupation of each site in that particular basis state.

A set of four states spans the Hilbert space of a single site. Integers ranging from 0 to 3 label each occupation, and the corresponding binary representation encodes the configurations as shown in Table 3.1.

state as integer	binary representation	site occupation
0	0 0	
1	0 1	↑
2	1 0	↓
3	1 1	2

Table 3.1: All the states of a one-site system represented as a base-10 integer, a base-2 integer and symbolically.

Expanding to a 2-site system, each half (left and right) consists of a single site, resulting in a Hilbert space of dimension $4^2 = 16$, and 4-bit values running from 0 to 15 encode the Fock states. As shown in Table 3.2, we assign the appropriate pair of bits to each half - the right pair to the right half and the left pair to the left half. We adopt a right-to-left convention because, in C++ (and most computer architectures), bits are indexed starting from the least significant bit on the right, typically representing 2^0. For example, our encoding scheme represents the up-down state as:

$$|\uparrow\downarrow\rangle = ([01][10]) = \left|2^2 + 2^1\right\rangle = |6\rangle\,.$$

The square brackets are included only to emphasize the left and right halves of the system.

In a 4-site system, the Hilbert space has dimension $4^4 = 256$, with Fock state

Table 3.2: All the states of a two-site system represented as a base-10 integer, bits and symbolically.

state as base-10 integer	state as bits	the occupation of the sites
0	0 0 0 0	☐ ☐
1	0 0 0 1	☐ ↑
2	0 0 1 0	☐ ↓
3	0 0 1 1	☐ 2
4	0 1 0 0	↑ ☐
5	0 1 0 1	↑ ↑
6	0 1 1 0	↑ ↓
7	0 1 1 1	↑ 2
8	1 0 0 0	↓ ☐
9	1 0 0 1	↓ ↑
10	1 0 1 0	↓ ↓
11	1 0 1 1	↓ 2
12	1 1 0 0	2 ☐
13	1 1 0 1	2 ↑
14	1 1 1 0	2 ↓
15	1 1 1 1	2 2

labels ranging from 0 to 255. Each state is stored using 8 bits or 1 byte. The rightmost 4 bits represent the state of the right half, while the leftmost 4 bits represent the state of the left half, as depicted in Figure 3.1. The sites are numbered from right to left, labeled 0 to 3, with each site's state represented by two bits.

Using this encoding scheme, the up-down-up-down state in a 4-site system is

$$|\uparrow\downarrow\uparrow\downarrow\rangle = |[0110][0110]\rangle = \left|2^6 + 2^5 + 2^2 + 2^1\right\rangle = |102\rangle\,,$$

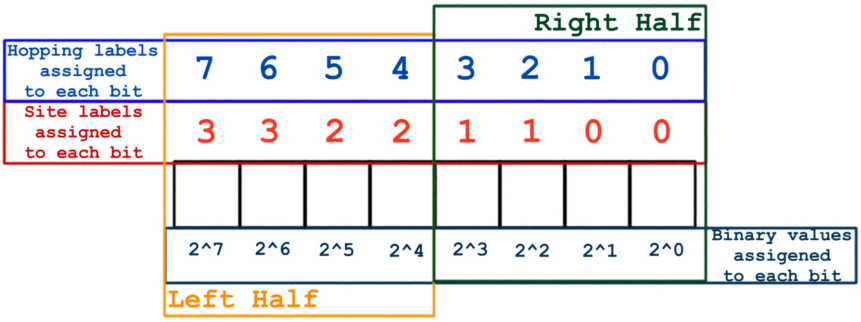

Figure 3.1: A schematic diagram of a state for a 4-site system as an object specified by a byte. The right 4 bits represent the right sub-space and the left 4 bits represents the left sub-space. The blue labels represent the bit's position that is used to construct the hopping part of the Hamiltonian. The red labels assign each pair of bits to one site in an ascending order from right to left. The numbers below the figure show the values assigned to each bit in a variable of type unsigned integer in the C++ programming language.

Hopping term

The function *hopping* adds the hopping elements to the Hamiltonian matrix. Specifically, we are looking for matrix elements for which:

$$\langle m|\, H_{hopping}\, |n\rangle \neq 0 \tag{3.1}$$

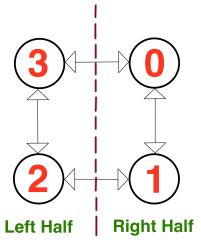

Figure 3.2: Schematic of first-nearest neighbour hopping in a 4-site system with periodic boundary conditions.

We hard-code all possible scenarios of hopping for a given system size in this function using two arrays called *hopmatrixup* and *hopmatrixdo* for the spin up and down particles, respectively. The dimension of the hopping arrays depends on the boundary conditions. With periodic boundary conditions, we have one more column in the hopping array compared with open boundary conditions corresponding to hopping from the last site to the first one.

To hard-code the hopping part, we use the labeling convention shown in Figure 3.1. Even hopping labels correspond to spin up, and odd hopping labels to spin down.

As an example, the hopping scenarios of a 4-site system are shown schematically in Figure 3.2 where the corresponding arrays are:

$$hopmatrixup = \begin{bmatrix} 0 & 2 & 4 & 6 \\ 2 & 4 & 6 & 0 \end{bmatrix}$$

$$hopmatrixdo = \begin{bmatrix} 1 & 3 & 5 & 7 \\ 3 & 5 & 7 & 1 \end{bmatrix}$$

Each column of *hopmatrixup* says that spin-up particles might hop between the bit labeled with the number in the first row and the one in the second row. For instance, the first column expresses the possibility of a spin-up particle moving from site 0 (bit 0) to site 1 (bit 2) or the reverse. The last column says spin-up particles might also hop between site 0 (bit 0) and site 3 (bit 6), establishing periodic boundary conditions.

For each column in *hopmatrixup* and *hopmatrixdo* we construct a mask. The mask is an integer that, in binary, specifies two bits belonging to two neighbour sites.

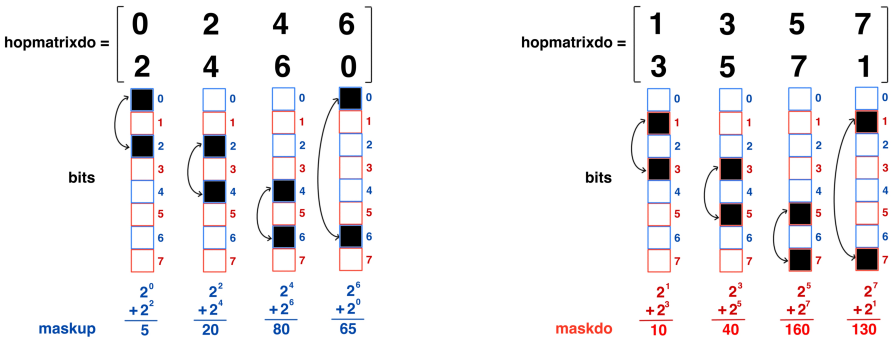

(a) spin-up (b) spin-down

Figure 3.3: The masks for hopping of spin-up(a) and spin-down(b) particles of the 4-site system, based on *hopmatrixup* and *hopmatrixdo* arrays, respectively. The bits highlighted in blue belong to spin-up particles, while the ones in red belong to spin-down particles. The double-headed arrows represent the corresponding hopping scenario.

For example, we construct $maskup = 2^0 + 2^2 = 5$ using the first column in *hopmatrixup*. All the masks for spin-up and spin-down particles are shown in Figure 3.3.

Next, for each Fock state $|n\rangle$, we execute a bitwise AND (&) between n and each *maskup* and between n and each *maskdo*, storing the results in *ku* for spin-up and *kd* for spin down particles, respectively.

$$ku = maskup \ \& \ n$$

$$kd = maskdo \ \& \ n$$

ku and *kd* show which sites in the mask are occupied in state $|n\rangle$. Next, we perform an XOR ($\wedge$) operation between *ku* and each *maskup* and between *kd* and each *maskdo*, and store the results in *lu* and *ld*, respectively.

$$lu = maskup \ \wedge \ ku$$

$$ld = maskdo \ \wedge \ kd$$

If *lu* or *ld* is nonzero and unequal to its corresponding *maskup* or *maskdo*, then the hopping is possible and the resulting state $|m\rangle$ is

$$m = n\text{–}ku + lu$$

or

$$m = n\text{–}kd + ld.$$

Subtracting *ku* (*kd*) from *n* removes the ↑ (↓) particle from the corresponding site in the *maskup* (*maskdo*) and adding *lu* (*ld*) adds it to the other site in the same mask, while the spin-down (spin-up) part remains unchanged. This process acts like the $c_i^\dagger c_j$ operators in the hopping term in the Hamiltonian. So, practically, we operate hopping to find the resulting state $|m\rangle$.

A hopping term can be either positive or negative, depending on the correspondence between fermionic creation operators and Fock states. To ensure consistency, we use a specific convention: $c_\uparrow^\dagger$ operators are positioned to the right of $c_\downarrow^\dagger$ operators, with site indices ordered from left to right. With this convention, all hopping terms to nearest neighbors acquire a negative sign. For example, consider the action of the hopping operator $-[c_{1\uparrow}^\dagger c_{2\uparrow}]$ on the state $|2\ \downarrow\rangle$:

$$\begin{aligned}
-[c_{1\uparrow}^\dagger c_{2\uparrow}]\,|2\ \downarrow\rangle &= -\,[c_{1\uparrow}^\dagger c_{2\uparrow}](c_{1\downarrow}^\dagger c_{2\downarrow}^\dagger c_{2\uparrow}^\dagger\,|\rangle) \\
&= -\,(c_{1\downarrow}^\dagger(-1)(-1)[c_{1\uparrow}^\dagger c_{2\uparrow}]c_{2\downarrow}^\dagger c_{2\uparrow}^\dagger\,|\rangle) \\
&= -\,(c_{1\downarrow}^\dagger c_{2\downarrow}^\dagger(-1)(-1)[c_{1\uparrow}^\dagger c_{2\uparrow}]c_{2\uparrow}^\dagger\,|\rangle) \\
&= -\,(c_{1\downarrow}^\dagger c_{2\downarrow}^\dagger c_{1\uparrow}^\dagger(1 - c_{2\uparrow}^\dagger c_{2\uparrow})\,|\rangle) \\
&= -\,(c_{1\downarrow}^\dagger c_{2\downarrow}^\dagger c_{1\uparrow}^\dagger\,|\rangle) = -\,|\uparrow\ 2\rangle
\end{aligned} \tag{3.2}$$

Finally, the function *hopping* sets the allocated memory of $ham1_{mn}$ to −1 and iterates the process for all *n*.

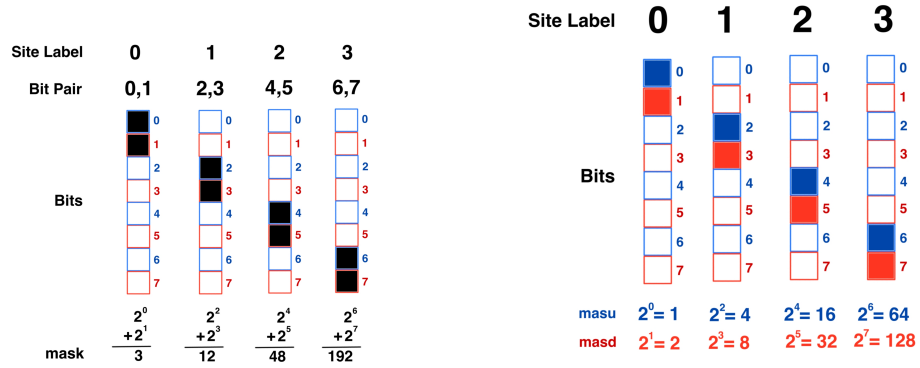

(a) hubbard (b) disorder

Figure 3.4: (a) The masks for the Hubbard term. The blue and red bits belong to spin-up and spin-down particles, respectively, and (b)the masks used to determine the state of each site and hence add the site potentials and local magnetic fields to the Hamiltonian matrix for a 4-site system. The bits highlighted in blue belong to spin-up particles, while the ones in red belong to spin-down particles.

Hubbard term

The *hubbard* function adds the Hubbard term to the *ham1* matrix. The process is similar to the hopping function, but the masks here are different, $mask = 2^k + 2^{k+1}$, where k is the site label. Figure 3.4 shows all the *hubbard* masks for a 4-site system.

Because the Hubbard term does not change the Fock state, it contributes only to the diagonal elements of the Hamiltonian. We perform a bitwise AND (&) operation between the state number i and each one of the *mask*s and store the result in pt

$$pt = mask \,\&\, i$$

If pt is equal to the *mask*, it means the corresponding site is doubly occupied, so we add U to $ham1_{ii}$. We repeat the process for all the *hubbard* masks and then iterate for all the integers, i.

Disorder term

The *disorder* function adds the site potentials and local magnetic fields to the *ham1*. Like the Hubbard term, the disorder terms do not change the Fock state, and the resulting elements are on the diagonal of the *ham1*.

For state $|j\rangle$, we need to see which bits are non-zero to find the site label and spin type of the particles and then add the corresponding values to the *ham1*. To find if a spin-up particle is on site k we use *masu* corresponding to site k (as shown in Figure 3.4).

We perform an AND (&) operation between *masu* and j, storing the results in *pu* and likewise for spin-down.

$$pu = masu \ \& \ j \text{ for spin-up}$$

$$pd = masd \ \& \ j \text{ for spin-down}$$

Now, we find the state of the site k in the state $|j\rangle$:

- When $masu \neq pu$ and $masd \neq pd$ the state of the site k is 0.
- When $masu = pu$ and $masd \neq pd$ the state of the site is $\uparrow$
- etc.

The *disorder* function adds the corresponding disorder value to $ham1_{j\,j}$ and iterates the process for all the integers j.

Eigenvalues and eigenstates

Here, we describe how we diagonalize the Hamiltonian matrix and store the eigenvalues and eigenvectors. We use the *Eigen* library – a standard linear algebra library developed in *C++* language – for matrix diagonalization.

Our code stores the eigenvectors in a two-dimensional square array where column n represents the energy eigenstate $|E_n\rangle$ in the Fock basis:

$$(\vec{E_n})_F = \begin{pmatrix} \langle 0|E_n\rangle \\ \langle 1|E_n\rangle \\ \vdots \\ \langle k|E_n\rangle \\ \vdots \\ \langle N-1|E_n\rangle \end{pmatrix} \tag{3.3}$$

where, $\{|k\rangle\}$ are the Fock basis, and N is the dimension of the Hilbert space.

Our code also stores the eigenvalues in a one-dimensional array where the nth element of the array corresponds to the eigenvalue E_n of the eigenstate $|E_n\rangle$. The eigenstates and the eigenvalues are real because the Hamiltonian matrix is Hermitian.

The Fock space inverse participation ratio

The Fock space inverse participation ratio (FIPR) is a measure to quantify how spread out or localized an energy eigenstate, $|E_n\rangle$, is across different states, $|n\rangle$, in the Fock space.[46] We calculate the average FIPR value of all the N eigenstates as:

$$FIPR = \frac{\sum_i \sum_n (\langle n|E_i\rangle)^4}{N}, \tag{3.4}$$

If FIPR is close to 1, the energy eigenstates are concentrated in a few Fock states. A small FIPR, close to $\frac{1}{dim(\text{Fock space})}$, implies that the energy eigenstates are spread across many Fock states.

Time evolution and density matrix

The state of the system changes from $\left|\psi(0)\right\rangle$ at initial time to $\left|\psi(t>0)\right\rangle$ at later times. In the Fock representation,

$$\vec{\psi}(t>0)_F = \begin{pmatrix} \sum_n e^{-iE_n t} \left\langle E_n \middle| \psi(0) \right\rangle \langle 0|E_n\rangle \\ \sum_n e^{-iE_n t} \left\langle E_n \middle| \psi(0) \right\rangle \langle 1|E_n\rangle \\ \vdots \\ \sum_n e^{-iE_n t} \left\langle E_n \middle| \psi(0) \right\rangle \langle k|E_n\rangle \\ \vdots \\ \sum_n e^{-iE_n t} \left\langle E_n \middle| \psi(0) \right\rangle \langle N-1|E_n\rangle \end{pmatrix} \tag{3.5}$$

We use $\langle k|E_n\rangle$, the elements of the energy eigenstates in the Fock representation, and E_n, the eigenvalues that we find as shown in section 3, and Eq. (3.5) to calculate the state of the system and store it in a complex-valued one-dimensional array. We can determine the complete density matrix using the outer product of the state vector: $\rho(t) = \left|\psi(t)\right\rangle \left\langle\psi(t)\right|$. However, as will be discussed in Section 3, we only calculate the specific elements that are necessary.

Test runs for eigenstates and density matrix

We ran the following tests to evaluate the precision of our calculations. These tests were run on 2-site and 4-site systems using double-precision floating point

numbers:

1. Test of the Hamiltonian:

   We compare the Hamiltonian matrix of a 2-site system generated by our code with that calculated by hand. The Hamiltonian constructed by the program matches the Hamiltonian calculated by hand.

2. Test of eigenvalues:

   We have an alternative code for diagonalizing the Hamiltonian matrix. This code first uses the *tred2* function to transform the Hamiltonian matrix into a tridiagonal form, followed by the *libt* function to diagonalize the resulting tridiagonal matrix. We compare the eigenvalues of the Hamiltonian obtained from our code with those from the alternative code. The difference between corresponding eigenvalues obtained from our code and the alternative code has a maximum magnitude of 10^{-12} across all eigenvalues.

3. Test of eigenvalue equation:

   We compare the two sides of the eigenvalue equation, $H|E_n\rangle = E_n|E_n\rangle$. The result shows that the difference between corresponding elements on the two sides has a maximum magnitude of 10^{-12}. This indicates that the eigenvalue equation holds a precision of 12 decimal places.

4. Orthonormalization test of eigenstates:

   We calculate the inner products of the eigenvectors $\langle E_m|E_n\rangle$ for all ms and ns to check the orthonormalization of the energy basis. The deviation from perfect orthonormalization has a maximum magnitude of 10^{-14}. This indicates that the energy basis is orthonormalized to a precision of 14 decimal places.

5. Purity of Total Density Matrix:

Starting from three different initial states - the up-down state, the first excited state, and a linear combination of energy eigenstates - we calculate the deviation from the purity of the total density matrix, $Tr[\rho^2] - 1$, at 40 arbitrary times t within the range $[10^{-3}, 10^8]$. In all cases, the density matrix remains pure to a precision of 13 decimal places.

The tests provide confidence in our results up to 12 digits.

Entanglement Entropy

In this section, we describe how our code calculates the reduced density matrix and report our test runs.

Method

Once we have the $N \times N$ density matrix ρ, our goal is to calculate the partial trace over the left half (dimension $M = \sqrt{N}$):

$$\rho_R \equiv Tr_L[\rho] = \sum_{j=0}^{M-1} (\langle\, j \,|_L \otimes I_R)\rho(|\, j \,\rangle_L \otimes I_R). \tag{3.6}$$

where $\{\, |j\,\rangle_L\}$ is any basis set that spans the Hilbert space of the left subsystem and I_R is the identity operator for the right subsystem. Using the Fock basis set for the left subsystem, the reduced density matrix ρ_R is an $M \times M$ array with complex values.

$$(\rho_R)_{ij} = \sum_{m=0}^{M-1} c_{M,m+i}\, c^*_{m,M+j} \tag{3.7}$$

where $c_{a,b} = \langle (aM + b) \big| \psi(t) \rangle$ is a coefficient with double subscripts. For more

detail, see Appendix A. To calculate ρ_R using Eq.(3.7), we only need to store the elements of $\vec{\psi}(t > 0)_F$ (Eq. (3.5)), without calculating and storing the entire density matrix ρ.

We then diagonalize ρ_R to find M eigenvalues p_i $(i = 0, M-1)$ and iterate the process for different times t. Finally, the EE is

$$S(t) = -\sum_{i}^{M} p_i(t) \ln p_i(t) \tag{3.8}$$

Test runs for Entanglement entropy

We ran the following tests to evaluate how accurately the reduced density matrix calculated by our code reflects the physical properties expected of a density matrix. These tests were run on 2-site and 4-site systems for each of the following initial conditions: the up-down state, an energy eigenstate, and a linear combination of the energy eigenstates.

1. Test of the reduced density matrix:

   We compare the reduced density matrix of a 2-site system obtained by our code with that calculated by hand. For each initial condition, the resulting matrix obtained by the code is equal to the corresponding matrix calculated by hand.

2. Non-negativeness and Reality of the Reduced Density Matrix:

   Eigenvalues of a Hermitian matrix, such as a density matrix, are real-valued, but calculating eigenvalues of a complex-valued matrix numerically always produces small imaginary parts that can be used as an indication of accuracy.

   We calculated the eigenvalues of the reduced density matrices for the above initial states, each for 40 arbitrary times within the range $[10^{-3}, 10^{8}]$. The

imaginary parts of the eigenvalues have a maximum magnitude of 10^{-8}, and the real parts of the eigenvalues are consistently positive.

3. The sum of the eigenvalues of the reduced density matrix:

   The eigenvalues of the density matrix, p_i, are probabilities and hence must sum to one. In this test, we calculate the deviation from this value, $\Delta = 1 - \sum_{i=0}^{M-1} p_i(t)$. We do this for the above three initial states, each at 40 times. The deviation has a maximum magnitude of 10^{-7}.

The tests confirm that the density matrices' eigenvalues are real (accurate to 8 decimal places), positive, and sum to one (accurate to 7 decimal places).

The Hungarian Algorithm

Sections 3 and 3 have detailed the calculation of the wavefunctions and the EE as a function of time. Our goal is to connect the EE time-dependent behavior with LIOMs as described in Section 2. Our next step must therefore be to identify the LIOMs. A key step is choosing the order of the columns in U to make it as close as possible to the identity. We use a process called the Hungarian algorithm to do this.[47]

The Hungarian algorithm was developed to efficiently solve a problem called the assignment problem. In this section, we will first introduce the assignment problem, describe the Hungarian algorithm, and explain how we use the algorithm to find the optimal column permutation of the U matrix. Finally, we present the primary question of our thesis.

The assignment problem

The assignment problem has multiple versions, and we are interested in the simplest one. It involves a set of N agents and N tasks. Each task can be assigned to any agent, but the cost of assigning a specific task to a specific agent may vary, and all assignment costs are positive. The goal is to assign each task to exactly one agent in such a way that the total cost is minimized. The assignment with minimum cost is called the optimal assignment.

This problem can be represented by an $N \times N$ matrix of positive values called the cost matrix. In this matrix, each row represents a task, and each column represents an agent. The elements of the cost matrix indicate the cost of assigning an agent to a task.

The number of possible assignments $(N!)$ grows dramatically as the size of the cost matrix N increases. In this case, a brute-force search to explore every possible assignment to find the optimal one becomes computationally infeasible.

Overview of the Hungarian algorithm

The Hungarian algorithm solves the assignment problem without having to explore every possible assignment. The algorithm adjusts the cost matrix by adding or subtracting a constant from all elements in a row or column. The adjustment does not alter the relative costs, and thus the optimal assignment for the adjusted cost matrix is identical to the one for the original matrix. The goal of adjusting the matrix is to create a scenario where each column of the matrix contains exactly one zero, with each zero located in a different row. These specific zeros are labeled as ”starred” zeros.

Here we provide an overview of the iterative process, further details are provided in Appendix A.

The algorithm begins by subtracting the smallest element in each row from all elements in that row, ensuring that each row has at least one zero. The next step is to identify and star one zero in each row, marking the corresponding columns as ”covered”.

In each iteration, some rows may contain multiple zeros, therefore, the algorithm must decide which zero to mark as starred in that row. The algorithm marks these rows as covered and then selects starred zeros in a way that maximizes the number of covered columns.

If the number of covered columns equals the size of the matrix (N), the algorithm has found the optimal assignment. If the number of covered columns is less than N, the algorithm identifies the smallest uncovered element in the matrix, subtracts this value from all uncovered elements, and adds it to covered rows. By each iteration, the algorithm progresses toward covering all columns with exactly one starred zero.

The solution to the assignment problem is represented by a one-dimensional array of integers called the assignment array:$\{a_0, a_1, \dots, a_{N-1}\}$. In this array, the ith element indicates the row number of the starred zero in column i, meaning that the task a_i is assigned to the agent i. The Hungarian algorithm delivers this optimal solution with a time complexity of approximately $O(N^3)$ for an $N \times N$ cost matrix.

Our implementation

As detailed in section 3, we store the matrix U as a two-dimensional array. The columns of U are normalized energy eigenstates in the Fock basis. Because the Hamiltonian is not only Hermitian but also real, the elements of these vectors are real values ranging from -1 to 1. Initially, these are organized from left to right in ascending order of their corresponding energy eigenvalues.

Our objective is to rearrange the columns of U in a manner that places the maximum total weight on the diagonal and hence makes the matrix as close as possible to the identity matrix. This problem can be framed as an assignment problem.

In this context, the columns of U correspond to energy eigenstates $|E_n\rangle$, while the rows correspond to Fock states $|n\rangle$. The elements of the matrix, $\langle n|E_n\rangle$, represent the projection of a Fock state onto an eigenstate. Our goal is to maximize the total cost, leading to a column arrangement that closely approximates the identity matrix.

Since we are looking to maximize the total cost rather than minimize the total cost, and given that the elements of U are not all positive, we modify the matrix U before applying the Hungarian algorithm.

i Positivity

We make the elements positive by taking the absolute value of U. (An alternative is to square the elements, which we explore in Chapter 4).

ii Reversing maximum and minimum

We then adjust the matrix further by applying the following operation to each element:

$$A'_{ij} = 1 - |U_{ij}|, \tag{3.9}$$

This operation reverses the magnitude of the elements, turning the maximum values in U into minimum values in A'. As a result, the modified matrix A' contains real-valued elements between 0 and 1.

This process reverses the order of the relative magnitude of the elements so that the elements with maximum values in U become the elements with minimum values in A'.

To mitigate arithmetic errors introduced by using floating point numbers in the

Hungarian algorithm, we convert the elements of A' into integers:

$$A_{ij} = floor(A'_{ij} \times 10^{n_{HA}}) \tag{3.10}$$

We refer to n_{HA} in Eq. (3.10) as the accuracy of the Hungarian algorithm. The resulting matrix A is an $N \times N$ integer-valued cost matrix, with elements ranging between 0 and $10^{n_{HA}}$.

Applying the Hungarian algorithm to matrix A yields the optimal assignment with minimum cost. This assignment corresponds to the arrangement of columns in U that makes the matrix as close as possible to the identity matrix, denoted as U_{opt}.

Consider the following example matrix U:

$$U = \begin{pmatrix} 0.5914 & -0.4345 & 0.8051 \\ -0.4988 & 0.3629 & 0.8196 \\ 0.2893 & 0.7632 & -0.0013 \end{pmatrix} \tag{3.11}$$

After the above adjustments with $n_{HA} = 1$, we obtain:

$$A = \begin{pmatrix} 4 & 5 & 1 \\ 5 & 6 & 1 \\ 7 & 2 & 9 \end{pmatrix} \tag{3.12}$$

As detailed in Appendix A, implementing the Hungarian algorithm on A produces the optimal assignment array $\{1, 3, 2\}$, indicating the assignment with minimum total cost in A.

Therefore, this indicates that in U_{opt}, column 1 of U goes first, then column 3 of U, and finally column 2 of U.

$$U_{opt} = \begin{pmatrix} 0.5914 & 0.8051 & -0.4345 \\ -0.4988 & 0.8196 & 0.3629 \\ 0.2893 & -0.0013 & 0.7632 \end{pmatrix} \tag{3.13}$$

In our code, the *Hungarian* function implements the Hungarian algorithm on the matrix U. The input to this function consists of the matrix, *es*, of energy eigenstates organized in ascending order. The output of the *Hungarian* function is a one-dimensional assignment array that provides the optimal column assignment.

The primary question of our thesis

Our goal is to explore how the charge and spin degrees of freedom contribute to the growth of entanglement in the disordered Hubbard chain. One issue is how accurately the constructed LIOMs represent the localized behavior of the charge and spin degrees of freedom in our MBL system.

We hypothesize that increasing the accuracy of the Hungarian algorithm affects the column order in the resulting matrix U_{opt}, leading to a more optimized U matrix. The second-order truncated l-bit Hamiltonian constructed with this optimized U_{opt} should capture the EE time dependence of the exact Hamiltonian more accurately.

The first question we address is: Does increasing the accuracy of the Hungarian algorithm reduce the observed vertical offset between the EE obtained from the

exact Hamiltonian and the EE obtained from the 2nd-order truncated Hamiltonian? We will discuss the impact of n_{HA} on the EE obtained from the second-order truncated Hamiltonian in Chapter 4. In addition, we will provide results relevant to the broader question of how charge and spin degrees of freedom contribute to EE.

Test of our implementation of the Hungarian Algorithm

We tested our implementation of the Hungarian algorithm using a sample of 10,000 randomly generated 6×6 matrices. The elements of each matrix were random floating point numbers between -1 and 1, with each column normalized.

The test compared the results of the Hungarian algorithm (using $n_{HA} = 7$ for precision) with those obtained by brute-force methods, which involve checking all possible permutations of the columns ($6! = 720$) to find the arrangement with the maximum diagonal weight.

We found that the Hungarian algorithm and the brute-force method produced identical assignment arrays consistently for all 10,000 samples.

We also observed a significant difference in the processing time between the two methods. The Hungarian algorithm took an average processing time of $1.3\mu s$ per matrix. On the other hand, the brute-force method took an average time of $144.5\mu s$ per matrix.

Integrals of motion and l-bit Hamiltonian

In Section 3, we detailed the process of optimally assigning Fock states to energy eigenstates. Building on this assignment, the next step is constructing the matrix representation of the LIOMs and the complete set of operators. Our goal is to

analyze how LIOMs and their pairwise products in the complete set contribute to the energy eigenvalues of the l-bit Hamiltonian and, consequently, to the time-dependent behavior of EE, as discussed in Section 2.

This section begins by describing the construction of the matrix representation of the LIOMs in the energy basis. However, there are fewer computational steps needed, if instead of transforming to the energy basis, the calculations are performed directly in the Fock basis.

We explain the process of constructing the complete set of operators in the Fock basis and calculating the coefficients in the l-bit Hamiltonian using this set. Following that, we describe the procedure for finding the energy eigenvalues of different versions of the truncated l-bit Hamiltonian. The section concludes with the results of validation tests.

Local integrals of motion

Here, we describe how we can construct the matrix representation of LIOMs in the energy basis.

The first step is to find the matrix representation of the orthonormalized local charge density, $\tilde{d}_i$, and magnetization, $\tilde{m}_i$, operators in the Fock basis. For an L-site system, the matrix representation of $\tilde{d}_i$ (or $\tilde{m}_i$) is constructed by taking the outer product of $\underline{\underline{\tilde{d}}}_i^{(1)}$ ($\underline{\underline{\tilde{m}}}_i^{(1)}$)) on site i with the identity matrix, $\underline{\underline{I}}_j^{(1)}$, on the other sites $j \neq i$. The single-site operators in the outer product are arranged from right to left. For example, in a system of size $L = 2$:

$$\underline{\underline{\tilde{d}}}_0 = \underline{\underline{I}}^{(1)}_1 \otimes \underline{\underline{\tilde{d}}}^{(1)}_0 \tag{3.14}$$

$$\underline{\underline{\tilde{d}}}_1 = \underline{\underline{\tilde{d}}}^{(1)}_1 \otimes \underline{\underline{I}}^{(1)}_0 \tag{3.15}$$

$$\underline{\underline{\tilde{m}}}_0 = \underline{\underline{I}}^{(1)}_1 \otimes \underline{\underline{\tilde{m}}}^{(1)}_0 \tag{3.16}$$

$$\underline{\underline{\tilde{m}}}_1 = \underline{\underline{\tilde{m}}}^{(1)}_1 \otimes \underline{\underline{I}}^{(1)}_0 \tag{3.17}$$

The resulting matrix for each outer product is an $N \times N$ diagonal matrix, where $N = 4^L$ is the dimension of the Hilbert space. For each site i, we construct the matrix representations of $\tilde{d}_i$ and $\tilde{m}_i$ and record the diagonal elements in a $2 \times N$ matrix. Considering again $L = 2$:

$$\begin{array}{lcccccccccccccccc}
n & & 0 & 1 & 2 & 3 & 4 & 5 & 6 & 7 & 8 & 9 & 10 & 11 & 12 & 13 & 14 & 15 \\
\underline{\underline{\tilde{d}}}_0 = \sqrt{2} & [& -1 & 0 & 0 & 1 & -1 & 0 & 0 & 1 & -1 & 0 & 0 & 1 & -1 & 0 & 0 & 1 \,] \\
\underline{\underline{\tilde{d}}}_1 = \sqrt{2} & [& -1 & -1 & -1 & -1 & 0 & 0 & 0 & 0 & 0 & 0 & 0 & 0 & 1 & 1 & 1 & 1 \,] \\
\underline{\underline{\tilde{m}}}_0 = \sqrt{2} & [& 0 & 1 & -1 & 0 & 0 & 1 & -1 & 0 & 0 & 1 & -1 & 0 & 0 & 1 & -1 & 0 \,] \\
\underline{\underline{\tilde{m}}}_1 = \sqrt{2} & [& 0 & 0 & 0 & 0 & 1 & 1 & 1 & 1 & -1 & -1 & -1 & -1 & 0 & 0 & 0 & 0 \,]
\end{array} \tag{3.18}$$

As presented in Table 2.1, the matrix elements of the transformed operator $\hat{A}'$ in the energy basis are identical to those of the original operator $\hat{A}$ in the Fock basis. Local operators that are diagonal in the Fock basis include the charge density, $\tilde{d}_i$, and magnetization, $\tilde{m}_i$. The corresponding LIOMs, which are diagonal in the energy basis, are the charge ($\hat{\mathbb{d}}_i$) and spin ($\hat{\mathbb{m}}_i$) LIOMs.

$$\begin{aligned}
\hat{\mathbb{d}}_i &= \hat{Q}_{opt} \tilde{d}_i \hat{Q}^\dagger_{opt} = \sum_n \langle n | \tilde{d}_i | n \rangle \, | E_{a(n)} \rangle \langle E_{a(n)} | \\
\hat{\mathbb{m}}_i &= \hat{Q}_{opt} \tilde{m}_i \hat{Q}^\dagger_{opt} = \sum_n \langle n | \tilde{m}_i | n \rangle \, | E_{a(n)} \rangle \langle E_{a(n)} |,
\end{aligned} \tag{3.19}$$

where $\{a(n)\}$ is the assignment array obtained through the Hungarian algorithm, as described in Section 3.

Complete set of operators

In Section 2, we described how to construct a complete set of operators under the Frobenius inner product. The complete set can be in either the Fock basis, denoted as $\{\hat{A}\}$, or the energy basis, denoted as $\{\hat{A}'\}$. The set $\{\hat{A}\}$ consists of the orthonormalized local charge density and magnetization operators, and their products, which are diagonal in the Fock basis. The set $\{\hat{A}'\}$ consists of the LIOMs and their products, which are diagonal in the energy basis.

Below, we describe how we calculate and store the matrix representation of these operators.

To construct the complete set of operators diagonal in the Fock basis, $\{\hat{A}\}$, for an L-site system, we start with the following single-site operators:

- orthonormalized local charge density $\tilde{d}_i^{(1)}$
- orthonormalized local magnetization $\tilde{m}_i^{(1)}$
- orthonormalized second-order on-site operator $\tilde{o}_i^{(1)}$
- identity operator $\hat{I}_i^{(1)}$

The outer product of any combination of these four single-site operators across L sites forms an operator in the set, $\{\hat{A}\}$. The single-site operators are ordered from right to left in the product. The number of non-identity single-site operators determines the order of the operator, with each second-order on-site operator increasing the order by one. The total number of the operators in the set, $\{\hat{A}\}$, is $N = 4^L$.

For example, for $L = 2$,

- zeroth order

$$\hat{I} = I_1^{(1)} \otimes I_0^{(1)}$$

- first order

$$\tilde{d}_0 = I_1^{(1)} \otimes \tilde{d}_0^{(1)}$$

$$\tilde{d}_1 = \tilde{d}_1^{(1)} \otimes I_0^{(1)}$$

$$\tilde{m}_0 = I_1^{(1)} \otimes \tilde{m}_0^{(1)}$$

$$\tilde{m}_1 = \tilde{m}_1^{(1)} \otimes I_0^{(1)}$$

- second order

$$\tilde{d}_1\tilde{d}_0 = \tilde{d}_1^{(1)} \otimes \tilde{d}_0^{(1)}$$

$$\tilde{m}_1\tilde{m}_0 = \tilde{m}_1^{(1)} \otimes \tilde{m}_0^{(1)}$$

$$\tilde{d}_1\tilde{m}_0 = \tilde{d}_1^{(1)} \otimes \tilde{m}_0^{(1)}$$

$$\tilde{m}_1\tilde{d}_0 = \tilde{m}_1^{(1)} \otimes \tilde{d}_0^{(1)}$$

$$\tilde{o}_0 = I_1^{(1)} \otimes \tilde{o}_0^{(1)}$$

$$\tilde{o}_1 = \tilde{o}_1^{(1)} \otimes I_0^{(1)}$$

- third order

$$\tilde{o}_1\tilde{d}_0 = \tilde{o}_1^{(1)} \otimes \tilde{d}_0^{(1)}$$

$$\tilde{d}_1\tilde{o}_0 = \tilde{d}_1^{(1)} \otimes \tilde{o}_0^{(1)}$$

$$\tilde{o}_1\tilde{m}_0 = \tilde{o}_1^{(1)} \otimes \tilde{m}_0^{(1)}$$

$$\tilde{m}_1\tilde{o}_0 = \tilde{m}_1^{(1)} \otimes \tilde{o}_0^{(1)}$$

- fourth order

$$\tilde{o}_1\tilde{o}_0 = \tilde{o}_1^{(1)} \otimes \tilde{o}_0^{(1)}$$

We can transform the operators of the $\{\hat{A}\}$ from the energy basis to the Fock basis, using $\hat{Q}_{opt}$. The set of transformed operators forms the complete set diagonal in the energy basis, $\{|O'\rangle\}$:

$$\hat{A}' = \hat{Q}_{opt}\hat{A}\hat{Q}_{opt}^{\dagger} = \sum_n \langle n|\, \hat{A}\, |n\rangle \left|E_{a(n)}\right\rangle\left\langle E_{a(n)}\right| \tag{3.20}$$

where $\{a(n)\}$ is the assignment array.

We construct the matrix representation of the complete set of operators, $\{\hat{A}\}$, in the Fock basis, because it requires fewer calculations.

The matrix representation of the single-site operators in the Fock basis for a given site i are:

$$\underline{\underline{\tilde{d}}}_i^{(1)} = \begin{pmatrix} -\sqrt{2} & 0 & 0 & 0 \\ 0 & 0 & 0 & 0 \\ 0 & 0 & 0 & 0 \\ 0 & 0 & 0 & \sqrt{2} \end{pmatrix} \qquad \underline{\underline{\tilde{m}}}_i^{(1)} = \begin{pmatrix} 0 & 0 & 0 & 0 \\ 0 & \sqrt{2} & 0 & 0 \\ 0 & 0 & -\sqrt{2} & 0 \\ 0 & 0 & 0 & 0 \end{pmatrix}$$

$$\underline{\underline{\tilde{o}}}_i^{(1)} = \begin{pmatrix} 1 & 0 & 0 & 0 \\ 0 & -1 & 0 & 0 \\ 0 & 0 & -1 & 0 \\ 0 & 0 & 0 & 1 \end{pmatrix} \qquad \underline{\underline{\hat{I}}}_i^{(1)} = \begin{pmatrix} 1 & 0 & 0 & 0 \\ 0 & 1 & 0 & 0 \\ 0 & 0 & 1 & 0 \\ 0 & 0 & 0 & 1 \end{pmatrix} \tag{3.21}$$

The matrix representations of the operators in $\{\hat{A}\}$ are constructed by performing the outer product of different combinations of the matrices in Eq.(3.21).

For a 2-site system, Eq.(3.22) shows the diagonal elements of $\{\underline{\underline{A}}_F\}$, as vectors.

n	0	1	2	3	4	5	6	7	8	9	10	11	12	13	14	15
$\underline{\underline{I}} =$	[1	1	1	1	1	1	1	1	1	1	1	1	1	1	1	1]
$\underline{\underline{\tilde{d}}}_0 = \sqrt{2}$	[−1	0	0	1	−1	0	0	1	−1	0	0	1	−1	0	0	1]
$\underline{\underline{\tilde{d}}}_1 = \sqrt{2}$	[−1	−1	−1	−1	0	0	0	0	0	0	0	0	1	1	1	1]
$\underline{\underline{\tilde{m}}}_0 = \sqrt{2}$	[0	1	−1	0	0	1	−1	0	0	1	−1	0	0	1	−1	0]
$\underline{\underline{\tilde{m}}}_1 = \sqrt{2}$	[0	0	0	0	1	1	1	1	−1	−1	−1	−1	0	0	0	0]
$\underline{\underline{\tilde{d}}}_0\underline{\underline{\tilde{d}}}_1 =$	[2	0	0	−2	0	0	0	0	0	0	0	0	−2	0	0	2]
$\underline{\underline{\tilde{d}}}_0\underline{\underline{\tilde{m}}}_1 =$	[0	0	0	0	−2	0	0	2	2	0	0	−2	0	0	0	0]
$\underline{\underline{\tilde{d}}}_1\underline{\underline{\tilde{m}}}_0 =$	[0	−2	2	0	0	0	0	0	0	0	0	0	0	2	−2	0]
$\underline{\underline{\tilde{m}}}_0\underline{\underline{\tilde{m}}}_1 =$	[0	0	0	0	0	2	−2	0	0	−2	2	0	0	0	0	0]
$\underline{\underline{\tilde{o}}}_0 =$	[1	−1	−1	1	1	−1	−1	1	1	−1	−1	1	1	−1	−1	1]
$\underline{\underline{\tilde{o}}}_1 =$	[1	1	1	1	−1	−1	−1	−1	−1	−1	−1	−1	1	1	1	1]
$\underline{\underline{\tilde{o}}}_0\underline{\underline{\tilde{d}}}_1 = \sqrt{2}$	[−1	1	1	−1	0	0	0	0	0	0	0	0	1	−1	−1	1]
$\underline{\underline{\tilde{o}}}_1\underline{\underline{\tilde{d}}}_0 = \sqrt{2}$	[−1	0	0	1	1	0	0	−1	1	0	0	−1	−1	0	0	1]
$\underline{\underline{\tilde{o}}}_0\underline{\underline{\tilde{m}}}_1 = \sqrt{2}$	[0	0	0	0	1	−1	−1	1	−1	1	1	−1	0	0	0	0]
$\underline{\underline{\tilde{o}}}_1\underline{\underline{\tilde{m}}}_0 = \sqrt{2}$	[0	1	−1	0	0	−1	1	0	0	−1	1	0	0	1	−1	0]
$\underline{\underline{\tilde{o}}}_0\underline{\underline{\tilde{o}}}_1 =$	[1	−1	−1	1	−1	1	1	−1	−1	1	1	−1	1	−1	−1	1]

(3.22)

In our code, the *lbt* function computes the matrix representation of each operator by performing the outer product and storing the diagonal elements as vectors. The vectors are stored in rows of a two-dimensional array named *matiom*.

L-bit Hamiltonian

Here, we describe how we calculate the coefficients in the l-bit Hamiltonian using the complete set of operators $\{\hat{A}\}$, which are diagonal in the Fock basis.

To achieve this, we transform Eq.(2.39) from the Fock basis to the energy basis, using the unitary operator U_{opt} (dropping the subscript for brevity).

$$\begin{aligned}\hat{U}\hat{H}\hat{U}^{\dagger} =& J_0\hat{U}\hat{I}\hat{U}^{\dagger} + \sum_i J_i^c \hat{U}\mathbb{d}_i\hat{U}^{\dagger} + \sum_i J_i^s \hat{U}\mathbb{m}_i\hat{U}^{\dagger} + \sum_i J_{ii}^o \hat{U}\mathbb{o}_i\hat{U}^{\dagger} \\ &+ \sum_{i,j(i>j)} J_{ij}^{cc}\hat{U}\mathbb{d}_i\mathbb{d}_j\hat{U}^{\dagger} + \sum_{i,j(i\neq j)} J_{ij}^{cs}\hat{U}\mathbb{d}_i\mathbb{m}_j\hat{U}^{\dagger} + \sum_{i,j(i>j)} J_{ij}^{ss}\hat{U}\mathbb{m}_i\mathbb{m}_j\hat{U}^{\dagger} \\ &+ \sum_{i,j,k(i>j>k)} J_{ijk}^{ccc}\hat{U}\mathbb{d}_i\mathbb{d}_j\mathbb{d}_k\hat{U}^{\dagger} + \sum_{i,j,k(i>j,i\neq k,j\neq k)} J_{ijk}^{ccs}\hat{U}\mathbb{d}_i\mathbb{d}_j\mathbb{m}_k\hat{U}^{\dagger} \\ &+ \sum_{i,j,k(i\neq j,i\neq k,j>k)} J_{ijk}^{css}\hat{U}\mathbb{d}_i\mathbb{m}_j\mathbb{m}_k\hat{U}^{\dagger} + \sum_{i,j,k(i>j>k)} J_{ijk}^{sss}\hat{U}\mathbb{m}_i\mathbb{m}_j\mathbb{m}_k\hat{U}^{\dagger} \\ &+ \sum_{i,j(i\neq j)} J_{iij}^{oc}\hat{U}\mathbb{o}_i\mathbb{d}_j\hat{U}^{\dagger} + \sum_{i,j(i\neq j)} J_{iij}^{os}\hat{U}\mathbb{o}_i\mathbb{m}_j\hat{U}^{\dagger} + ... \end{aligned} \tag{3.23}$$

In Eq.(3.23), the transformation changes the operators of the complete set diagonal in the energy basis $\{\hat{A}'\}$ into the operators of the complete set diagonal in the Fock basis $\{\hat{A}\}$.

$$\hat{U}\hat{A}'\hat{U}^{\dagger} = \hat{U}\hat{Q}\hat{A}\hat{Q}^{\dagger}\hat{U}^{\dagger} = \hat{A}. \tag{3.24}$$

Therefore:

$$\begin{aligned}\hat{U}\hat{H}\hat{U}^{\dagger} =& J_0\hat{I} + \sum_i J_i^c \tilde{d}_i + \sum_i J_i^s \tilde{m}_i + \sum_i J_{ii}^o \tilde{o}_i + \sum_{i,j(i\neq j)} J_{ij}^{cs}\tilde{d}_i\tilde{m}_j + \sum_{i,j(i>j)} J_{ij}^{cc}\tilde{d}_i\tilde{d}_j + \sum_{i,j(i>j)} J_{ij}^{ss}\tilde{m}_i\tilde{m}_j \\ &+ \sum_{i,j,k(i>j>k)} J_{ijk}^{ccc}\tilde{d}_i\tilde{d}_j\tilde{d}_k + \sum_{i,j,k(i>j,k\neq i,k\neq j)} J_{ijk}^{ccs}\tilde{d}_i\tilde{d}_j\tilde{m}_k + \sum_{i,j,k(i>j\neq i,k\neq i,j>k)} J_{ijk}^{css}\tilde{d}_i\tilde{m}_j\tilde{m}_k \\ &+ \sum_{i,j,k(i>j>k)} J_{ijk}^{sss}\tilde{m}_i\tilde{m}_j\tilde{m}_k + \sum_{ij,(i\neq j)} J_{iij}^{oc}\tilde{o}_i\tilde{d}_j + \sum_{ij,(i\neq j)} J_{iij}^{os}\tilde{o}_i\tilde{m}_j + ... \end{aligned} \tag{3.25}$$

In Eq.(3.25), $\hat{U}\hat{H}\hat{U}^{\dagger}$ is an operator that is diagonal in the Fock basis:

$$\hat{U}\hat{H}\hat{U}^{\dagger} = E_{a(n)}\left|n\right\rangle\left\langle n\right| \tag{3.26}$$

where $\{a(n)\}$ the assignment array.

Coefficients in l-bit Hamiltonian

Here, we describe how we calculate the coefficients in the l-bit Hamiltonian, using the matrix representation of the operators of the complete set, $\{\hat{A}\}$ in the Fock basis and Eq.(3.25).

To calculate the coefficients in the l-bit Hamiltonian, we project the corresponding operator in Eq.(3.25) onto $\hat{H}' = \hat{U}_{opt}\hat{H}\hat{U}_{opt}^{\dagger}$. For example, the coefficients of the first-order charge terms, $\{J_i^c : i = 0, L-1\}$, are calculated as:

$$J_i^c = (\hat{U}_{opt}\hat{H}\hat{U}_{opt}^{\dagger}, \tilde{d}_i) = (\hat{H}, \mathbb{d}_i) = \frac{1}{N}\sum_{n=0}^{N-1} E_{a(n)} \langle n| \tilde{d}_i |n\rangle \tag{3.27}$$

fip is a member function of *iom* object, which calculates the coefficients in the l-bit Hamiltonian. The *fip* function takes as input two vectors: the eigenvalues of the Hamiltonian rearranged by the assignment array, and the diagonal elements of the corresponding matrix, $\underline{\underline{A}}_F$, stored in the rows of the *matiom* array. The computed set of coefficients for each disorder configuration is then stored in *cSample*.

Truncated l-bit Hamiltonians and their eigenvalues

To isolate the contribution of specific first and second-order terms in the l-bit Hamiltonian to the energy eigenvalues and, consequently, to the time dependence of EE, we truncate the l-bit Hamiltonian and retain only the relevant terms, as described in Section 2. The specific terms of interest in the l-bit Hamiltonian include: first-order charge and spin terms, second-order on-site terms, and the second-order charge-charge, charge-spin, and spin-spin terms.

Eq.(3.28) shows two examples of the truncated l-bit Hamiltonians which we will study in Chapter 4 and their corresponding eigenvalues: H_{liom1s}, which includes just the first-order spin terms, and $H_{liom2cc}$, which includes all first-order terms and second-order charge-charge terms.

$$
\begin{aligned}
H_{liom1s} =& J_0\hat{\mathbb{I}} + \sum_i J_i^s \hat{\mathbb{m}}_i \\
(E_{liom1s})_n =& J_0 + \sum_i J_i^s \langle n|\, \tilde{m}_i \,|n\rangle \\
H_{liom2cc} =& J_0\hat{\mathbb{I}} + \sum_i [J_i^c \hat{\mathbb{d}}_i + J_i^s \hat{\mathbb{m}}_i + \sum_i \sum_{j>i} J_{ij}^{cc} \hat{\mathbb{d}}_i \hat{\mathbb{d}}_j \\
(E_{liom2cc})_n =& J_0 + \sum_i [J_i^c \langle n|\, \tilde{d}_i \,|n\rangle + J_i^s \langle n|\, \tilde{m}_i \,|n\rangle] + \sum_i \sum_{j>i} J_{ij}^{cc} \langle n|\, \tilde{d}_i \tilde{d}_j \,|n\rangle
\end{aligned}
\tag{3.28}
$$

In our code, the eigenvalues of each truncated Hamiltonian are stored in separate arrays, each containing N real-valued elements with double precision. Once the entanglement entropies for all considered times are calculated, the eigenvalues are systematically removed from storage to optimize memory usage.

Test runs

In this section, we present an overview of the test runs conducted.

Orthonormality

We calculated the Frobenius inner products of all possible pairs of operators in our complete set, $\{\hat{A}\}$, for system sizes of $L = 2$, 4, and 6. The results for unmatched pairs were zero to 13 digits after the decimal point. The results for matched pairs were one to 14 digits after the decimal point.

2-site system

We compared the energy eigenvalues obtained from the complete l-bit Hamiltonian with those obtained from the exact diagonalization of the original Hamiltonian. The two sets of eigenvalues were consistent to 7 digits after the decimal point.

Limit of no hopping

We analytically calculated the disorder-average of coefficients in the l-bit Hamiltonian in the limit of no hopping ($t_h = 0.0$) and compared it with those computed through the code. The results were the same to 2 digits after the decimal point.

Averaging

In this section, we describe how we take averages. First, we review some statistics, then we describe the quantities over which we are averaging, and finally, we specify the averaging procedure for three different observables.

Statistical measures

Below, we briefly define population and sample datasets and explain how these statistical measures are used to characterize them.

Let X represent an observable, like EE, calculated from a quantity, like disorder configuration. If we calculate X for all possible values of this quantity, the resulting set of values forms a population: $\{X_1, X_2, X_3, ... X_P\}$, where P is the size of the population.

In most cases, it is impractical or impossible to calculate X for every possible

quantity value, as there may be infinitely many. Instead, we calculate X for a selected subset of values. This subset forms a sample: $\{X_1, X_2, X_3, \dots, X_N\}$, where N is the size of the sample.

The population is characterized by its first moment, the average (mean), and its second moment, the standard deviation (SD). The population average μ_X is calculated by:

$$\mu_X = \frac{\sum_{p=1}^{P} X_P}{P} \tag{3.29}$$

The standard deviation, denoted as σ_X, quantifies the extent to which values in the population deviate from the mean:

$$\sigma_X = \sqrt{\frac{\sum_{p=1}^{P}(X_p - \mu_X)^2}{P}}, \tag{3.30}$$

When we analyze a sample of N values of X, we can characterize it by calculating the sample mean $\bar{X}$ and the sample standard deviation SD_X, calculated as for μ_X and σ_X, but with P replaced by N. However, it is important to assess how accurately the sample statistics reflect the population statistics. The standard error of the mean denoted as SEM_X quantifies how closely the sample mean approximates the true population mean:

$$SEM_{\bar{X}} = \frac{SD_X}{\sqrt{N}}. \tag{3.31}$$

The 95% confidence interval (CI) provides the range within which the true population mean is expected to lie with 95% certainty:

$$CI_{\bar{X}} = [\bar{X} - 1.96 \times SEM_{\bar{X}}, \bar{X} + 1.96 \times SEM_{\bar{X}}]. \tag{3.32}$$

As N increases, X values closer to the true average μ_X occur more frequently, while the influence of extreme values on both the sample mean and sample standard deviation diminishes. This causes the sample standard deviation SD_X to stabilize, leading to a decrease in $SEM_{\bar{X}}$. Consequently, by increasing the sample size, we can reduce the standard error of the mean to the desired level of accuracy.

Quantities being averaged over

Here we describe the quantities over which we average and specify whether the data sets are populations or samples.

Disorder configurations

Below, we first define a disorder configuration and describe how they are generated.

To set up the Hamiltonian in Eq.(2.1), we randomly select the on-site potentials ϵ_i and the on-site magnetic fields h_i from uniform distributions within the intervals $[-W_{ch}, W_{ch}]$ and $[-W_{sp}, W_{sp}]$, respectively. This selection uses the Mersenne Twister pseudo-random number generator, which produces a specific sequence of numbers for a given seed. A disorder configuration consists of the set of selected values $\{\epsilon_i\}$ and $\{h_i\}$ for $i = 1, \ldots, L$. We store the seeds in a file named *SEEDS*, enabling us to regenerate the same disorder configurations.

Since we are running multiple configurations in parallel, we use a new seed for generating each disorder configuration. The seeds are derived from the epoch time in nanoseconds, which provides 16-digit large integers. These seeds are sufficiently distinct due to the timing of when the random number generator reads the epoch time, typically separated by 10^{12} nanoseconds. Using different

seeds in parallel computation is a standard practice. [48]

The datasets we calculate – including the ones for coefficients in the l-bit Hamiltonian, the timescales associated with each term, and the EE – are obtained from a limited number of disorder configurations N_{dc}. The potential number of disorder configurations is infinite, therefore each dataset is a sample.

Initial conditions

When calculating EE as a function of time, we need to set initial conditions. We use initial states with zero EE, specifically Fock states. These Fock states are categorized into blocks, each defined by a fixed number of particles and total spin. In this thesis, we focus on the half-filled block with zero net spin. For system sizes $L = 2$, 4, and 6, we average over all states in this block, amounting to 4, 36, and 400 states, respectively. These data sets are populations. For larger system sizes, including all possible states in the block becomes impractical, so we randomly select initial states from the block. These datasets are samples.

Coefficients within a type

The l-bit Hamiltonian consists of multiple terms, each associated with a coefficient. These terms are categorized by type, such as first-order charge terms. The coefficients within a type form a dataset that is a population, for example, the first-order charge coefficients $\{J_i^c : i = 0, L-1\}$. Averaging over the coefficients within each type simplifies handling multiple values and provides a single representative value that characterizes each type of coefficient.

Coefficients in l-bit Hamiltonian

We calculate the coefficients in the l-bit Hamiltonian as described in Section 3.

We store the coefficients obtained from each disorder configuration in a data array named *ccsample*. In this array, each row corresponds to one of the terms in the l-bit Hamiltonian (e.g., the third row contains the first-order charge coefficient of J_1^c, the fourth row contains the first-order charge coefficient of J_2^c and so on), and each column corresponds to a different disorder configuration.

In this work, we take the average over both disorder configurations and the coefficients within each type. Since our dataset includes both sample and population data, we calculate the standard deviation for an observable, such as the first-order charge terms, using the following expression:

$$SD_{[J_i^c]_s} = \sqrt{\frac{\sum_{p=1}^{P} \sum_{s=1}^{N} ([J_p^c]_s - \bar{J}^c)^2}{N \times P}} \tag{3.33}$$

where the first summation in the numerator accounts for the population of coefficients within a type, and the second summation corresponds to coefficients obtained from each disorder configuration.

The standard error of the mean (SEM) is then calculated as:

$$SEM_{\bar{J}^c} = \frac{SD_{[J_i^c]_s}}{\sqrt{N}}. \tag{3.34}$$

Notice that in the denominator, we only divide by the square root of the sample size.

Test runs on average coefficients

We ran tests to determine the number of disorder configurations needed for a reliable and accurate sample average of the coefficients. The test was performed for system sizes $L = 2$, 4, and 6, $W_{ch} = 16$, $W_{sp} = 0.1$, $U = 1$ and $n_{HA} = 7$. For systems sizes $L = 2$ and 4, up to 10^5 disorder configurations were considered.

For systems size $L = 6$, the number of disorder configurations was limited to 10^3.

We calculated the average over both the disorder configurations and the coefficients within each type. In addition to the average value, we calculated the corresponding standard deviation and the width of the 95% confidence interval, as a function of the number of disorder configurations.

As the sample size increased across all coefficient types and system sizes, we observed a decrease in the width of the confidence interval. The average coefficients fluctuated within this range, with the fluctuations diminishing as the confidence interval narrowed. Initially, the standard deviation increased, then stabilized at a steady value. This behavior indicated that the sample average of the coefficients was converging toward the true value.

Table 3.3 shows the average values and standard deviation of each type of coefficient for $L = 4$ for $N_{dc} = 10^3$ and 10^5.

Type	average ($N_{dc} = 10^3$)	average ($N_{dc} = 10^5$)	SD ($N_{dc} = 10^3$)	SD ($N_{dc} = 10^5$)
first-order charge	0.3 ± 0.4	0.35 ± 0.04	6.7	6.6
first-order spin	0.000 ± 0.004	0.0004 ± 0.0004	0.07	0.07
second-order charge-charge	−0.004 ± 0.0025	−0.0044 ± 0.0002	0.04	0.04
second-order charge-spin	0.000 ± 0.0007	0.0000 ± 0.00007	0.01	0.01
second-order spin-spin	0.000 ± 0.003	0.004 ± 0.0003	0.04	0.04
second-order on-site	0.26 ± 0.004	0.263 ± 0.0005	0.08	0.08

Table 3.3: The average values and standard deviation of the first and second-order terms of the l-bit Hamiltonian for $W_{ch} = 16$, $W_{sp} = 0.1$, $U = 1$, $n_{HA} = 7$, $L = 4$ and $N_{dc} = 10^5$. The confidence interval is reported as the uncertainty in average values.

In Table 3.3, as sample size increased from 10^3 to 10^5, the standard deviation remained almost the same. The average value also remained relatively stable, indicating that even with $N_{dc} = 1000$ the sample average is reliable. The width of the confidence interval decreased. In conclusion, averaging the coefficients over $N_{dc} = 1000$ disorder configurations, produced reliable average values that are accurate to one digit after the decimal point.

Timescales

The coefficient of each term in the l-bit Hamiltonian has units of energy. The inverse of the magnitude of each coefficient has units of time and determines the associated timescale. Below, we describe two methods for calculating the average timescale associated with each term in the l-bit Hamiltonian.

The first method involves averaging the timescales directly over disorder configurations. This average tends to be dominated by coefficients with small magnitude.

In the second method, we first calculate the average magnitude of the coefficients over disorder configurations and then take the inverse of this average. In this approach, the average value captures the effect of coefficients with a larger magnitude.

Small-magnitude coefficients have a small weight in the l-bit Hamiltonian and contribute less to the EE time dependence than those with large magnitudes. Our goal is to connect the terms in the l-bit Hamiltonian with the EE time dependence. Hence, we use the second averaging approach because it provides a representative timescale for the values, which have a greater impact on the EE time dependence.

For example, the average timescale associated with J_{12}^{ss} is:

$$|t_{12}^{ss}| = \frac{N_{dc}}{\sum_{i=1}^{i=N_{dc}} |ccSample_{ij'}|} \tag{3.35}$$

Entanglement entropy

Unlike the coefficients in the l-bit Hamiltonian, EE depends on both the disorder configuration and the system's initial state. We calculate the average EE in two

ways: first, by averaging over disorder configurations with a fixed initial state; and second, by averaging over both disorder configurations and initial states.

As described in Section 3, we store the EE values in a data array named *eeSample*. In this array, each column represents the EE at a specific time, while each row corresponds to the EE obtained from one disorder configuration and one initial state.

When averaging only over disorder configurations, the initial state remains fixed across all configurations. When averaging over both disorder configurations and initial states, in each iteration we calculate the EE for a different initial state and a different disorder configuration.

To obtain a sample EE average that accurately represents the full population of disorder configurations, it is important to increase the sample size until the uncertainty in the sample average becomes negligible. In Section 4, we will examine how many disorder configurations are necessary to compute a sample average that closely approximates the true population average.

Results

The broad aim of this thesis is to understand the time-dependent behavior of EE in a disordered Hubbard chain. More specifically, we explore how this behavior relates to the EE obtained from truncated l-bit Hamiltonians.

The primary question we address is: Does increasing the accuracy of the Hungarian algorithm reduce the observed offset between the EE of the exact Hamiltonian and the EE of the second-order truncated l-bit Hamiltonian? We hypothesize that higher accuracy in the Hungarian algorithm will lead to more localized LIOMs, allowing the second-order truncated Hamiltonian to better capture the time dependence of the EE from the exact Hamiltonian.

In Section 4.1, we investigate how increasing the accuracy level of the Hungarian algorithm affects the optimization of unitary matrices and the EE obtained from truncated l-bit Hamiltonians. In Section 4.2, we compare the EE from truncated l-bit Hamiltonians with the EE from the exact non-interacting and interacting Hamiltonians.

Assessing impact of Hungarian algorithm implementation

When implementing the Hungarian algorithm, one must choose the algorithm's accuracy level and how to make the matrix positive.

To determine the best choices, we first apply the Hungarian algorithm to randomly generated matrices. We investigate how increasing the accuracy of the algorithm and using different methods for making the unitary matrix positive affect the column order of the optimized matrices. Next, we examine how increasing the accuracy level of the Hungarian algorithm impacts the disorder-averaged EE of the truncated l-bit Hamiltonian.

Tests on random matrices

We address three questions, numbered below.

Question(1): Does increasing the accuracy level of the Hungarian algorithm affect the order of columns in the optimized version of a unitary matrix?

To address this we take the following approach. We generate three sets of square matrices: ten of size 500×500, five of size 1000×1000, and one of size 5000×5000, all filled with real numbers that are randomly generated from a uniform distribution in the range $[-1,1]$. We normalize the columns to simulate the eigenstates.

To make the matrices positive-valued for HA implementation, we take the absolute value of each element. The Hungarian algorithm is then implemented on each matrix with different accuracy levels: $n_{HA} = 1, 2, 3, ...\, 13$.

To compare assignments obtained at different accuracy levels, we use $n_{HA} = 13$, the highest accuracy level for reference. We define the assignment deviation, denoted as $D(n_{HA})$, as the number of elements in the assignment array a_i that differ from those in the assignment array using the reference accuracy level.

The results of this analysis are shown in the solid black lines in Figure 4.1. For all matrix sizes, implementing the Hungarian algorithm with $n_{HA} = 1$ results in the highest assignment deviation. As n_{HA} increases, the deviation $D(n_{HA})$ decreases. There is a threshold accuracy level, n'_{HA}, where $D(n_{HA} \geq n'_{HA})$ vanishes. The

standard deviation of the assignment deviation also vanishes at $n_{HA} = n'_{HA}$, indicating that $D_{n'_{HA}}$ is zero for all the sample matrices.

Thus, increasing the accuracy of the Hungarian algorithm does affect the column order in the optimized version of a unitary matrix.

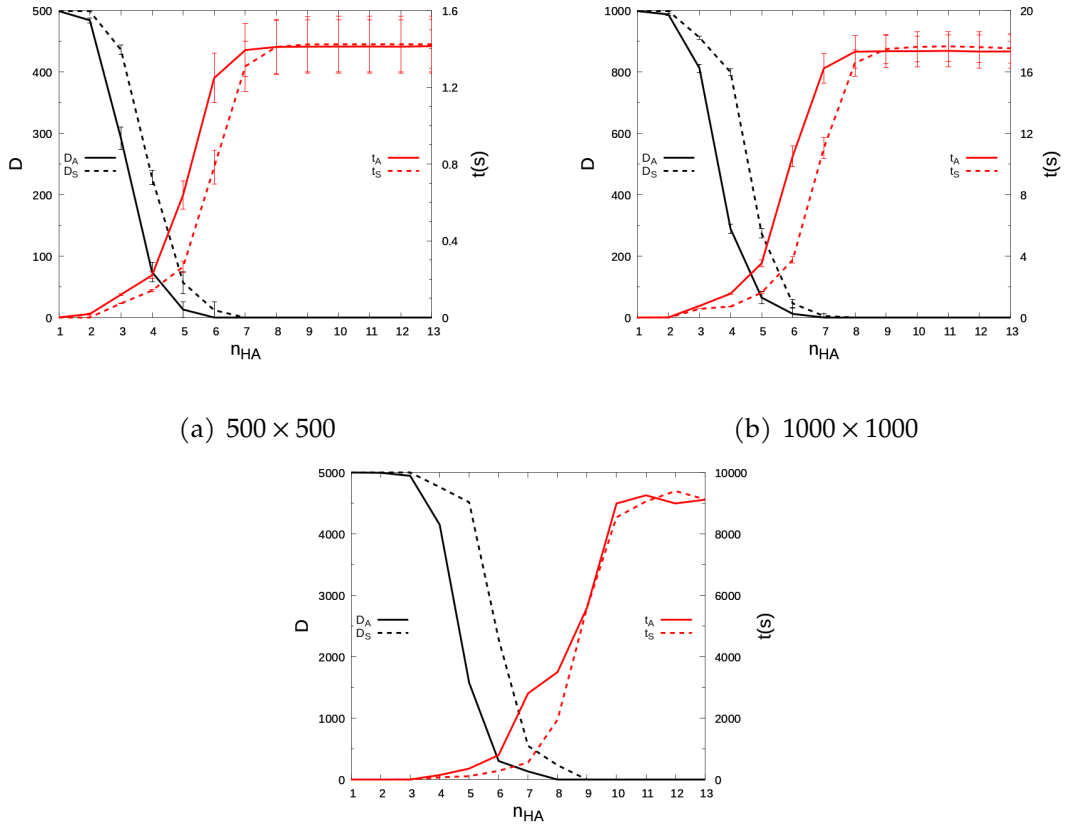

(a) 500×500 (b) 1000×1000

(c) 5000×5000

Figure 4.1: The assignment deviation $D_{A,S}$ and runtime $t_{A,S}$ of the absolute and square approaches versus the HA accuracy level n_{HA} for matrix sizes: (a)500×500, (b)1000×1000, and (c)5000×5000. The assignment deviations and runtimes are averaged over ten 500×500 in (a) and five 1000×1000 random matrices in (b), and the vertical bars show the corresponding standard deviation.

Question(2): What is the more efficient way to make the matrices positive in implementing the Hungarian algorithm: taking the absolute value or squaring the magnitude?

We use the same sample of random matrices, but instead of taking the absolute

value, we make the matrices positive by squaring the magnitude. We then compare the assignment deviation of the absolute approach $D_A(n_{HA})$ with the square one $D_S(n_{HA})$, as well as their corresponding runtimes, $t_A(n_{HA})$ and $t_S(n_{HA})$.

Figure 4.1 shows the assignment deviations $D_A(n_{HA})$ (black solid), $D_S(n_{HA})$ (black dashed) and corresponding runtimes $t_A(n_{HA})$ (red solid), and $t_S(n_{HA})$ (red dashed) for the random matrices. Additionally, Table 4.1 presents the threshold values of n'_{HA} at which the deviation vanishes, along with runtimes $t_A(n'_{HA})$ and $t_S(n'_{HA})$ for matrices of different sizes. We observe that the deviation for the squaring approach, D_S, vanishes at a higher n'_{HA} compared to the absolute approach, D_A. Additionally, for all matrix sizes, the runtime at the threshold accuracy level for the absolute value approach is shorter than that for the squaring approach, i.e., $t_A(n'HA) < t_S(n'HA)$. Therefore, the absolute approach is more efficient than the squaring approach.

This result can be explained by considering elements within a single column of these matrices: the magnitudes are all less than or equal to one. Squaring values less than one brings them closer together compared to taking the absolute value. The Hungarian algorithm performs better when these differences are larger, which is why the absolute value approach—by dispersing the values more widely—outperforms the squaring approach. Hereafter, we will use the absolute approach in implementing the Hungarian algorithm.

size	$(n'_{HA})_{absolute}$	$t_A(n'_{HA})[s]$	$SD_{t_A(n'_{HA})}[s]$	$(n'_{HA})_{square}$	$t_S(n'_{HA})[s]$	$SD_{t_S(n'_{HA})}[s]$
500	6	1.3	0.1	7	1.3	0.1
1000	7	16.2	1.0	8	16.6	0.9
5000	8	3500	—	9	5597	—

Table 4.1: The value n'_{HA}, the runtimes $t_{A,S}(n'_{HA})$, and the standard deviation of the runtimes $SD_{t_{A,S}(n'_{HA})}$ for the 500×500 and 1000×1000, and 5000×5000 random matrices using the absolute and square approaches.

Question(3): What is the minimum accuracy level required for an optimized assignment using the Hungarian algorithm?

As shown in the second column of Table 4.1, the minimum accuracy needed to find the optimal assignment increases with matrix size.

For the eigenstates of the disordered Hubbard model with a system size of L, we deal with matrix sizes of $4^L \times 4^L$. These matrices are sparse and block-structured, with the largest block being $\binom{L}{L/2}^2 \times \binom{L}{L/2}^2$. We study sizes $L = 2,4,6$, for which the largest blocks are 4×4, 36×36, 400×400, respectively.

In conclusion, increasing the accuracy of the Hungarian algorithm does change the order of the columns in the optimized unitary matrix. We are choosing to use $n_{HA} = 7$, as it produces the same results as larger values of n_{HA} for matrices up to 500×500.

Tests on entanglement entropy

Here, we test how the accuracy level of the Hungarian algorithm affects the EE obtained from the truncated l-bit Hamiltonian. However, we will be working with the disorder-averaged EE, so we begin by determining how many disorder configurations are needed.

Disorder average

The question we address here is: How many disorder configurations do we need to take for averaging?

We approach this in two ways. First, we examined the convergence of the average EE by sampling 10, 100, and 1000 disorder configurations, and calculated the standard deviation, denoted as SD, to assess the variability of the average values.

Figure 4.2 shows the average EE, denoted as $S(t)$, and standard deviations $SD(S(t))$

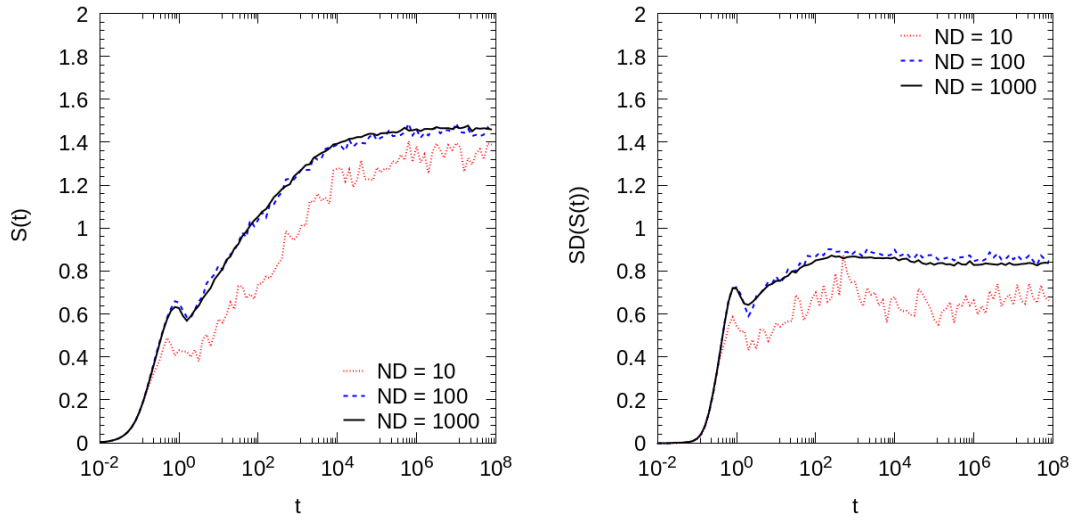

(a) S(t) (b) SD(S(t))

Figure 4.2: (a) The average $S(t)$ and (b) the standard deviation $SD(S(t))$ versus time for varying disorder configurations $N_{dc} = 10$, 100, and 1000, $L = 6$, $|\psi_0\rangle = |\uparrow\downarrow\uparrow\downarrow\uparrow\downarrow\rangle$, $W_{ch} = 16.0$, $W_{sp} = 0.1$, and $n_{HA} = 7$.

as a function of time for different numbers of disorder configurations, N_{dc}. In Figure 4.2(a), the average value of the EE becomes smoother as the number of disorder configurations increases. The significant difference between $N_{dc} = 10$ and $N_{dc} = 100$, and the proximity of the average values between $N_{dc} = 100$ and $N_{dc} = 1000$, demonstrate stabilization at $N_{dc} = 1000$. Figure 4.2(b) shows the large variability of EE results. The standard deviation increases from $N_{dc} = 10$ to $N_{dc} = 100$, and then decreases slightly as the sample size increases to $N_{dc} = 1000$. The standard deviation for $N_{dc} = 1000$ is lower than for $N_{dc} = 100$.

Next, we calculate the 95% confidence interval of the average EE using 1000 disorder configurations.

Figure 4.3 shows the average value, standard deviation, and confidence interval of the EE for non-interacting and interacting Hamiltonians with two disorder configurations: one with strong disorder in both charge and spin channels ($W_{sp} = W_{ch} = 16$) and one with strong disorder in the charge channel ($W_{ch} = 16$) but weak in spin ($W_{sp} = 0.1$). We refer to these cases as $W_{sp} = W_{ch}$

and $W_{sp} \ll W_{ch}$, respectively.

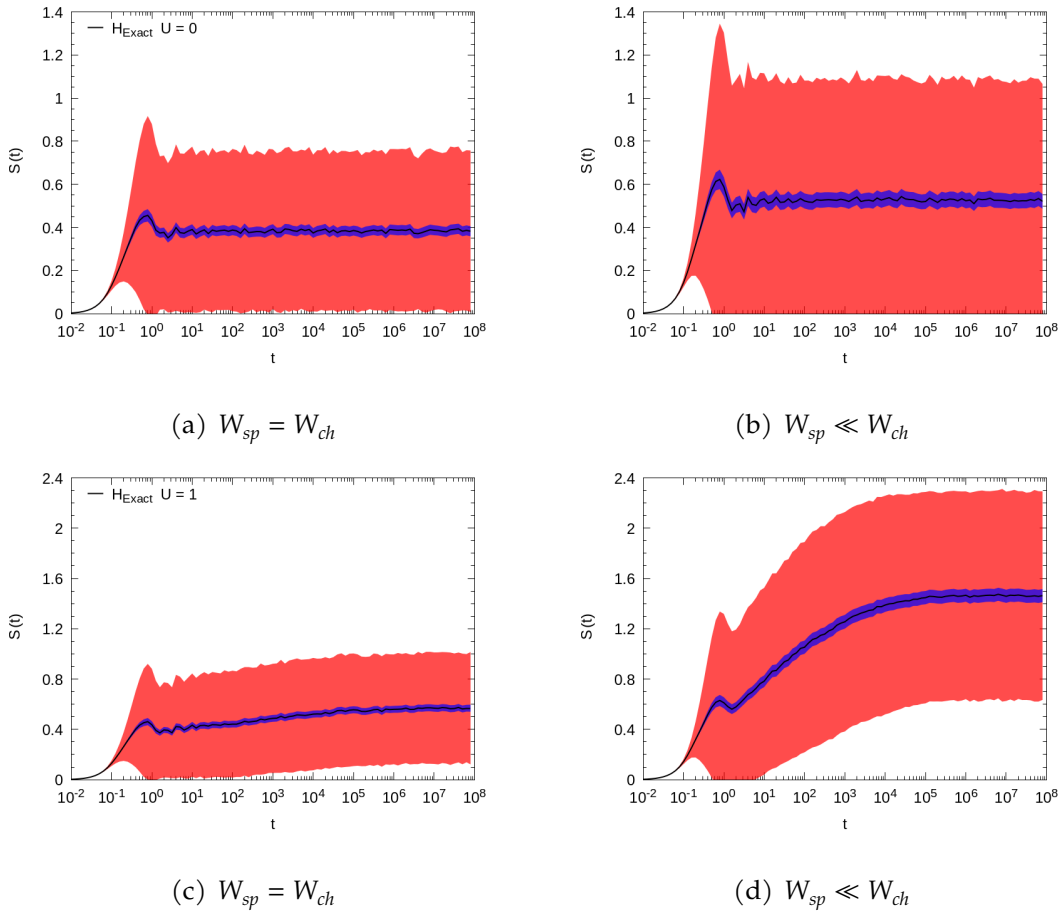

(a) $W_{sp} = W_{ch}$ (b) $W_{sp} \ll W_{ch}$

(c) $W_{sp} = W_{ch}$ (d) $W_{sp} \ll W_{ch}$

Figure 4.3: EE versus time for the exact Hamiltonian for (a,b) non-interacting and (c,d) interacting cases, averaged over 1000 disorder configurations for $L = 6$, $|\psi_0\rangle = |\uparrow\downarrow\uparrow\downarrow\uparrow\downarrow\rangle$, $W_{ch} = 16$, and (a,c) $W_{sp} = 16$ and (b,d) $W_{sp} = 0.1$. The blue region surrounding the black curve shows the 95% confidence interval, and the red region shows the standard deviation.

In Figure 4.3, the blue regions show the range where the true average value is expected to lie with 95% certainty. The blue region widens the most at long times in the interacting case when $W_{sp} \ll W_{sp}$, shown in Figure 4.3(d), indicating the greatest uncertainty in the EE. Even in this case, the average EE is estimated to be 1.46 ± 0.05. Therefore, with $N_{dc} = 1000$, the average is smooth, and the SEM is of order the second decimal place of the average.

Entanglement entropy of the truncated l-bit Hamiltonian

The question we aim to answer is: How does the accuracy level of the Hungarian algorithm affect the EE of the truncated Hamiltonians, and at what accuracy level does the EE converge for different disorder strengths in the charge and spin channels?

To address this question, we calculated the EE as a function of time for the first-order truncated l-bit Hamiltonian, denoted as H_{liom1}, both with and without interactions ($U = 1$ and $U = 0$), as well as for the second-order truncated l-bit Hamiltonian with interactions, denoted as H_{liom2}. These calculations were performed for a system size of $L = 6$, starting from the up-down state $|\psi_0\rangle = |\uparrow\downarrow\uparrow\downarrow\uparrow\downarrow\rangle$.

In our analysis, the truncated l-bit Hamiltonians were constructed using different accuracy levels of the Hungarian algorithm: $n_{HA} = 0$, 1, 4, and 7. Here, $n_{HA} = 0$ corresponds to a random assignment of eigenstates to Fock states. The EE obtained from the exact Hamiltonian, denoted as H_{exact}, with and without interactions, is presented for comparison. To explore the impact of disorder, we examined the two sets of disorder configurations described above, denoted as $W_{sp} = W_{ch}$ and $W_{sp} \ll W_{ch}$.

Our results are shown in Figures 4.4 (H_{liom1}, $U = 0$), 4.5 (H_{liom1}, $U = 1$), and 4.6 (H_{liom2}, $U = 1$).

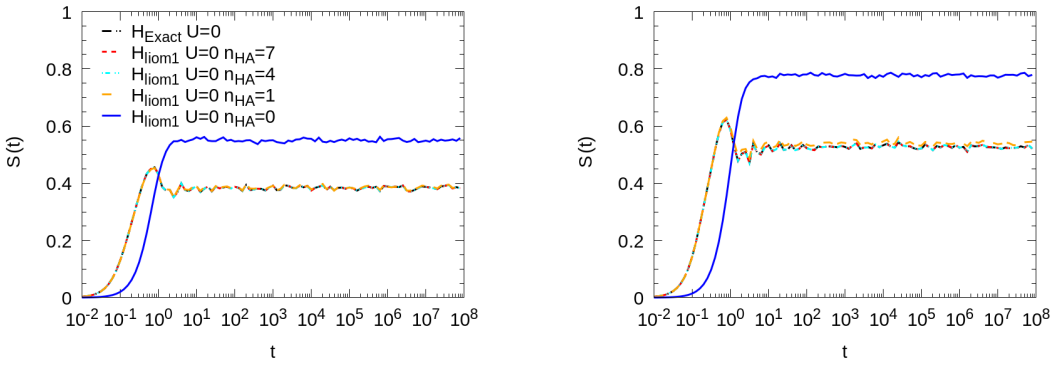

(a) $W_{sp} = W_{ch}$ (b) $W_{sp} \ll W_{ch}$

Figure 4.4: The EE versus time for the first-order truncated l-bit Hamiltonians (H_{liom1}) with $U = 0$ and different accuracy levels: $n_{HA} = 0$ (blue solid), 1 (orange dashed), 4 (cyan dashed), and 7 (red dashed). The EE of the exact Hamiltonian (H_{exact}) with $U = 0$ is shown for comparison. Data is averaged over 1000 disorder configurations for $L = 6$, $|\psi_0\rangle = |\uparrow\downarrow\uparrow\downarrow\uparrow\downarrow\rangle$, $W_{ch} = 16$, and (a) $W_{sp} = 16$, (b) $W_{sp} = 0.1$.

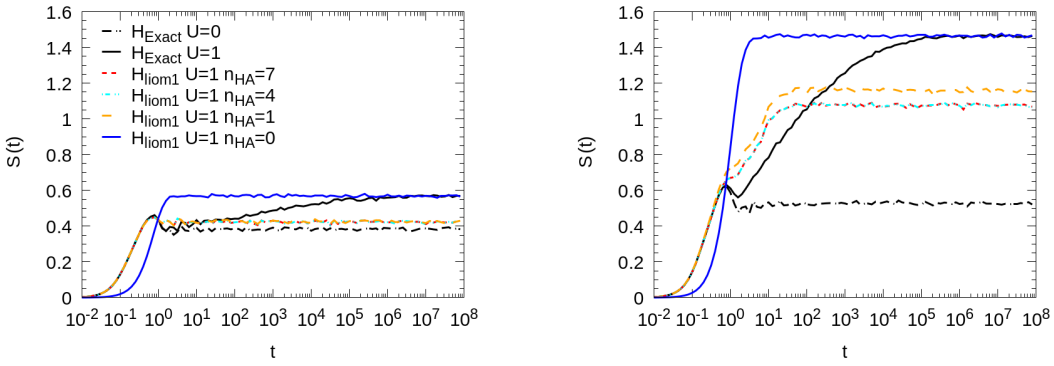

(a) $W_{sp} = W_{ch}$ (b) $W_{sp} \ll W_{ch}$

Figure 4.5: The EE versus time for the first-order truncated l-bit Hamiltonians (H_{liom1}) with $U = 1$ and different accuracy levels: $n_{HA} = 0$ (blue solid), 1 (orange dashed), 4 (cyan dashed), and 7 (red dashed). The EE of the exact Hamiltonian (H_{exact}) with $U = 0$ and $U = 1$ are shown for comparison. Data is averaged over 1000 disorder configurations for $L = 6$, $|\psi_0\rangle = |\uparrow\downarrow\uparrow\downarrow\uparrow\downarrow\rangle$, $W_{ch} = 16$, and (a) $W_{sp} = 16$, (b) $W_{sp} = 0.1$.

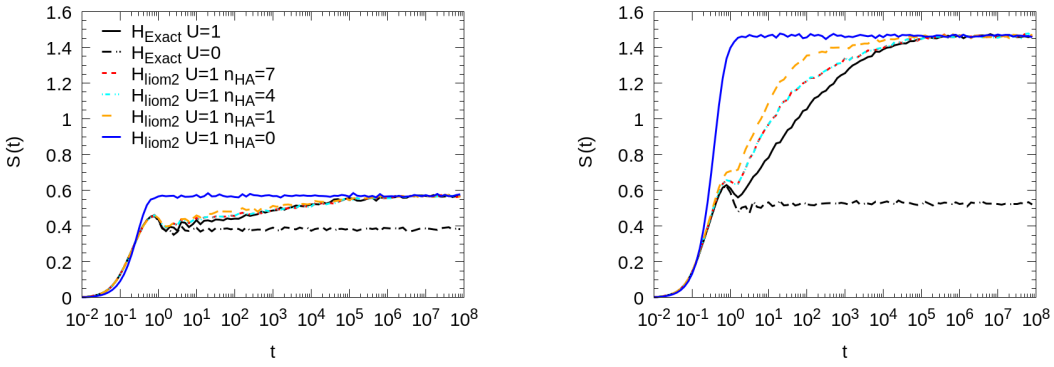

(a) $W_{sp} = W_{ch}$ (b) $W_{sp} \ll W_{ch}$

Figure 4.6: The EE versus time for the second-order truncated l-bit Hamiltonians (H_{liom2}) with $U = 1$ and different accuracy levels: $n_{HA} = 0$ (blue solid), 1 (orange dashed), 4 (cyan dashed), and 7 (red dashed). The EE of the exact Hamiltonian (H_{exact}) with $U = 0$ and $U = 1$ are shown for comparison. Data is averaged over 1000 disorder configurations for $L = 6$, $|\psi_0\rangle = |\uparrow\downarrow\uparrow\downarrow\uparrow\downarrow\rangle$, $W_{ch} = 16$, and (a) $W_{sp} = 16$, (b) $W_{sp} = 0.1$.

For $W_{sp} = W_{ch}$, the EE results obtained from H_{liom1} without interaction (Figure 4.4(a)) show a clear pattern. The EE obtained for $n_{HA} = 1$ (orange dashed), 4 (cyan dashed), and 7 (red dashed) are the same, while the EE for $n_{HA} = 0$ (blue solid) differs. The same is true in Figure 4.5(a) for the EE obtained from H_{liom1} with interactions. In Figure 4.6(a), the EE obtained from H_{liom2} for $n_{HA} = 4$ and 7 are the same, while the EE for $n_{HA} = 1$ and 0 differ. For H_{liom1} with and without interactions the EE converges at $n_{HA} = 1$, for H_{liom2} the EE converges at $n_{HA} = 4$.

For $W_{sp} \ll W_{ch}$, the EE results obtained from H_{liom1} without interaction (Figure 4.4(b)) show a different pattern. The EE for $n_{HA} = 4$ and 7 are the same, while the EE for $n_{HA} = 1$ and 0 differ. The EE obtained from H_{liom1} with interactions, as shown in Figure 4.5(b) follows the same pattern. As shown in Figure 4.6(b), the EE obtained from H_{liom2} also follows this trend. In all cases – whether for H_{liom1} without interactions, with interactions, or H_{liom2} – the EE converges at $n_{HA} = 4$.

There are other observations in the results shown in Figures 4.4, 4.5, and 4.6, which we will address in the next section. Here, we focus exclusively on the n_{HA} dependence.

To understand why convergence is faster when W_{sp} is larger, we computed the FIPR, as defined in Section 3. For $W_{sp} = W_{ch}$, the FIPR values are 0.706 (interacting) and 0.704 (non-interacting), while for $W_{sp} \ll W_{ch}$, they are 0.64 and 0.59, respectively. The FIPR values of the energy eigenstates are higher when $W_{sp} = W_{ch}$ compared to when $W_{sp} \ll W_{ch}$, indicating that the Hungarian algorithm requires more digits after the decimal point to optimize the unitary matrix and achieve convergence in the EE for systems with different disorder strengths.

In summary, increasing the accuracy of the Hungarian algorithm affects the EE of the truncated Hamiltonians. When $W_{sp} = W_{ch}$, $n_{HA} = 1$ is sufficient to achieve convergence of the EE. For $W_{sp} \ll W_{ch}$, $n_{HA} = 4$ is needed for EE convergence. Therefore, we will use $n_{HA} = 7$ hereafter.

Contribution of the charge and spin local integrals of motion in the time dependence of entanglement entropy

Here, we compare the EE from the truncated l-bit Hamiltonians with that from the exact Hamiltonian. Throughout this section, we consider again the two sets of disorder configurations: $W_{sp} = W_{ch}$, and $W_{sp} \ll W_{ch}$. We average the EE over disorder configurations and initial states of the half-filled block with zero net spin, using four different disorder configurations per initial state. The same sample of configurations and combinations is used for calculating the l-bit Hamiltonian coefficients and the EE of the exact and truncated Hamiltonians. In addition, we examine the timescales associated with the l-bit Hamiltonian coefficients. Timescales are averaged only over disorder configurations.

We begin by analyzing the EE time dependence of the exact non-interacting and interacting Hamiltonians. We then compare the EE from the first-order truncated l-bit Hamiltonian to the exact non-interacting Hamiltonian, followed by a

comparison of the second-order truncated Hamiltonian with the exact interacting Hamiltonian.

Exact Hamiltonian

Figures 4.7(a) and (b) show the EE obtained from the exact non-interacting and interacting Hamiltonians for $W_{sp} = W_{ch}$ and $W_{sp} \ll W_{ch}$, respectively.

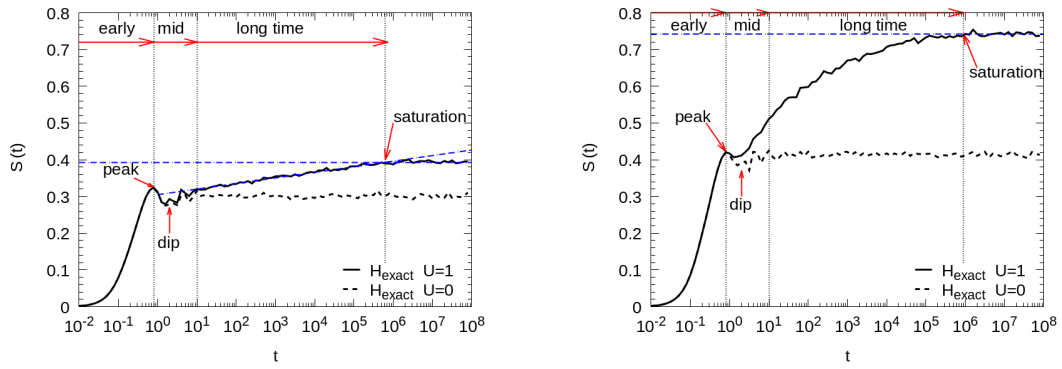

(a) $W_{sp} = 16$ (b) $W_{sp} = 0.1$

Figure 4.7: EE versus time for the exact non-interacting (H_{exact} with $U = 0$) and interacting (H_{exact} with $U = 1$) Hamiltonians with $L = 6$, $n_{HA} = 7$, and $W_{ch} = 16$, for (a) $W_{sp} = 16$ and (b) $W_{sp} = 0.1$, averaged over 1600 disorder configurations and initial states in the zero-spin, half-filled block.

From the EE time dependence obtained from the exact Hamiltonian with interactions (black solid line, Figure 4.7(a) and (b)), we define four distinct time regions: early times, mid times, long times, and saturation times. The division between early times and mid times is the peak point. The division between long times and saturation times is set where the curve reaches its saturation value. The division between mid times and long times in Figure 4.7(a) is the point where the $log(t)$ behavior starts, while in Figure 4.7(b), it is a qualitative line placed at the same location.

For both $W_{sp} = W_{ch}$ (Figure 4.7(a)) and $W_{sp} \ll W_{ch}$ (Figure 4.7(b)), the EE obtained from both non-interacting H_{exact} (dashed black) and interacting H_{exact}

(solid black) rises rapidly at early times. To understand this rapid rise, let's first focus on the non-interacting Hamiltonian. The single-particle energy eigenstates are Anderson localized, and the many-body wavefunction is a product of single-particle wavefunctions. Consider a single particle located in the right subsystem. As its wavefunction evolves, the probability density spreads across overlapping Anderson localized eigenstates, as discussed in Section 1. This spreading may cause the probability density to extend from the right subsystem into the left subsystem. If the probability density crosses the boundary between subsystems, the reduced density matrix ρ_L becomes more mixed, leading to a rapid rise in the EE. For the interacting Hamiltonian in the small U limit, the energy eigenstates retain localized features. The probability density spreads across subsystems in a similar manner, resulting in a similar rapid rise in EE at early times for the interacting case.

For both $W_{sp} = W_{ch}$ and $W_{sp} \ll W_{ch}$, the EE of the non-interacting H_{exact} saturates at long times. In the non-interacting case, as the single-particle wavefunction evolves, the probability density for the particles reaches a steady value across the sites at long times. At this point, the degree of mixing in the reduced density matrix ρ_L no longer changes, and as a result, the EE reaches a steady value and saturates.

For both $W_{sp} = W_{ch}$ and $W_{sp} \ll W_{ch}$, the EE in the interacting H_{exact} exhibits further growth at long times. When $W_{sp} = W_{ch}$, this growth is proportional to $log(t)$ over five orders of magnitude in time. This is the same behaviour seen in systems with a single degree of freedom, as discussed in Section 2. However, for $W_{sp} \ll W_{ch}$, the long-time behavior differs, showing no $log(t)$ dependence. The multiple degrees of freedom contribute differently to the long-time EE of the interacting H_{exact} when $W_{sp} \ll W_{ch}$. To explore this further, we will examine the contribution of LIOMs and their couplings to the EE time dependence in the next section.

First-order truncated Hamiltonian

Here, we compare the EE obtained from the first-order truncated Hamiltonian, H_{liom1}, with that of the exact non-interacting Hamiltonian, H_{exact}. We begin by comparing the results obtained from H_{liom1} without interactions and H_{exact} of the non-interacting system. Figures 4.8 shows the EE when (a) $W_{sp} = W_{ch}$ and (b) $W_{sp} \ll W_{ch}$, respectively. The EE obtained from H_{liom1} (cyan dashed) matches that obtained from H_{exact} (black dashed). In the non-interacting system, the truncation of the l-bit Hamiltonian to the first-order accurately captures the EE time dependence. The LIOMs act as projectors of the Anderson localized states.

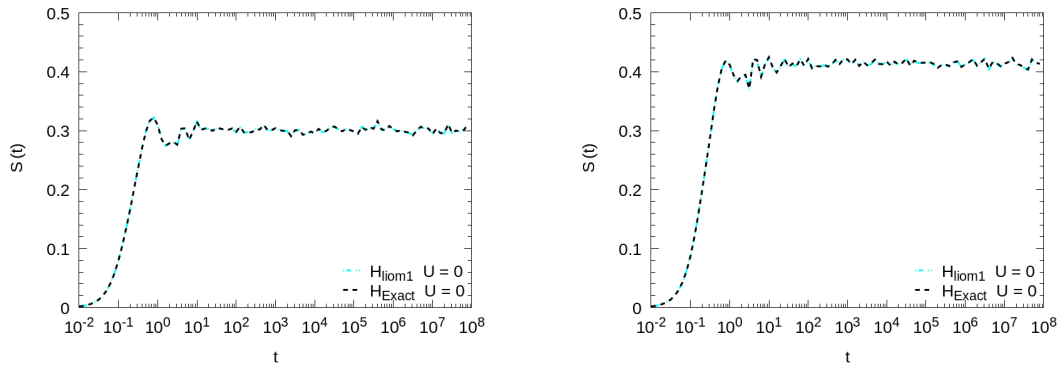

(a) $W_{sp} = W_{ch}$ (b) $W_{sp} \ll W_{ch}$

Figure 4.8: EE versus time for H_{exact} (black dashed) and H_{liom1} (cyan dashed) with $U = 0$, $L = 6$, $n_{HA} = 7$, $W_{ch} = 16$, and (a) $W_{sp} = 16$ and (b) $W_{sp} = 0.1$ averaged over 1600 disorder configurations and initial states.

Next, we compare the EE obtained from H_{liom1} with interactions with the EE obtained from H_{exact} without interactions, as shown in Figure 4.9. At early times, the EE obtained from H_{liom1} (dark-purple solid) matches that from the non-interacting H_{exact} (black dashed) for both $W_{sp} = W_{ch}$ and $W_{sp} \ll W_{ch}$. The EE of H_{liom1}, whether with or without interactions, shows a rapid rise at early times, similar to the H_{exact} result.

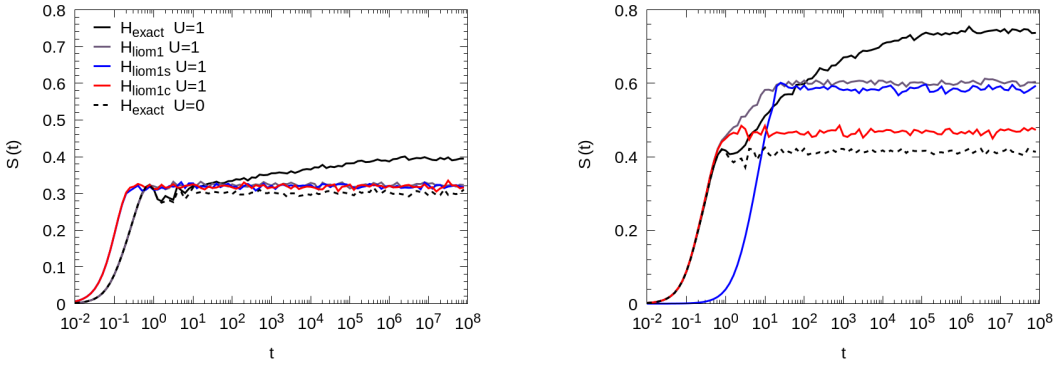

(a) $W_{sp} = W_{ch}$ (b) $W_{sp} \ll W_{ch}$

Figure 4.9: EE versus time for H_{exact} (black dashed), $H_{liom1all}$ (dark-purple) , H_{liom1c} (red solid) and H_{liom1s} (blue solid) with $L = 6$, $n_{HA} = 7$, $W_{ch} = 16$, and (a) $W_{sp} = 16$ and (b) $W_{sp} = 0.1$ averaged over 1600 disorder configurations and initial states.

At long times, the EE obtained from H_{liom1} reaches a fixed value for both $W_{sp} = W_{ch}$ and $W_{sp} \ll W_{ch}$, though the magnitudes differ. The fixed EE value from H_{liom1} is slightly higher than that from H_{exact} when $W_{sp} = W_{ch}$ and significantly higher when $W_{sp} \ll W_{ch}$. In the small U limit, the effect of interactions is to couple the Anderson localized states. The LIOMs then act as projectors of these objects. The localization lengths of the LIOMs with interactions are therefore larger than those without interaction. As the wavefunction spreads over the extended localization length of the interacting LIOMs, more distant parts of the system become entangled, resulting in the EE of H_{liom1} reaching for $W_{sp} = W_{ch}$ a slightly higher value than that of H_{exact}. When $W_{sp} \ll W_{ch}$, there is a significant difference between H_{liom1} result and the H_{exact} result.

At mid times, the results from H_{liom1} with $U = 1$ and H_{exact} with $U = 0$ are distinctly different. When $W_{sp} = W_{ch}$, the H_{liom1} result does not show a dip structure. When $W_{sp} \ll W_{ch}$, the H_{liom1} result has a significant further rise. The lack of dip at mid times in the H_{liom1} result for $W_{sp} = W_{ch}$ suggests that higher-order terms in the l-bit Hamiltonian of the interacting case contribute to the dip structure. The extra rise at mid times in the H_{liom1} result for $W_{sp} \ll W_{ch}$ can be

understood by examining the results for H_{liom1c} and H_{liom1s}, and the timescales associated with the first-order charge (J_{1c}) and spin (J_{1s}) terms in the l-bit Hamiltonian.

When $W_{sp} \ll W_{ch}$, the EE from H_{liom1c} (red solid) rises rapidly at early times and reaches a fixed value at mid times, while the EE from H_{liom1s} (blue solid) begins to rise at mid times and reaches a fixed value at long times. The fixed value in the H_{liom1s} result is significantly higher than that in the H_{liom1c} result. Strong disorder in the charge channel and weak disorder in the spin channel result in spin LIOMs with larger localization lengths than charge LIOMs. As the wavefunction spreads through spin LIOMs, more distant parts of the system get entangled than when it spreads through charge LIOMs. Therefore, the EE of H_{liom1s} rises to a much higher value compared to the EE of H_{liom1c}.

This distinct time that charge and spin LIOMs contribute to the EE is also connected to the timescales shown in Figure 4.10, associated with the coefficients in the l-bit Hamiltonian, including terms up to the second order. The red and blue points in Figures 4.10 represent the timescales of the first-order charge (J_{1c}) and spin (J_{1s}) terms, respectively. When $W_{sp} = W_{ch}$ (Figure 4.10 (a)), the charge and spin timescales are the same. In contrast, when $W_{sp} \ll W_{ch}$ (Figure 4.10 (b)), the spin timescales are two orders of magnitude larger than the charge timescales. Therefore, the spin LIOMs contribute to the EE of H_{liom1} at a later time than the charge LIOMs.

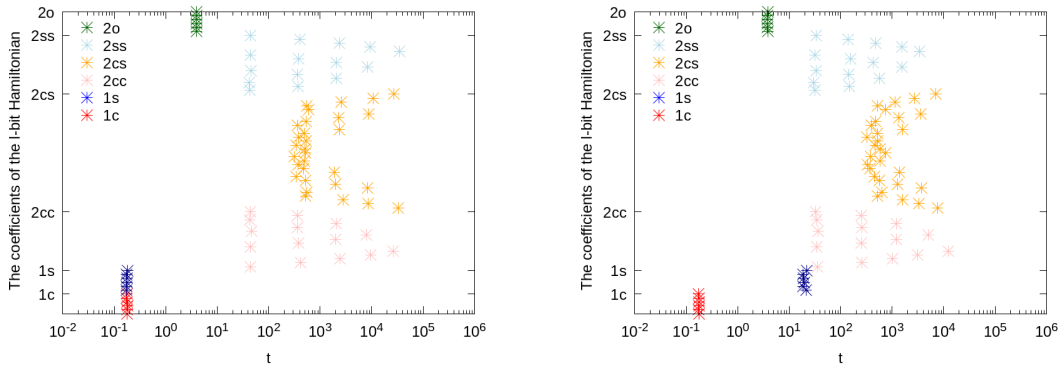

(a) $W_{sp} = W_{ch}$ (b) $W_{sp} \ll W_{ch}$

Figure 4.10: The timescales associated with the first and second-order terms of the l-bit Hamiltonian for $U = 1$, $L = 6$, $n_{HA} = 7$, $W_{ch} = 16$, (a) $W_{sp} = 16$ and (b) $W_{sp} = 0.1$ averaged over 1600 disorder configurations.

The EE obtained from H_{liom1}, reflecting contributions from both first-order charge and first-order spin terms, shows two distinct rises at early and mid times. The wavefunction initially spreads through the localization lengths of charge LIOMs at early times, then continues to spread through those of spin LIOMs at mid times. The extra rise at mid times in the H_{liom1} result arises from the distinct contributions of charge and spin LIOMs to the EE when $W_{sp} \ll W_{ch}$.

Second-order truncated Hamiltonian

Here, we begin by comparing the EE obtained from H_{liom2} with the EE obtained from interacting H_{exact}. Next, we examine the contributions to the EE of the different second-order terms defined in section 2. Finally, we conclude by examining the timescales associated with the coefficients of all the terms in the l-bit Hamiltonian.

Figure 4.11 shows the EE results obtained from H_{liom2}, other second-order truncated l-bit Hamiltonians, and interacting H_{exact}. For clarity, we have presented the results in separate panels. The top two panels show the EE results obtained

from $H_{liom2cc}$ and $H_{liom2ss}$, while the bottom two panels show the EE results obtained from H_{liom2o} and $H_{liom2cs}$. The results for $W_{sp} = W_{ch}$ are shown in the left panels (a) and (c), and the results for $W_{sp} \ll W_{ch}$ are shown in the right panels (b) and (d).

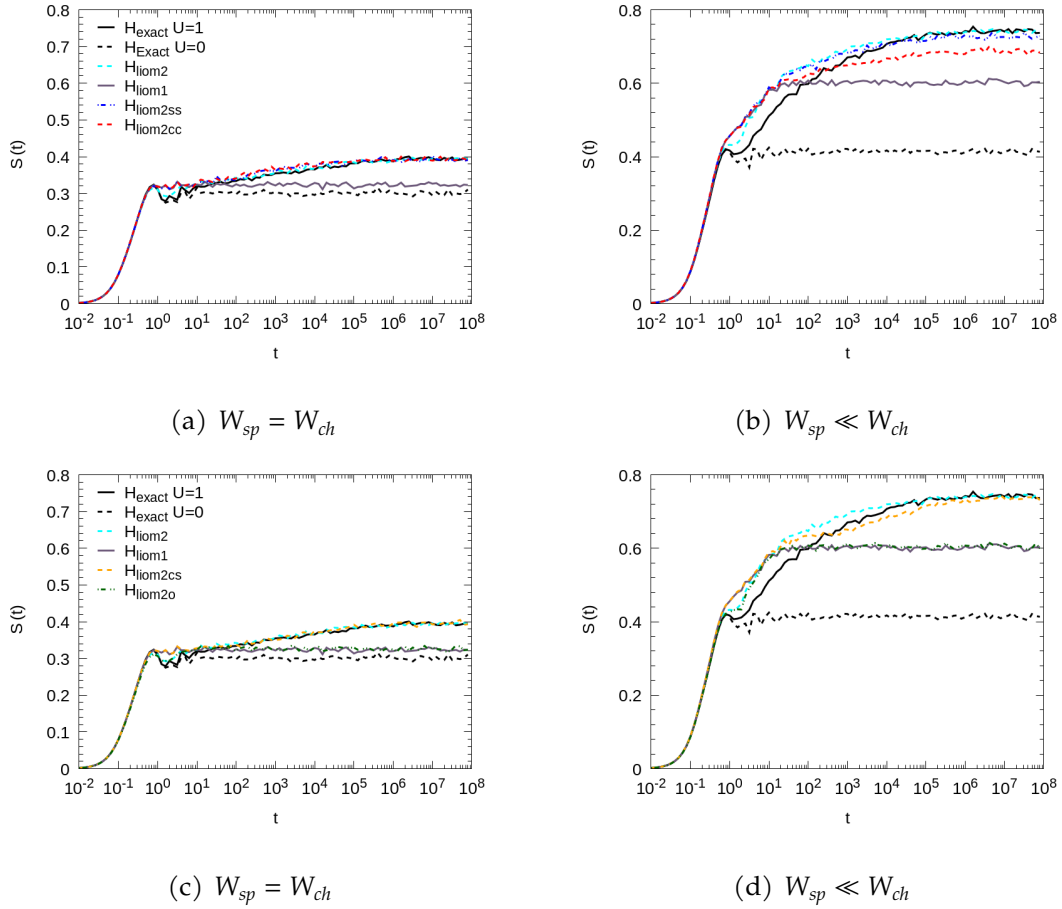

(a) $W_{sp} = W_{ch}$ (b) $W_{sp} \ll W_{ch}$

(c) $W_{sp} = W_{ch}$ (d) $W_{sp} \ll W_{ch}$

Figure 4.11: EE versus time for H_{exact} (black solid), H_{liom1} (dark-purple solid), H_{liom2} (cyan dashed), $H_{liom2cc}$ (red dashed), $H_{liom2cs}$ (orange dashed), $H_{liom2ss}$ (blue dashed), and H_{liom2o} (green dashed) for $L = 6$, $n_{HA} = 7$, $W_{ch} = 16$, and (a,c) $W_{sp} = 16$ and (b,d) $W_{sp} = 0.1$ averaged over 1600 disorder configurations and initial states.

When $W_{sp} = W_{ch}$, the EE from H_{liom2} (cyan dashed) and the EE from interacting H_{exact} (black solid) are the same at all times. When $W_{sp} \ll W_{ch}$, the EE from H_{liom2} and the EE from interacting H_{exact} show similar behavior, although they do not match exactly. At early time, the H_{liom2} result matches the interacting H_{exact} result. At mid times, the H_{liom2} result plateaus and rises while the H_{exact} result shows a dip structure. At long times, although the H_{liom2} result lies above

that of H_{exact}, both exhibit non-logarithmic growth and eventually saturate at the same value.

The mid-time behavior whether the peak-dip structure for $W_{sp} = W_{ch}$ or the plateau for $W_{sp} << W_{ch}$ can be attributed to the second-order terms. This can be understood by comparing the EE obtained from H_{liom2o} the EE obtained from H_{liom1}, and by examining the timescales associated with the coefficients of the second-order on-site terms, J_{2o}. At early and long times, the EE from H_{liom2o} (green dashed) and the H_{liom1} result (dark-purple) are the same for both $W_{sp} = W_{ch}$ and $W_{sp} \ll W_{ch}$. At mid times, when $W_{sp} = W_{ch}$, the H_{liom2o} result shows a dip, while the H_{liom1} result remains at a fixed value. When $W_{sp} \ll W_{ch}$, the H_{liom2o} result shows a plateau, while the H_{liom1} result rises. The green points in Figures 4.10 represent the timescales of the second-order on-site terms, J_{2o}. These timescales are the same for both $W_{sp} = W_{ch}$ and $W_{sp} \ll W_{ch}$, falling at mid times. In both disorder cases, the second-order on-site terms contribute to the EE obtained from H_{liom2} at mid times, resulting in a dip structure when $W_{sp} = W_{ch}$ and a plateau when $W_{sp} \ll W_{ch}$.

The long-time growth in the H_{liom2} result can be understood by comparing the EE obtained from each of $H_{liom2cc}$, $H_{liom2cs}$ and $H_{liom2ss}$ with the EE obtained from H_{liom1}. Additionally, their contribution can be understood by examining the timescales associated with the coupling constants J_{2cc}, J_{2cs}, and J_{2ss}. We observe consistent behavior for both disorder cases, $W_{sp} = W_{ch}$ and $W_{sp} \ll W_{ch}$: At early and mid times, the EE obtained from each of $H_{liom2cc}$ (blue dashed), $H_{liom2ss}$ (red dashed), and $H_{liom2cs}$ (orange dashed), matches the H_{liom1} (dark-purple solid) results. At long times, the EE obtained from each of $H_{liom2cc}$, $H_{liom2ss}$, and $H_{liom2cs}$ shows further growth, while the H_{liom1} result remains at a fixed value. For both disorder cases, the pair-wise couplings between LIOMs contribute to the long-term growth of EE. These long-time contributions of the pair-wise couplings can also be linked to the timescales associated with coupling constants. The

pink, light-blue and orange points in Figures 4.10 represent the timescales associated with the charge-charge J_{2cc}, spin-spin J_{2ss} and charge-spin J_{2cs} couplings. For both $W_{sp} = W_{ch}$ and $W_{sp} \ll W_{ch}$, these timescales are well-separated and distributed across the long-time regime. For both disorder cases, the couplings between charge and spin LIOMs contribute to the long-time growth of the EE obtained from H_{liom2}.

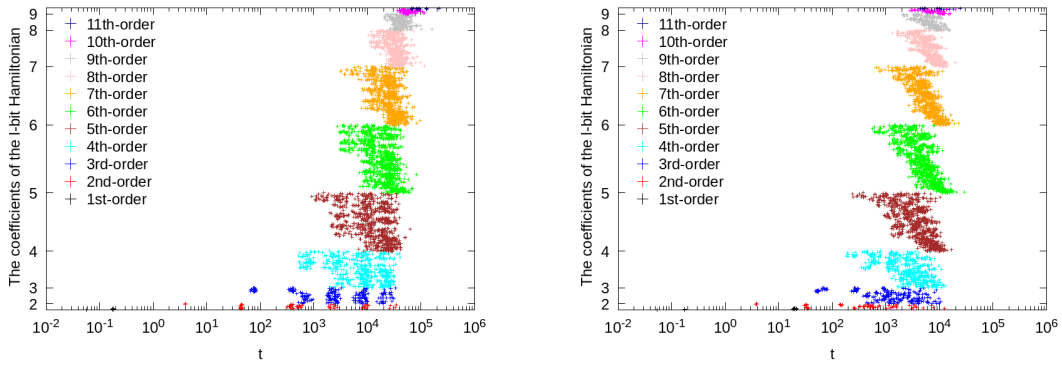

(a) $W_{sp} = W_{ch}$ (b) $W_{sp} \ll W_{ch}$

Figure 4.12: The timescales associated with the coefficients of the l-bit Hamiltonian for $U = 1$, $L = 6$, $n_{HA} = 7$, $W_{ch} = 16$, (a) $W_{sp} = 16$ and (b) $W_{sp} = 0.1$ averaged over 1600 disorder configurations. The timescales associated with the coefficients of each order of terms are shown in different colors, arranged from the lowest at the bottom to the highest at the top.

The high-order terms of the l-bit Hamiltonian are truncated in H_{liom2} but included in H_{exact}. The vertical offset between the H_{liom2} and H_{exact} results when $W_{sp} \ll W_{ch}$ can be understood by examining the timescales associated with the coefficients of the high-order terms. Figure 4.12 (a) and (b) shows the timescales associated with all terms in the l-bit Hamiltonian for $W_{sp} = W_{ch}$ and $W_{sp} \ll W_{ch}$, respectively. The timescales of high-order terms for $W_{sp} \ll W_{ch}$ (Figure 4.12 (b)) are shifted to earlier times compared to those for $W_{sp} = W_{ch}$ (Figure 4.12 (a)). The high-order terms contribute to the EE obtained from the interacting H_{exact} at earlier timescales for $W_{sp} \ll W_{ch}$ than they do for $W_{sp} = W_{ch}$. These timescales are absent in the EE obtained from H_{liom2}. As a result, the EE from H_{liom2} does not closely match the EE from H_{exact} when $W_{sp} \ll W_{ch}$.

Conclusion

We studied the EE time dependence in a disordered Hubbard chain to explore the connection between LIOMs and EE behavior. Specifically, we examined two disorder cases: one with equally strong disorder in both charge and spin channels ($W_{sp} = W_{ch}$), and another with strong disorder in charge channel but weak disorder in spin ($W_{sp} \ll W_{ch}$).

In this thesis, we addressed two primary questions: Starting from a non-entangled state, how do the charge and spin LIOMs contribute to the time dependence of EE? Specifically, does increasing the accuracy level of the Hungarian algorithm reduce the vertical offset observed between EE from H_{liom2} and EE from H_{exact}?

We began by examining how the accuracy level in the Hungarian algorithm affects the EE obtained from H_{liom1} and H_{liom2}. Increasing the accuracy level initially affected the EE values, with convergence observed at $n_{HA} = 1$ for $W_{sp} = W_{ch}$ and at $n_{HA} = 4$ for $W_{sp} \ll W_{ch}$. Further increasing the accuracy to $n_{HA} = 7$ did not change the EE results, so we chose $n_{HA} = 7$ as the accuracy level for constructing both H_{liom1} and H_{liom2} with optimally local integrals of motion.

To understand how interactions influence the EE time dependence, we compared EE results from the exact non-interacting and interacting Hamiltonians. In both disorder cases, EE showed a rapid rise at early times for both Hamiltonians. At long times, in both cases of disorder, the results for the non-interacting Hamiltonian saturated, while the results for the exact interacting Hamiltonian showed further growth. Interactions result in EE growth at long times. When

$W_{sp} = W_{ch}$, the results of the interacting H_{exact} exhibited a $\log(t)$ dependence, spanning five orders of magnitude at long times. The logarithmic growth of EE at long times was similar to that observed in systems with one degree of freedom. However when $W_{sp} \ll W_{ch}$, the interactions between multiple degrees of freedom do not contribute to a simple $\log(t)$ dependence.

To address the broad question, we compared the results of EE obtained from different truncations of H_{liom} with the EE from H_{exact}. For the non-interacting system, the EE obtained from H_{liom1} matched the EE from the non-interacting H_{exact} for both disorder cases. This indicates that, in the absence of interactions, the charge and spin LIOMs accurately capture the EE time dependence of the exact Hamiltonian.

We then compared EE results from the H_{liom1} with interactions with EE from the non-interacting H_{exact}. When $W_{sp} \ll W_{ch}$, the two behave similarly with a rapid initial rise and saturation at long times. The LIOMs with interactions contribute to EE similar to the LIOMs without interactions. When $W_{sp} \ll W_{ch}$, both have a rapid initial rise and saturate at long times, but H_{liom1} result rises significantly above H_{exact} result at mid times. The extra rise is due to the distinct contribution of charge and spin LIOMs to the EE. The charge LIOMs contribute to EE at early times, while the spin LIOMs contribute at mid times. As the many-body wavefunction spreads across the longer localization length of the spin LIOMs, EE rises to a significantly higher value than the non-interacting system.

To address the specific question, we next compared the EE from H_{liom2} with the EE from the interacting H_{exact}. Increasing the accuracy of the Hungarian algorithm reduced the vertical offset between EE of H_{liom2} and EE of H_{exact}. When $W_{sp} = W_{ch}$, the two were the same at all times. When $W_{sp} \ll W_{ch}$, the two were the same at early and saturation times. At mid and long times, the EE of H_{liom2} lay above the EE of H_{exact}, and a vertical offset remains even after optimizing the locality of LIOMs. This result indicated that the remaining vertical offset arises

due to the distinct contribution of charge and spin LIOMs.

We also examined the contribution of the second-order terms to the EE. The results of EE obtained from H_{liom2o} for both disorder cases showed that the second-order on-site operators contribute to the EE of H_{liom2} at mid times resulting in a dip when $W_{sp} = W_{ch}$ and a plateau when $W_{sp} << W_{ch}$. These operators are unique to systems with both spin and charge degrees of freedom per site and are distinct from LIOMs and their pairwise couplings. Further studies on the second-order on-site terms will help clarify why these terms contribute to a decline in EE in a disordered Hubbard chain.

Next, the results of EE obtained from $H_{liom2cc}$, $H_{liom2ss}$, and $H_{liom2cs}$ for both disorder cases showed that the second-order charge-charge, spin-spin, and charge-spin terms contribute to a growth in the EE of H_{liom2} at long times. When $W_{sp} = W_{ch}$, the pair-wise couplings between LIOMs result in a logarithmic growth at long times and contribute to the EE of H_{liom2} in the same way as interactions do to EE of H_{exact}. When $W_{sp} \ll W_{ch}$, the pair-wise couplings between LIOMs do not fully capture the contribution of interactions between the multiple degrees of freedom.

We also calculated the average of coefficients in the l-bit Hamiltonian over disorder configurations and within each type. When $W_{sp} = W_{ch}$, the coefficients of the first-order charge terms were the same as those of the first-order spin terms. When $W_{sp} \ll W_{ch}$, the coefficients of the first-order charge terms were two orders of magnitude larger than those of the first-order spin terms. For both disorder cases, the average coefficients of the second-order on-site terms were the same. For both disordered cases, the charge-spin couplings were one order of magnitude smaller than the charge-charge and spin-spin couplings.

While this study focused on a specific initial condition – a Fock state within the half-filled block with zero net spin – future research could explore systems

with an unequal number of fermions with up and down spin, such as half-filled blocks with non-zero net spin or systems away from half-filling, where the number of fermions does not equal the number of sites. With these initial conditions, the system's charge-spin symmetry is broken [44], potentially leading to different localization effects in various sectors of the Hilbert space. In particular, it would provide insights whether the characteristic logarithmic growth of EE persists when $W_{sp} \ll W_{ch}$ or whether distinctly different timescales emerge for the contributions of LIOMs and the second-order terms to EE.

Another aspect of MBL in systems with one degree of freedom per site is the proportionality of EE saturation value to the system size, which has been extensively studied. Our study relies on the exact diagonalization, which restricts us to small system sizes. Extending this analysis to larger system sizes, such as $L = 8$, would allow for testing the proportionality of EE saturation value with size in systems with two degrees of freedom per site.

Another direction for future research is investigating an interacting case with $U > t$. In this scenario, stronger interactions may suppress particle hopping between sites, allowing us to observe how the time-dependent behavior of EE changes as U increases. In particular, it would be valuable to examine how the insulating phase, when $U >> t$, impacts the EE time dependence.

In summary, by constructing optimally local LIOMs with the accurate implementation of the Hungarian algorithm, we examined how the time-dependent behavior of EE across different time regimes relates to LIOMs and their pair-wise products in a Hubbard chain. The LIOMs, second-order on-site operators, and pairwise couplings between LIOMs contribute to the EE at distinct timescales. With equally strong disorder in both charge and spin channels, we observed a $\log(t)$ dependence of EE at long times, similar to that seen in systems with only one degree of freedom per site. The EE time dependence in our system was also captured by H_{liom2}. In contrast, when disorder is strong in the charge channel

but weak in spin, the EE growth at long times was not simply logarithmic. Spin LIOMs contributed to a further rise in the EE, resulting in the EE of H_{liom2} rising above the EE of H_{exact}.

Bibliography

[1] P. W. Anderson. Absence of diffusion in certain random lattices. *Physical Review*, 109(5):1492–1505, March 1958.

[2] E. Abrahams, P. W. Anderson, D. C. Licciardello, and T. V. Ramakrishnan. Scaling theory of localization: Absence of quantum diffusion in two dimensions. *Physical Review Letters*, 42(10):673–676, March 1979.

[3] L. Fleishman and P. W. Anderson. Interactions and the anderson transition. *Physical Review B*, 21(6):2366–2377, March 1980.

[4] I. V. Gornyi, A. D. Mirlin, and D. G. Polyakov. Interacting electrons in disordered wires: Anderson localization and low-transport. *Physical Review Letters*, 95(20):206603, November 2005.

[5] D.M. Basko, I.L. Aleiner, and B.L. Altshuler. Metal–insulator transition in a weakly interacting many-electron system with localized single-particle states. *Annals of Physics*, 321(5):1126–1205, May 2006.

[6] Dmitry A. Abanin, Ehud Altman, Immanuel Bloch, and Maksym Serbyn. Colloquium : Many-body localization, thermalization, and entanglement. *Reviews of Modern Physics*, 91(2):021001, May 2019.

[7] Rahul Nandkishore and David A. Huse. Many-body localization and thermalization in quantum statistical mechanics. *Annual Review of Condensed Matter Physics*, 6(1):15–38, March 2015.

[8] Luca D'Alessio, Yariv Kafri, Anatoli Polkovnikov, and Marcos Rigol. From quantum chaos and eigenstate thermalization to statistical mechanics and thermodynamics. *Advances in Physics*, 65(3):239–362, May 2016.

[9] Michael Schreiber, Sean S. Hodgman, Pranjal Bordia, Henrik P. Lüschen, Mark H. Fischer, Ronen Vosk, Ehud Altman, Ulrich Schneider, and Immanuel Bloch. Observation of many-body localization of interacting fermions in a quasirandom optical lattice. *Science*, 349(6250):842–845, August 2015.

[10] Gabriele De Chiara, Simone Montangero, Pasquale Calabrese, and Rosario Fazio. Entanglement entropy dynamics of Heisenberg chains. *Journal of Statistical Mechanics: Theory and Experiment*, 2006(03):P03001–P03001, March 2006.

[11] Pasquale Calabrese and John Cardy. Evolution of entanglement entropy in one-dimensional systems. *Journal of Statistical Mechanics: Theory and Experiment*, 2005(04):P04010, April 2005.

[12] Hyungwon Kim and David A. Huse. Ballistic spreading of entanglement in a diffusive nonintegrable system. *Physical Review Letters*, 111(12):127205, September 2013.

[13] Marko Žnidarič, Tomaž Prosen, and Peter Prelovšek. Many-body localization in the Heisenberg XXZ magnet in a random field. *Physical Review B*, 77(6):064426, February 2008.

[14] Ronen Vosk and Ehud Altman. Many-body localization in one dimension as a dynamical renormalization group fixed point. *Physical Review Letters*, 110(6):067204, February 2013.

[15] Jens H. Bardarson, Frank Pollmann, and Joel E. Moore. Unbounded growth of entanglement in models of many-body localization. *Physical Review Letters*, 109(1):017202, July 2012.

[16] Ferenc Iglói, Zsolt Szatmári, and Yu-Cheng Lin. Entanglement entropy dynamics of disordered quantum spin chains. *Physical Review B*, 85(9):094417, March 2012.

[17] Maksym Serbyn, Z. Papić, and Dmitry A. Abanin. Universal slow growth of entanglement in interacting strongly disordered systems. *Physical Review Letters*, 110(26):260601, June 2013.

[18] David A. Huse, Rahul Nandkishore, and Vadim Oganesyan. Phenomenology of fully many-body-localized systems. *Physical Review B*, 90(17):174202, November 2014.

[19] Alexander Lukin, Matthew Rispoli, Robert Schittko, M. Eric Tai, Adam M. Kaufman, Soonwon Choi, Vedika Khemani, Julian Léonard, and Markus Greiner. Probing entanglement in a many-body–localized system. *Science*, 364(6437):256–260, April 2019.

[20] John Preskill. Quantum computing in the nisq era and beyond. *Quantum*, 2:79, August 2018.

[21] Frank Pollmann, Ari M. Turner, Erez Berg, and Masaki Oshikawa. Entanglement spectrum of a topological phase in one dimension. *Physical Review B*, 81(6):064439, February 2010.

[22] M Friesdorf, A H Werner, M Goihl, J Eisert, and W Brown. Local constants of motion imply information propagation. *New Journal of Physics*, 17(11):113054, November 2015.

[23] Elliott H. Lieb and Derek W. Robinson. The finite group velocity of quantum spin systems. *Communications in Mathematical Physics*, 28(3):251–257, September 1972.

[24] David J. Luitz and Yevgeny Bar Lev. Information propagation in isolated quantum systems. *Physical Review B*, 96(2):020406, July 2017.

[25] Christian K. Burrell and Tobias J. Osborne. Bounds on the speed of information propagation in disordered quantum spin chains. *Physical Review Letters*, 99(16):167201, October 2007.

[26] Maksym Serbyn, Z. Papić, and Dmitry A. Abanin. Local conservation laws and the structure of the many-body localized states. *Physical Review Letters*, 111(12):127201, September 2013.

[27] V. Ros, M. Müller, and A. Scardicchio. Integrals of motion in the many-body localized phase. *Nuclear Physics B*, 891:420–465, February 2015.

[28] John Z. Imbrie. On many-body localization for quantum spin chains. *Journal of Statistical Physics*, 163(5):998–1048, April 2016.

[29] John Z. Imbrie. Diagonalization and many-body localization for a disordered quantum spin chain. *Physical Review Letters*, 117(2):027201, July 2016.

[30] Stephen Inglis and Lode Pollet. Accessing many-Body localized states through the generalized Gibbs ensemble. *Physical Review Letters*, 117(12):120402, September 2016.

[31] Louk Rademaker and Miguel Ortuño. Explicit local integrals of motion for the many-body localized state. *Physical Review Letters*, 116(1):010404, January 2016.

[32] Steven J. Thomson and Marco Schirò. Local integrals of motion in quasiperiodic many-body localized systems. *SciPost Physics*, 14(5), May 2023.

[33] Anushya Chandran, Isaac H. Kim, Guifre Vidal, and Dmitry A. Abanin. Constructing local integrals of motion in the many-body localized phase. *Physical Review B*, 91(8):085425, February 2015.

[34] Hansveer Singh, Brayden Ware, Romain Vasseur, and Sarang Gopalakrishnan. Local integrals of motion and the quasiperiodic many-body localization transition. *Physical Review B*, 103(22):L220201, June 2021.

[35] Rong-Qiang He and Zhong-Yi Lu. Interaction-induced characteristic length in strongly many-body localized systems. *Chinese Physics Letters*, 35(2):027101, January 2018.

[36] Pai Peng, Zeyang Li, Haoxiong Yan, Ken Xuan Wei, and Paola Cappellaro. Comparing many-body localization lengths via nonperturbative construction of local integrals of motion. *Physical Review B*, 100(21):214203, December 2019.

[37] Safa Adami, Mohsen Amini, and Morteza Soltani. Structural properties of local integrals of motion across the many-body localization transition via a fast and efficient method for their construction. *Physical Review B*, 106(5):054202, August 2022.

[38] Zahra Gholami, Mohsen Amini, Morteza Soltani, and Ebrahim Ghanbari-Adivi. Multibody expansion of the local integrals of motion: how many pairs of particle-hole do we really need to describe the quasiparticles in the many-body localized phase? *Journal of Physics A: Mathematical and Theoretical*, 56(15):155001, March 2023.

[39] P. Prelovšek, O. S. Barišić, and M. Žnidarič. Absence of full many-body localization in the disordered Hubbard chain. *Physical Review B*, 94(24):241104, December 2016.

[40] Marcin Mierzejewski, Maciej Kozarzewski, and Peter Prelovšek. Counting local integrals of motion in disordered spinless-fermion and Hubbard chains. *Physical Review B*, 97(6):064204, February 2018.

[41] Maciej Kozarzewski, Peter Prelovšek, and Marcin Mierzejewski. Spin subdiffusion in the disordered Hubbard chain. *Physical Review Letters*, 120(24):246602, June 2018.

[42] Jakub Zakrzewski and Dominique Delande. Spin-charge separation and many-body localization. *Physical Review B*, 98(1):014203, July 2018.

[43] R Wortis and Malcolm P Kennett. Local integrals of motion in the two-site anderson-hubbard model. *Journal of Physics: Condensed Matter*, 29(40):405602, September 2017.

[44] Brandon Leipner-Johns and Rachel Wortis. Charge- and spin-specific local integrals of motion in a disordered Hubbard model. *Physical Review B*, 100(12):125132, September 2019.

[45] R.G. Baraniuk and D.L. Jones. Warped wavelet bases: Unitary equivalence and signal processing. In *Digital Speech Processing*, volume 3, pages 111.320–323. Proceedings- ICASSP, IEEE International Conference on Acoustics Speech and Signal Processing, Publ by IEEE, 1993.

[46] Richard Berkovits and Yshai Avishai. Localization in fock space: A finite-energy scaling hypothesis for many-particle excitation statistics. *Physical Review Letters*, 80(3):568–571, January 1998.

[47] James Munkres. Algorithms for the assignment and transportation problems. *Journal of the Society for Industrial and Applied Mathematics*, 5(1):32–38, March 1957.

[48] Stefan Rotter Sonja Grün, editor. *Analysis of Parallel Spike Trains*. Springer US, 2010.

Appendix A: Hungarian algorithm, details

As described in Section 3, the Hungarian algorithm efficiently solves the assignment problem by systematically adjusting a cost matrix to identify the optimal assignment. In this appendix, we describe how the algorithm processes an $N \times N$ cost matrix, detailing the steps it takes to create zeros and handle various scenarios that may arise. We demonstrate these steps using a 3×3 matrix to further clarify the step-by-step process of the Hungarian algorithm:

- Step 1 - Initial Row Reduction:

  The algorithm identifies the smallest value in each row and subtracts it from all other values in that row. This ensures that each row contains at least one zero.

- Step 2a - Initial Assignment of Zeros:

  The algorithm scans the matrix in a row-major order, starting from the top-left element (first row, first column). It identifies the first occurrence of a zero in each row and uncovered column and marks it as starred. The column containing the starred zero is then covered. The algorithm continues this process for the remaining rows, leaving zeros unstarred if they are in a covered column.

- Step 2b - Check for Optimal Assignment:

  If the number of covered columns equals the total number of agents or tasks, denoted as N, the algorithm has found the optimal assignment and

stops. Otherwise, it proceeds to Step 3.

- Step 3 - Cover Rows, Uncover Columns, and Prime Zeros:

  In this step, the algorithm handles situations where zeros exist in uncovered columns. This scenario might arise in two cases: 1. Multiple zeros in one row are created when the algorithm initially creates zeros. 2. As described in step 5, further adjustments of the matrix create a zero in an uncovered column. It primes these zeros and checks if their row contains a starred zero. If a starred zero is found in the same row, the algorithm uncovers the column containing the starred zero and covers the row containing the primed zero. If no starred zero is found, the algorithm proceeds to Step 4. This means that there is another way of starring the zeros, which covers one more column.

  If the condition for Step 4 does not trigger, the maximum number of columns in the adjusted matrix is already covered and the algorithm proceeds to Step 5.

- Step 4 - Path Augmentation:

  If triggered, this step modifies the matrix to increase the number of starred zeros. The algorithm identifies a path through the matrix, defined as a sequence of alternating primed and starred zeros: $Z'_0, Z_1^\star, Z'_2, \ldots, Z'_{2k}$. The *path* begins with a *primed* zero, denoted as Z'_0, which is the first primed zero identified by the algorithm through a row-major search starting from the leftmost element in the first row. If available, $Z_1^\star$ is the *starred* zero in the same column as Z'_0. Following that, Z'_2 represents a *primed* zero located in the same row as $Z_1^\star$, and so on, until it ends with a primed zero that does not have a corresponding starred zero in its column.

  The algorithm then switches the *primed* zeros to *starred* zeros and the *starred* zeros to *primed* zeros along this path, removes all primes, uncovers all

rows, and returns to Step 2a.

- Step 5 - Further Adjustment

  The algorithm adjusts the matrix to create new zeros and increase the number of starred zeros without reducing the existing ones. It identifies the smallest uncovered element, denoted as s, subtracts s from all elements in the uncovered column, and adds s to the elements in covered rows.

  This adjustment results in:

  1. Increasing the values of primed zeros in the intersection of covered columns and rows by s.
  2. Decreasing all uncovered elements by s.
  3. Leaving the rest of the elements unchanged.

  This creates at least one zero in an uncovered column, the algorithm returns to Step 3.

As an example, let's find the optimal assignment for a sample 3×3 matrix. The algorithm begins with Step 1:

$$\begin{bmatrix} 4 & 5 & \textcircled{1} \\ 5 & 6 & \textcircled{1} \\ 7 & \textcircled{2} & 9 \end{bmatrix} \rightarrow \begin{bmatrix} 3 & 4 & 0 \\ 4 & 5 & 0 \\ 5 & 0 & 7 \end{bmatrix}$$

In Steps 2a and 2b, the algorithm covers the second and third columns, but with only two columns covered out of $N = 3$, it moves to Step 3.

$$\begin{bmatrix} 3 & 4 & \textcircled{0} \\ 5 & 6 & 0 \\ 7 & \textcircled{0} & 9 \end{bmatrix} \rightarrow \begin{bmatrix} 3 & 4 & \bigstar \\ 4 & 5 & 0 \\ 5 & \bigstar & 7 \end{bmatrix}$$

In Step 3, no zeros are found in uncovered columns, so the algorithm proceeds to Step 5.

$$\begin{bmatrix} 3 & 4 & \star \\ 4 & 5 & 0 \\ 5 & \star & 7 \end{bmatrix} \rightarrow \begin{bmatrix} 3 & 4 & \star \\ 4 & 5 & 0 \\ 5 & \star & 7 \end{bmatrix}$$

In step 5, the algorithm finds the smallest uncovered value, 3, and subtracts it from all the elements on the uncovered column. It then returns to step 3.

$$\begin{bmatrix} \textcircled{3} & 4 & \star \\ 4 & 5 & 0 \\ 5 & \star & 7 \end{bmatrix} \rightarrow \begin{bmatrix} 0 & 4 & \star \\ 1 & 5 & 0 \\ 2 & \star & 7 \end{bmatrix}$$

Returning to Step 3, the algorithm primes a zero in the first row. Since there is a starred zero in the first row, the condition for Step 4 does not trigger. The algorithm covers the row and uncovers the column that contains the starred zero in the first row, then proceeds to step 5.

$$\begin{bmatrix} \textcircled{0}' & 4 & \star \\ 1 & 5 & 0 \\ 2 & \star & 7 \end{bmatrix} \rightarrow \begin{bmatrix} 0' & 4 & \star \\ 1 & 5 & 0 \\ 2 & \star & 7 \end{bmatrix}$$

In step 5, the algorithm finds the smallest uncovered value, which is again zero. The matrix does not change and it goes back to step 3.

$$\begin{bmatrix} 0' & 4 & \star \\ 1 & 5 & \textcircled{0} \\ 2 & \star & 7 \end{bmatrix} \rightarrow \begin{bmatrix} 0' & 4 & \star \\ 1 & 5 & 0 \\ 2 & \star & 7 \end{bmatrix}$$

In step 3, the algorithm finds another primed zero in the second row. This time, there is no starred zero at the second row and this condition triggers step 4.

$$\begin{bmatrix} 0' & 4 & \star \\ 1 & 5 & \textcircled{0} \\ 2 & \star & 7 \end{bmatrix} \rightarrow \begin{bmatrix} 0' & 4 & \star \\ 1 & 5 & 0' \\ 2 & \star & 7 \end{bmatrix}$$

Notice that the path starts from the primed zero in the second row (green) goes to the starred zero in the first row (red) and ends with another primed zero in the first row and the first column (blue). In step 4, the algorithm switches the primed zeros with the starred ones along the path. It removes all the primes and uncovers all rows, then returns to step 2.

$$\begin{bmatrix} 0' & 4 & \star \\ 1 & 5 & 0' \\ 2 & \star & 7 \end{bmatrix} \rightarrow \begin{bmatrix} \star & 4 & 0' \\ 1 & 5 & \star \\ 2 & \star & 7 \end{bmatrix} \rightarrow \begin{bmatrix} \star & 4 & 0 \\ 1 & 5 & \star \\ 2 & \star & 7 \end{bmatrix}$$

In step 2a, all the columns are covered. In step 2b, the algorithm finishes, because we have found 3 starred zeros out of 3.

$$\begin{bmatrix} \star & 4 & 0 \\ 1 & 5 & \star \\ 2 & \star & 7 \end{bmatrix} \rightarrow \textit{Step2b} \rightarrow \textit{End}$$

The algorithm ultimately produces an assignment array representing the optimal assignment with the minimum total cost. This array contains the row indices of the starred zeros in each column, read from left to right.

In our example, the assignment array is $1, 3, 2$.

The arrangement with minimum cost is found by organizing the columns based

on this assignment array, and the minimum cost is the trace of the resulting matrix.

$$M = \begin{bmatrix} 4 & 5 & 1 \\ 5 & 6 & 1 \\ 7 & 2 & 9 \end{bmatrix} \rightarrow \begin{bmatrix} 4 & 1 & 5 \\ 5 & 1 & 6 \\ 7 & 9 & 2 \end{bmatrix}$$

Appendix B: Partial trace, details

Below, we describe our method for partial tracing of the density matrix, based on the convention that we have used for storing and organizing Fock states of the total system.

As outlined in Section 3, our code uses binary representation of integers as Fock states. We divide our composite system into two halves, left and right. Each Fock state $|n\rangle_{LR}$ is the outer product of the Fock state of the two subsystems:

$$|n\rangle_{LR} = |n_L\rangle \otimes |n_R\rangle \tag{A.1}$$

The table in Equation A.2 shows the Fock basis of total system $\{|n\rangle_{LR}\}$ for $L = 2$ as the outer product of the states of the left $\{|n\rangle_L\}$ and right $\{|n\rangle_R\}$ subsystems according to our conventions:

Total state	Outer product
$\|0\rangle_{LR}$	$\|0\rangle_L \|0\rangle_R$
$\|1\rangle_{LR}$	$\|0\rangle_L \|1\rangle_R$
$\|2\rangle_{LR}$	$\|0\rangle_L \|2\rangle_R$
$\|3\rangle_{LR}$	$\|0\rangle_L \|3\rangle_R$
$\|4\rangle_{LR}$	$\|1\rangle_L \|0\rangle_R$
$\|5\rangle_{LR}$	$\|1\rangle_L \|1\rangle_R$
$\|6\rangle_{LR}$	$\|1\rangle_L \|2\rangle_R$
$\|7\rangle_{LR}$	$\|1\rangle_L \|3\rangle_R$
$\|8\rangle_{LR}$	$\|2\rangle_L \|0\rangle_R$
$\|9\rangle_{LR}$	$\|2\rangle_L \|1\rangle_R$
$\|10\rangle_{LR}$	$\|2\rangle_L \|2\rangle_R$
$\|11\rangle_{LR}$	$\|2\rangle_L \|3\rangle_R$
$\|12\rangle_{LR}$	$\|3\rangle_L \|0\rangle_R$
$\|13\rangle_{LR}$	$\|3\rangle_L \|1\rangle_R$
$\|14\rangle_{LR}$	$\|3\rangle_L \|2\rangle_R$
$\|15\rangle_{LR}$	$\|3\rangle_L \|3\rangle_R$

(A.2)

We take the partial trace over the left subsystem to find the state of the right subsystem.

$$Tr_L[\rho_{LR}] = \sum_n (\langle\alpha|_L \otimes I_R)\rho_{LR}(|\alpha\rangle_L \otimes I_R). \tag{A.3}$$

In Equation A.3, $\{\langle\alpha|\}$ is any basis that spans the Hilbert space of the left Subsytem. In our caculations, it is natural to choose the Fock basis $\{|n\rangle_L\}$.

As we described in Section 3, the density matrix is:

$$\begin{aligned} \left|\psi\right\rangle &= \sum_{m=0}^{N} c_m \left|m\right\rangle \\ &= \sum_{\alpha,\beta=0}^{M} c_{\alpha\beta} \left|\alpha\right\rangle_L \left|\beta\right\rangle_R , \end{aligned} \tag{A.4}$$

where $|n\rangle$ is the Fock basis for the total system, $c_m = \langle m|\psi\rangle$, $|\alpha\rangle_L$ and $|\beta\rangle_R$ is the Fock basis of the left and right subsystem, respectively.

The density matrix ρ_{LR} for the total system is:

$$\begin{aligned} \rho_{LR} &= \left|\psi\right\rangle\left\langle\psi\right| \\ &= (\sum_{\alpha,\beta} c_{\alpha\beta} \left|\alpha\right\rangle_L \left|\beta\right\rangle_R)(\sum_{\alpha',\beta'} c^*_{\alpha'\beta'} \left\langle\alpha'\right|_L \left\langle\beta'\right|_R) \\ &= \sum_{\alpha,\beta,\alpha',\beta'} c_{\alpha\beta} c^*_{\alpha'\beta'} \left|\alpha\right\rangle_L \left|\beta\right\rangle_R \left\langle\alpha'\right|_L \left\langle\beta'\right|_R \\ &= \sum_{m,m'} c_m c^*_{m'} \left|m\right\rangle\left\langle m'\right| \end{aligned} \tag{A.5}$$

The partial trace over the left subsystem is as follows:

$$\begin{aligned} \rho_R = Tr_L[\rho_{LR}] &= \sum_{\gamma=0}^{M} (\left\langle\gamma\right|_L \otimes I_R)\rho_{LR}(\left|\gamma\right\rangle_L \otimes I_R) \\ &= \sum_{\gamma} (\left\langle\gamma\right|_L \otimes I_R)(\sum_{\alpha,\beta,\alpha',\beta'} c_{\alpha\beta} c^*_{\alpha'\beta'} \left|\alpha\right\rangle_L \left|\beta\right\rangle_R \left\langle F_{\alpha'}\right|_L \left\langle F_{\beta'}\right|_R)(\left|\gamma\right\rangle_L \otimes I_R) \\ &= \sum_{\gamma,\alpha,\beta,\alpha',\beta'} c_{\alpha\beta} c^*_{\alpha'\beta'} \left\langle\gamma|\alpha\right\rangle_L (I \left|\beta\right\rangle_R)(\left\langle\beta'\right|_R I) \left\langle\alpha'|\gamma\right\rangle_L \\ &= \sum_{\gamma,\alpha,\beta,\alpha',\beta'} c_{\alpha\beta} c^*_{\alpha'\beta'} \delta_{\gamma,\alpha} \left|\beta\right\rangle_R \left\langle\beta'\right|_R \delta_{\gamma,\alpha'} \\ &= \sum_{\gamma,\beta,\beta'} c_{\gamma\beta} c^*_{\gamma\beta'} \left|\beta\right\rangle_R \left\langle\beta'\right|_R \end{aligned} \tag{A.6}$$

The single coefficient (Fock basis)	The double coefficient (product state)
c_0 to c_{M-1}	$c_{0,0}$ to $c_{0,M-1}$
c_M to c_{2M-1}	$c_{1,0}$ to $c_{1,M-1}$
c_{2M} to c_{3M-1} $\vdots$ c_{N-M} to c_{N-1}	$c_{2,0}$ to $c_{2,M-1}$ $\vdots$ $c_{M-1,0}$ to $c_{M-1,M-1}$

Table A.1: Coefficient in the total Fock basis with single and double subscripts

An element of the reduced density matrix $(\rho_R)_{nm}$.

$$
\begin{aligned}
\Rightarrow (\rho_R)_{nm} &= \langle n|_R \, \rho_R \, |m\rangle_R \\
&= \langle n|_R \, (\sum_{\gamma,\beta,\beta'} c_{\gamma\beta} c^*_{\gamma\beta'} \, |\beta\rangle_R \, \langle\beta'|_R) \, |m\rangle_R \\
&= \sum_{\gamma,\beta,\beta'} c_{\gamma\beta} c^*_{\gamma\beta'} \, \langle n|\beta\rangle_R \, \langle\beta'|m\rangle_R \\
&= \sum_{\gamma,\alpha,\alpha'} c_{\gamma\beta} c^*_{\gamma\beta'} \delta_{n\beta} \delta_{m\beta'} \\
&= \sum_{\gamma} c_{\gamma n} c^*_{\gamma m} \qquad \text{(A.7)}
\end{aligned}
$$

Table A.1 shows the one-to-one mapping between the singular c_i and double $c_{\alpha\beta}$ coefficients.

Using this mapping and Equation A.7, we find each double coefficient in the density matrix and then we calculate the elements of the reduced density matrix.